CHAPTER 5

Kinetostatic Modelling of Micro-motion Stages

A more accurate modelling method compared to the PRBM method is presented in this chapter. This is a kinetostatic model which is capable of predicting both the kinematics and statics of compliant mechanisms. In other words, kinetostatic models allow the fulfillment of both the kinematics and the statics design criteria (Krovi *et al.*, 2002) of compliant micro-motion stages. The kinetostatic models of the two compliant stages, which were the four-bar compliant mechanism and the 3-RRR compliant stage were derived. The kinetostatic models were derived to have closed-form equations. Material and link parameters are variables in the models. Flexure hinge compliances are also one of the variables in these models. Therefore, the most suitable flexure hinge compliance equation can be selected based on the scheme developed in Chapter 3 to calculate the kinetostatics of compliant micro-motion stages accurately. Two cases of the four-bar mechanism and the 3-RRR micro-motion stage respectively were studied to a) investigate the effect of inaccurate modelling of flexure hinge compliances on the accuracy of the kinetostatic models, and b) to demonstrate the advantages of the derived closed-form kinetostatic models with flexure hinge compliances as one of the variables. Analytical matrices of the kinetostatic models of Case 1 were calculated by deliberately choosing the flexure hinge equations which have large differences when compared to FEA results (refer to Figures 3.12-3.14). Meanwhile, analytical matrices of Case 2 were obtained by choosing the flexure hinge equations with small differences (refer to Figures 3.12-3.14 and Table 3.9).

Nomenclature

Note: Matrices are shown in boldface.

Subscripts	
$1, 2, 3, o', o$	Point 1, 2, 3, o', o
x, y, z	reference axes
$h1, h2, h3$	Hinge 1, 2, 3
L_1, L_2, L_3	Link 1, 2, 3
Superscript	
$1, 2, 3$	reference axes of flexure hinges
Symbols	
x, y	reference axes
Δx, Δy	translational displacements along the x- and y-axis, also named as Δx-displacement and Δy-displacement
$\Delta\alpha$	rotational displacement motion about the z-axis, also named as $\Delta\alpha$-displacement
$\mathbf{C}$	compliance matrix
F, M	force, moment
$\partial\Delta x/\partial F$, $\partial\Delta x/\partial M$	the change of Δx-displacement due to forces/moment
$\partial\Delta y/\partial F$, $\partial\Delta y/\partial M$	the change of Δy-displacement due to forces/moment
$\partial\Delta\alpha/\partial F$, $\partial\Delta\alpha/\partial M$	the change of $\Delta\alpha$-displacement due to forces/moment
$[\Delta\alpha_z/M_z]_j$,$[\Delta y/F_y]_j$, $[\Delta x/F_x]_j$,	compliances of flexure hinge j, where j =1, 2, 3
t_j	smallest thickness of flexure hinge j, where j = 1, 2, 3
R_j	radius of flexure hinge j, where j = 1, 2, 3
$\mathbf{D}$	displacement matrix

5.1 Kinetostatic model of four-bar compliant mechanisms

The kinetostatic model of a four-bar compliant mechanism is shown below.

$$\begin{bmatrix} \mathbf{U_o} \\ U_{in} \end{bmatrix} = \begin{bmatrix} \mathbf{C_{o,F_o}} & \mathbf{C_{o,F_{in}}} \\ \mathbf{C_{in,F_o}} & C_{in,F_{in}} \end{bmatrix} \begin{bmatrix} \mathbf{F_o} \\ F_{in} \end{bmatrix} \tag{5.1}$$

where $\mathbf{U_o} = \begin{bmatrix} \Delta x_o & \Delta y_o & \Delta \alpha_o \end{bmatrix}^T$ is a 3x1 matrix representing the output displacements of the compliant mechanism,
U_{in} is a constant representing the input displacements of the compliant mechanism,
$\mathbf{F_o} = \begin{bmatrix} F_{ox} & F_{oy} & M_{oz} \end{bmatrix}^T$ is a 3x1 matrix representing the output forces/moment acting at Point o,
F_{in} is a constant representing the input forces,
$\mathbf{C_{o,F_o}}$ is a 3x3 compliance matrix relating the output displacements to the output forces/moment,
$\mathbf{C_{o,F_{in}}}$ is a 3x1 compliance matrix relating the output displacements to the input forces,
$\mathbf{C_{in,F_o}}$ is a 1x3 compliance matrix relating the input displacements to the output forces/moment,
$C_{in,F_{in}}$ is a constant relating the input displacements to the input forces.

5.1.1 Derivation of the output compliance matrix, $\mathbf{C_{o,F_o}}$

The four-bar compliant structure is divided into two links in order to calculate the $\mathbf{C_{o,F_o}}$ matrix. Each link consists of two flexure hinges. The flexure hinge compliances are $[\Delta\alpha_z/M_z]_j$, $[\Delta y/F_y]_j$ and $[\Delta x/F_x]_j$ where j =1,2. Link 1 of the four-bar compliant structure is shown in Figure 5.1b together with its dimensions, displacements, local coordinates of flexure hinges and the applied forces/moment. The compliances at Point o' contributed by each flexure hinge in the structure are firstly calculated. These compliance matrices are named $\mathbf{C_{h1}}$ and $\mathbf{C_{h2}}$. The two flexure hinges of Link 1 are arranged in series; therefore the compliance matrix of the four-bar structure at Point o' can be obtained by summing $\mathbf{C_{h1}}$ and $\mathbf{C_{h2}}$. The compliance matrices of the two links are referred to as $\mathbf{C_{L_1o,F_o}}$ and $\mathbf{C_{L_2o,F_o}}$ respectively. The two links of the four-bar structure are arranged in parallel; therefore the $\mathbf{C_{o,F_o}}$ matrix in Equation 5.1 is calculated by summing $\mathbf{C_{L_1o,F_o}}$ and $\mathbf{C_{L_2o,F_o}}$ using the rule

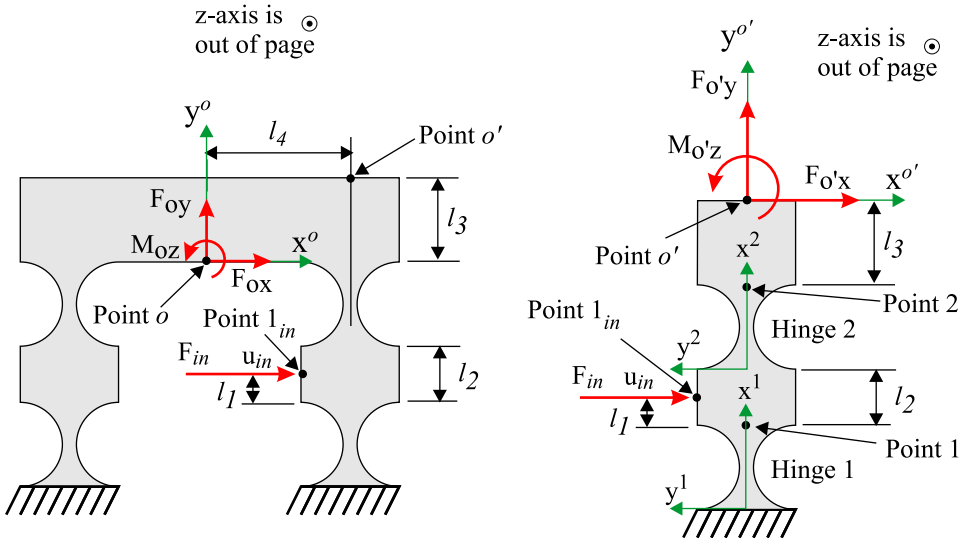

(a) Four-bar compliant mechanism (b) Link 1 of the four-bar mechanism

Figure 5.1: Four-bar compliant mechanism

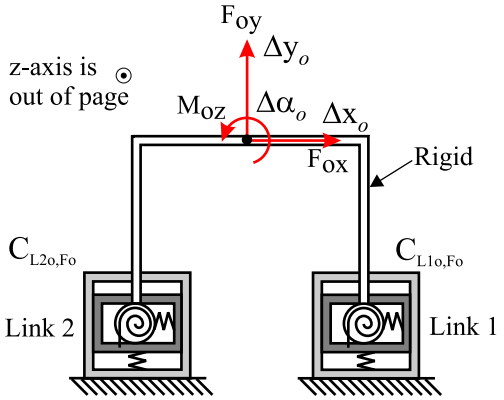

Figure 5.2: Parallel spring model of the four-bar compliant mechanism

of parallel connection of springs (see Figure 5.2). Throughout the derivation of the kinetostatic model in this thesis, it is assumed that a) the structural deformations only occur at flexure hinges and no deformations occur at rigid linkages, and b) the translational and rotational displacements are small enough to be linearised.

5.1.1.1 Compliances of the four-bar mechanism due to Hinge 1

The compliance matrix of the four-bar compliant structure due to Hinge 1 is expressed as,

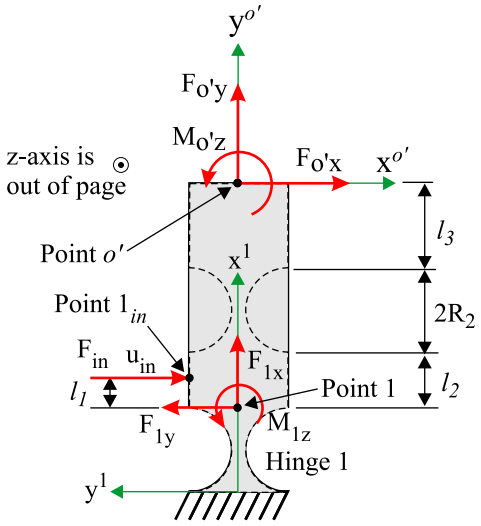

Figure 5.3: Compliances due to Hinge 1

$$\mathbf{C_{h1}} = \begin{bmatrix} \partial\Delta x^1_{o'}/\partial F_{o'x} & \partial\Delta x^1_{o'}/\partial F_{o'y} & \partial\Delta x^1_{o'}/\partial M_{o'z} \\ \partial\Delta y^1_{o'}/\partial F_{o'x} & \partial\Delta y^1_{o'}/\partial F_{o'y} & \partial\Delta y^1_{o'}/\partial M_{o'z} \\ \partial\Delta \alpha^1_{o'}/\partial F_{o'x} & \partial\Delta \alpha^1_{o'}/\partial F_{o'y} & \partial\Delta \alpha^1_{o'}/\partial M_{o'z} \end{bmatrix} \tag{5.2}$$

where the partial derivative terms in Equation 5.2 are derived as follows:

From Figure 5.3, forces/moment acting at Point o' and Point 1_{in}* can be resolved into forces/moment acting at Point 1 as follows,

$$\begin{aligned} F_{1x} &= F_{o'y} \\ F_{1y} &= -F_{o'x} - F_{in} \\ M_{1z} &= -F_{o'x}\,(l_2 + l_3 + 2R_2) - F_{in} l_1 + M_{o'z} \end{aligned} \tag{5.3}$$

Derivation of $\partial\Delta\alpha^1_{o'}/\partial F_{o'x}$, $\partial\Delta\alpha^1_{o'}/\partial F_{o'y}$ *and* $\partial\Delta\alpha^1_{o'}/\partial M_{o'z}$

The rotational displacements about the z-axis, $\Delta\alpha^1_1$-displacement at Point 1 can be calculated as shown below,

*Input forces acting at this point are going to be used to calculate compliance matrices $\mathbf{C_{o,F_{in}}}$, $\mathbf{C_{F_{in},o}}$ and $\mathbf{C_{in,F_{in}}}$ later in this section.

$$\begin{aligned}\Delta\alpha_1^1 &= \left[\frac{\Delta\alpha_z}{M_z}\right]_1 M_{1z} + \left[\frac{\Delta\alpha_z}{M_z}\right]_1 F_{1y}R_1 \\ &= \left[\frac{\Delta\alpha_z}{M_z}\right]_1 \{-F_{o'x}(l_2+l_3+2R_2) - F_{in}l_1 + M_{o'z}\} + \left[\frac{\Delta\alpha_z}{M_z}\right]_1 (-F_{o'x} - F_{in})R_1 \\ &= \left[\frac{\Delta\alpha_z}{M_z}\right]_1 \{-F_{o'x}(l_2+l_3+2R_2+R_1) - F_{in}(l_1+R_1) + M_{o'z}\} \end{aligned} \tag{5.4}$$

The $\Delta\alpha_1^1$-compliances of Hinge 1 caused by $F_{o'x}$, $F_{o'y}$ and $M_{o'z}$ are obtained by taking the partial derivatives of $\Delta\alpha_1^1$ with respect to the forces/moment acting at Point o',

$$\frac{\partial\Delta\alpha_1^1}{\partial F_{o'x}} = -(l_2+l_3+2R_2+R_1)\left[\frac{\Delta\alpha_z}{M_z}\right]_1 \tag{5.5}$$

$$\frac{\partial\Delta\alpha_1^1}{\partial F_{o'y}} = 0 \tag{5.6}$$

$$\frac{\partial\Delta\alpha_1^1}{\partial M_{o'z}} = \left[\frac{\Delta\alpha_z}{M_z}\right]_1 \tag{5.7}$$

The results of the partial derivatives of $\Delta\alpha_1^1$ in Equations 5.5 to 5.7 describe the relationship between the $\Delta\alpha_1^1$-displacement and the forces/moment. The partial derivatives of the Δx- and Δy-displacements with respect to forces/moment also describe this similar relationship.

The rotational displacements about the z-axis, $\Delta\alpha_{o'}^1$-displacement at Point o' is the same as $\Delta\alpha_1^1$-displacement. Therefore, their results of the partial derivatives are the same as Equations 5.5, 5.6 and 5.7.

$$\frac{\partial\Delta\alpha_{o'}^1}{\partial F_{o'x}} = -(l_2+l_3+2R_2+R_1)\left[\frac{\Delta\alpha_z}{M_z}\right]_1 \tag{5.8}$$

$$\frac{\partial\Delta\alpha_{o'}^1}{\partial F_{o'y}} = 0 \tag{5.9}$$

$$\frac{\partial \Delta\alpha^1_{o'}}{\partial M_{o'z}} = \left[\frac{\Delta\alpha_z}{M_z}\right]_1 \tag{5.10}$$

Derivation of $\partial\Delta y^1_{o'}/\partial F_{o'x}$, $\partial\Delta y^1_{o'}/\partial F_{o'y}$ ***and*** $\partial\Delta y^1_{o'}/\partial M_{o'z}$

The translational displacement along the y-axis, Δy^1_1-displacement at Point 1 can be calculated as shown below,

$$\begin{aligned}\Delta y^1_1 &= \left[\frac{\Delta y}{F_y}\right]_1 F_{1y} + \left[\frac{\Delta\alpha_z}{M_z}\right]_1 M_{1z}R_1 \\ &= -\left[\frac{\Delta y}{F_y}\right]_1 (F_{o'x} + F_{in}) \\ &\quad + \left[\frac{\Delta\alpha_z}{M_z}\right]_1 \{-F_{o'x}(l_2 + l_3 + 2R_2) - F_{in}l_1 + M_{o'z}\} R_1\end{aligned} \tag{5.11}$$

The Δy^1_1-compliances of Hinge 1 caused by $F_{o'x}$, $F_{o'y}$ and $M_{o'z}$ are obtained by taking the partial derivatives of Δy^1_1 with respect to the forces/moment acting at Point o',

$$\frac{\partial \Delta y^1_1}{\partial F_{o'x}} = -\left[\frac{\Delta y}{F_y}\right]_1 - (l_2 + l_3 + 2R_2) R_1 \left[\frac{\Delta\alpha_z}{M_z}\right]_1 \tag{5.12}$$

$$\frac{\partial \Delta y^1_1}{\partial F_{o'y}} = 0 \tag{5.13}$$

$$\frac{\partial \Delta y^1_1}{\partial M_{o'z}} = R_1 \left[\frac{\Delta\alpha_z}{M_z}\right]_1 \tag{5.14}$$

Due to the amplification of the link with distance $l_2 + l_3 + 2R_2$, the translational displacements, $\Delta y^1_{o'}$-displacement at Point o' is the summation of Δy^1_1-displacement at Point 1 and the amplified displacements caused by the rotational motions of the link (see Figure 5.4). Therefore, the $\Delta y^1_{o'}$-displacement is,

$$\Delta y^1_{o'} = \Delta y^1_1 + \Delta\alpha^1_{o'}(l_2 + l_3 + 2R_2) \tag{5.15}$$

The $\Delta y^1_{o'}$-compliances of Hinge 1 caused by $F_{o'x}$, $F_{o'y}$ and $M_{o'z}$ are obtained by

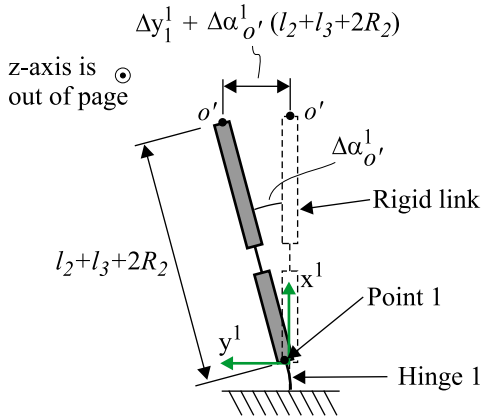

Figure 5.4: $\Delta y_{o'}^1$-displacement caused by the amplification of link with distance $l_2 + l_3 + 2R_2$. Dashed lines represent initial position of the four-bar compliant structure. The flexure hinge is drawn as a solid line and the rigid link is drawn as a block

taking the partial derivatives of $\Delta y_{o'}^1$ with respect to all the forces/moment acting at Point o',

$$\begin{aligned}
\frac{\partial \Delta y_{o'}^1}{\partial F_{o'x}} &= \frac{\partial \Delta y_1^1}{\partial F_{o'x}} + \frac{\partial \Delta \alpha_{o'}^1}{\partial F_{o'x}} (l_2 + l_3 + 2R_2) \\
&= -\left[\frac{\Delta y}{F_y}\right]_1 - (l_2 + l_3 + 2R_2) R_1 \left[\frac{\Delta \alpha_z}{M_z}\right]_1 \\
&\quad + \left\{-(l_2 + l_3 + 2R_2)(l_2 + l_3 + 2R_2 + R_1)\left[\frac{\Delta \alpha_z}{M_z}\right]_1\right\} \\
&= -\left[\frac{\Delta y}{F_y}\right]_1 - \{(l_2 + l_3 + 2R_2) R_1 \\
&\quad + (l_2 + l_3 + 2R_2)(l_2 + l_3 + 2R_2 + R_1)\} \left[\frac{\Delta \alpha_z}{M_z}\right]_1
\end{aligned} \tag{5.16}$$

$$\begin{aligned}
\frac{\partial \Delta y_{o'}^1}{\partial F_{o'y}} &= \frac{\partial \Delta y_1^1}{\partial F_{o'y}} + \frac{\partial \Delta \alpha_{o'}^1}{\partial F_{o'y}} (l_2 + l_3 + 2R_2) \\
&= 0
\end{aligned} \tag{5.17}$$

$$\begin{aligned}\frac{\partial \Delta y^1_{o'}}{\partial M_{o'z}} &= \frac{\partial \Delta y^1_1}{\partial M_{o'z}} + \frac{\partial \Delta \alpha^1_{o'}}{\partial M_{o'z}} (l_2 + l_3 + 2R_2) \\ &= R_1 \left[\frac{\Delta \alpha_z}{M_z}\right]_1 + (l_2 + l_3 + 2R_2) \left[\frac{\Delta \alpha_z}{M_z}\right]_1 \\ &= (l_2 + l_3 + R_1 + 2R_2) \left[\frac{\Delta \alpha_z}{M_z}\right]_1 \end{aligned} \tag{5.18}$$

Derivation of $\partial \Delta x^1_{o'}/\partial F_{o'x}$**,** $\partial \Delta x^1_{o'}/\partial F_{o'y}$ ***and*** $\partial \Delta x^1_{o'}/\partial M_{o'z}$

The translational displacements along the x-axis, Δx^1_1-displacement at Point 1 can be calculated as shown below,

$$\begin{aligned}\Delta x^1_1 &= \left[\frac{\Delta x}{F_x}\right]_1 F_{1x} \\ &= \left[\frac{\Delta x}{F_x}\right]_1 F_{o'y} \end{aligned} \tag{5.19}$$

The Δx^1_1-compliances of Hinge 1 caused by $F_{o'x}$, $F_{o'y}$ and $M_{o'z}$ are obtained by taking the partial derivatives of Δx^1_1 with respect to the forces/moment acting at Point o',

$$\frac{\partial \Delta x^1_1}{\partial F_{o'x}} = 0 \tag{5.20}$$

$$\frac{\partial \Delta x^1_1}{\partial F_{o'y}} = \left[\frac{\Delta x}{F_x}\right]_1 \tag{5.21}$$

$$\frac{\partial \Delta x^1_1}{\partial M_{o'z}} = 0 \tag{5.22}$$

Due to the amplification of the link with distance $l_2 + l_3 + 2R_2$, the translational displacements, $\Delta x^1_{o'}$-displacement at Point o' is the summation of Δx^1_1-displacement at Point 1 and the amplified displacements caused by the rotational motions of the link (see Figure 5.5). Therefore, the $\Delta x^1_{o'}$-displacement is,

$$\Delta x^1_{o'} = \Delta x^1_1 + \left\{(l_2 + l_3 + 2R_2) - (l_2 + l_3 + 2R_2)\, cos\left(\Delta \alpha^1_{o'}\right)\right\} \tag{5.23}$$

However, the term $\{(l_2 + l_3 + 2R_2) - (l_2 + l_3 + 2R_2)\, cos\,(\Delta \alpha^1_{o'})\}$ in Equation 5.23 is very small. Thus, Equation 5.23 is reduced to,

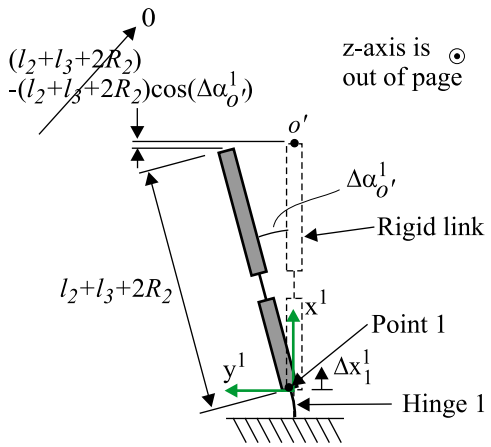

Figure 5.5: $\Delta x^1_{o'}$-displacement caused by the amplification of link with distance $l_2 + l_3 + 2R_2$. Dashed lines represent initial position of the four-bar compliant structure. The flexure hinge is drawn as a solid line and the rigid link is drawn as a block

$$\Delta x^1_{o'} = \Delta x^1_1 \tag{5.24}$$

Therefore, the $\Delta x^1_{o'}$-compliances are the same as the Δx^1_1-compliances.

$$\frac{\partial \Delta x^1_{o'}}{\partial F_{o'x}} = 0 \tag{5.25}$$

$$\frac{\partial \Delta x^1_{o'}}{\partial F_{o'y}} = \left[\frac{\Delta x}{F_x}\right]_1 \tag{5.26}$$

$$\frac{\partial \Delta x^1_{o'}}{\partial M_{o'z}} = 0 \tag{5.27}$$

By substituting Equations 5.8-5.10, 5.16-5.18 and 5.25-5.27 into Equation 5.2, the compliance matrix of the four-bar compliant structure due to Hinge 1 can be obtained.

5.1.1.2 Compliances of the four-bar mechanism due to Hinge 2

The compliance matrix of the four-bar compliant structure due to Hinge 2 is expressed as,

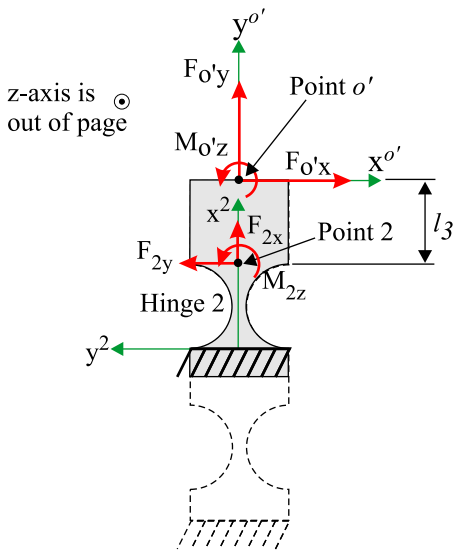

Figure 5.6: Compliances due to Hinge 2

$$\mathbf{C_{h2}} = \begin{bmatrix} \partial\Delta x^2_{o'}/\partial F_{o'x} & \partial\Delta x^2_{o'}/\partial F_{o'y} & \partial\Delta x^2_{o'}/\partial M_{o'z} \\ \partial\Delta y^2_{o'}/\partial F_{o'x} & \partial\Delta y^2_{o'}/\partial F_{o'y} & \partial\Delta y^2_{o'}/\partial M_{o'z} \\ \partial\Delta \alpha^2_{o'}/\partial F_{o'x} & \partial\Delta \alpha^2_{o'}/\partial F_{o'y} & \partial\Delta \alpha^2_{o'}/\partial M_{o'z} \end{bmatrix} \tag{5.28}$$

where the partial derivative terms in Equation 5.28 are derived as follows:

From Figure 5.6, forces/moment acting at Point o' can be resolved into forces/moment acting at Point 2 as follows,

$$\begin{aligned} F_{2x} &= F_{o'y} \\ F_{2y} &= -F_{o'x} \\ M_{2z} &= -F_{o'x} l_3 + M_{o'z} \end{aligned} \tag{5.29}$$

Derivation of $\partial\Delta\alpha^2_{o'}/\partial F_{o'x}$, $\partial\Delta\alpha^2_{o'}/\partial F_{o'y}$ ***and*** $\partial\Delta\alpha^2_{o'}/\partial M_{o'z}$

The rotational displacements about the z-axis, $\Delta\alpha^2_2$-displacement at Point 2 can be calculated as shown below,

$$\begin{aligned}\Delta\alpha_2^2 &= \left[\frac{\Delta\alpha_z}{M_z}\right]_2 M_{2z} + \left[\frac{\Delta\alpha_z}{M_z}\right]_2 F_{2y}R_2 \\ &= \left[\frac{\Delta\alpha_z}{M_z}\right]_2 (-F_{o'x}l_3 + M_{o'z}) + \left[\frac{\Delta\alpha_z}{M_z}\right]_2 (-F_{o'x}R_2) \\ &= \left[\frac{\Delta\alpha_z}{M_z}\right]_2 (-F_{o'x}(l_3 + R_2) + M_{o'z}) \end{aligned} \tag{5.30}$$

The $\Delta\alpha_2^2$-compliances of Hinge 2 caused by $F_{o'x}$, $F_{o'y}$ and $M_{o'z}$ are obtained by taking the partial derivatives of $\Delta\alpha_2^2$ with respect to the forces/moment acting at Point o',

$$\frac{\partial\Delta\alpha_2^2}{\partial F_{o'x}} = -(l_3 + R_2)\left[\frac{\Delta\alpha_z}{M_z}\right]_2 \tag{5.31}$$

$$\frac{\partial\Delta\alpha_2^2}{\partial F_{o'y}} = 0 \tag{5.32}$$

$$\frac{\partial\Delta\alpha_2^2}{\partial M_{o'z}} = \left[\frac{\Delta\alpha_z}{M_z}\right]_2 \tag{5.33}$$

The rotational displacements, $\Delta\alpha_{o'}^2$-displacement at Point o' is the same as $\Delta\alpha_2^2$-displacement. Therefore, their results of the partial derivatives are the same as Equations 5.31, 5.32 and 5.33.

$$\frac{\partial\Delta\alpha_{o'}^2}{\partial F_{o'x}} = -(l_3 + R_2)\left[\frac{\Delta\alpha_z}{M_z}\right]_2 \tag{5.34}$$

$$\frac{\partial\Delta\alpha_{o'}^2}{\partial F_{o'y}} = 0 \tag{5.35}$$

$$\frac{\partial\Delta\alpha_{o'}^2}{\partial M_{o'z}} = \left[\frac{\Delta\alpha_z}{M_z}\right]_2 \tag{5.36}$$

Derivation of $\partial\Delta y^2_{o'}/\partial F_{o'x}$, $\partial\Delta y^2_{o'}/\partial F_{o'y}$ ***and*** $\partial\Delta y^2_{o'}/\partial M_{o'z}$

The translational displacements along the y-axis, Δy_2^2-displacement at Point 2 can be calculated as shown below,

$$\begin{aligned}\Delta y_2^2 &= \left[\frac{\Delta y}{F_y}\right]_2 F_{2y} + \left[\frac{\Delta \alpha_z}{M_z}\right]_2 M_{2z} R_2 \\ &= -\left[\frac{\Delta y}{F_y}\right]_2 F_{o'x} + \left[\frac{\Delta \alpha_z}{M_z}\right]_2 (M_{o'z} - F_{o'x} l_3)\, R_2 \end{aligned} \tag{5.37}$$

The Δy_2^2-compliances of Hinge 2 caused by $F_{o'x}$, $F_{o'y}$ and $M_{o'z}$ are obtained by taking the partial derivatives of Δy_2^2 with respect to the forces/moment acting at Point o',

$$\frac{\partial \Delta y_2^2}{\partial F_{o'x}} = -\left[\frac{\Delta y}{F_y}\right]_2 - l_3 R_2 \left[\frac{\Delta \alpha_z}{M_z}\right]_2 \tag{5.38}$$

$$\frac{\partial \Delta y_2^2}{\partial F_{o'y}} = 0 \tag{5.39}$$

$$\frac{\partial \Delta y_2^2}{\partial M_{o'z}} = R_2 \left[\frac{\Delta \alpha_z}{M_z}\right]_2 \tag{5.40}$$

Due to the amplification of the link with distance l_3, the translational displacements, $\Delta y_{o'}^2$-displacement at Point o' is the summation of Δy_2^2-displacement at Point 2 and the amplified displacements caused by the rotational motions of the link (see Figure 5.7). Therefore, the $\Delta y_{o'}^2$-displacement is,

$$\Delta y_{o'}^2 = \Delta y_2^2 + \Delta \alpha_{o'}^2 l_3 \tag{5.41}$$

The $\Delta y_{o'}^2$-compliances of Hinge 2 caused by $F_{o'x}$, $F_{o'y}$ and $M_{o'z}$ are obtained by taking the partial derivatives of $\Delta y_{o'}^2$ with respect to all the forces/moment acting at Point o',

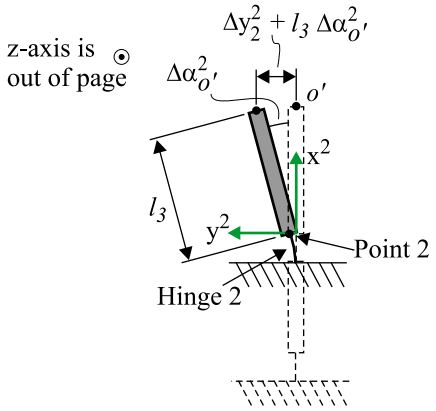

Figure 5.7: $\Delta y_{o'}^2$-displacement caused by the amplification of link with distance l_3. Dashed lines represent initial position of the four-bar compliant structure. The flexure hinge is drawn as a solid line and the rigid link is drawn as a block

$$\begin{aligned}\frac{\partial \Delta y_{o'}^2}{\partial F_{o'x}} &= \frac{\partial \Delta y_2^2}{\partial F_{o'x}} + \frac{\partial \Delta \alpha_{o'}^2}{\partial F_{o'x}} l_3 \\ &= -\left[\frac{\Delta y}{F_y}\right]_2 - l_3 R_2 \left[\frac{\Delta \alpha_z}{M_z}\right]_2 + \left\{-l_3\left(l_3 + R_2\right)\left[\frac{\Delta \alpha_z}{M_z}\right]_2\right\} \\ &= -\left[\frac{\Delta y}{F_y}\right]_2 - l_3\left(l_3 + 2R_2\right)\left[\frac{\Delta \alpha_z}{M_z}\right]_2 \end{aligned} \tag{5.42}$$

$$\begin{aligned}\frac{\partial \Delta y_{o'}^2}{\partial F_{o'y}} &= \frac{\partial \Delta y_2^2}{\partial F_{o'y}} + \frac{\partial \Delta \alpha_{o'}^2}{\partial F_{o'y}} l_3 \\ &= 0 \end{aligned} \tag{5.43}$$

$$\begin{aligned}\frac{\partial \Delta y_{o'}^2}{\partial M_{o'z}} &= \frac{\partial \Delta y_2^2}{\partial M_{o'z}} + \frac{\partial \Delta \alpha_{o'}^2}{\partial M_{o'z}} l_3 \\ &= R_2 \left[\frac{\Delta \alpha_z}{M_z}\right]_2 + l_3 \left[\frac{\Delta \alpha_z}{M_z}\right]_2 \\ &= \left(l_3 + R_2\right)\left[\frac{\Delta \alpha_z}{M_z}\right]_2 \end{aligned} \tag{5.44}$$

Derivation of $\partial \Delta x_{o'}^2 / \partial F_{o'x}$, $\partial \Delta x_{o'}^2 / \partial F_{o'y}$ ***and*** $\partial \Delta x_{o'}^2 / \partial M_{o'z}$

The translational displacement along the x-axis, Δx_2^2-displacement at Point 2 can be calculated as shown below,

$$\begin{aligned} \Delta x_2^2 &= \left[\frac{\Delta x}{F_x}\right]_2 F_{2x} \\ &= \left[\frac{\Delta x}{F_x}\right]_2 F_{o'y} \end{aligned} \tag{5.45}$$

The Δx_2^2-compliances of Hinge 2 caused by $F_{o'x}$, $F_{o'y}$ and $M_{o'z}$ are obtained by taking the partial derivatives of Δx_2^2 with respect to the forces/moment acting at Point o',

$$\frac{\partial \Delta x_2^2}{\partial F_{o'x}} = 0 \tag{5.46}$$

$$\frac{\partial \Delta x_2^2}{\partial F_{o'y}} = \left[\frac{\Delta x}{F_x}\right]_2 \tag{5.47}$$

$$\frac{\partial \Delta x_2^2}{\partial M_{o'z}} = 0 \tag{5.48}$$

Due to the amplification of the link with distance l_3, the translational displacements, $\Delta x_{o'}^2$-displacement at Point o' is the summation of Δx_2^2-displacement at Point 2 and the amplified displacements caused by the rotational motions of the link (see Figure 5.8). Therefore, the $\Delta x_{o'}^2$-displacement is,

$$\Delta x_{o'}^2 = \Delta x_2^2 + \left\{l_3 - l_3 cos\left(\Delta \alpha_{o'}^2\right)\right\} \tag{5.49}$$

However, the term $\{l_3 - l_3 cos\,(\Delta \alpha_{o'}^2)\}$ in Equation 5.49 is very small. Thus, Equation 5.49 is reduced to,

$$\Delta x_{o'}^2 = \Delta x_2^2 \tag{5.50}$$

Therefore, the $\Delta x_{o'}^2$-compliances are the same as the Δx_2^2-compliances,

$$\frac{\partial \Delta x_{o'}^2}{\partial F_{o'x}} = 0 \tag{5.51}$$

$$\frac{\partial \Delta x_{o'}^2}{\partial F_{o'y}} = \left[\frac{\Delta x}{F_x}\right]_2 \tag{5.52}$$

$$\frac{\partial \Delta x_{o'}^2}{\partial M_{o'z}} = 0 \tag{5.53}$$

By substituting Equations 5.34-5.36, 5.42-5.44 and 5.51-5.53 into Equation 5.28,

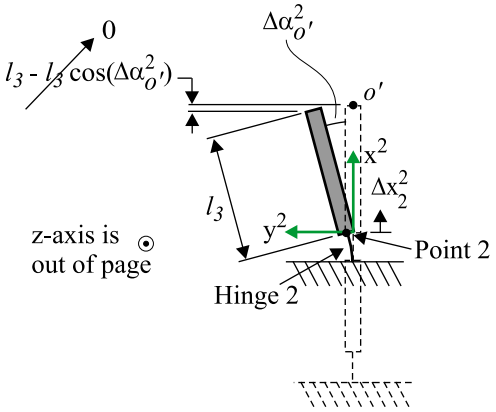

Figure 5.8: $\Delta x^2_{o'}$-displacement caused by the amplification of link with distance l_3. Dashed lines represent initial position of the four-bar compliant structure. The flexure hinge is drawn as a solid line and the rigid link is drawn as a block

the compliance matrix of the four-bar compliant structure due to Hinge 2 can be obtained.

5.1.1.3 Compliance matrices of Link 1 and 2

Since the two flexure hinges are arranged in series in the four-bar compliant structure, the overall compliances of the four-bar structure at Point o' can be calculated by summing the compliance matrices, $\mathbf{C_{h1}}$ and $\mathbf{C_{h2}}$. However, the compliance matrices $\mathbf{C_{h1}}$ and $\mathbf{C_{h2}}$ are defined using the local coordinate of x^1y^1, and x^2y^2 respectively. These local coordinates are orientated 90° from the coordinate of $x^{o'}y^{o'}$. Therefore, $\mathbf{C_{h1}}$ and $\mathbf{C_{h2}}$ need to be rotated by 90° before the summation. The rotated $\mathbf{C_{h1}}$ and $\mathbf{C_{h2}}$ are referred to as $\mathbf{C'_{h1}}$ and $\mathbf{C'_{h2}}$ respectively.

$$\mathbf{C'_{h1}} = \mathbf{T_{\pi/2}C_{h1}} \tag{5.54}$$

$$\mathbf{C'_{h2}} = \mathbf{T_{\pi/2}C_{h2}} \tag{5.55}$$

where,

$$\mathbf{T_{\pi/2}} = \begin{bmatrix} cos(\pi/2) & -sin(\pi/2) & 0 \\ sin(\pi/2) & cos(\pi/2) & 0 \\ 0 & 0 & 1 \end{bmatrix} \tag{5.56}$$

The compliance matrix at Point o' of Link 1 is,

$$\mathbf{C_{L_1o',F_{o'}}} = \mathbf{C'_{h1}} + \mathbf{C'_{h2}} \tag{5.57}$$

where the subscript "L_1" indicates Link 1 of the four-bar compliant structure. The output displacements at Point o' of Link 1 is,

$$\begin{bmatrix} \Delta x_{o'} \\ \Delta y_{o'} \\ \Delta \alpha_{o'} \end{bmatrix}_{L_1} = \mathbf{C_{L_1o',F_{o'}}} \mathbf{F_{o'}} \tag{5.58}$$

where $\mathbf{F_{o'}} = \begin{bmatrix} F_{o'x} & F_{o'y} & M_{o'z} \end{bmatrix}^T$.

When output forces are applied at Point o instead of Point o' (see Figure 5.1a) and the displacements at this point are desired, matrix $\mathbf{T_f}$ can be used to transfer the output forces from Point o to Point o'. Once $\mathbf{C_{L_1o',F_{o'}}}$ is determined using Equation 5.57, the compliances at Point o can be calculated by transforming $\mathbf{C_{L_1o',F_{o'}}}$ to Point o using a matrix, T_d. Intuitively, we know that $\Delta x_o = \Delta x_{o'}$ and $\Delta \alpha_o = \Delta \alpha_{o'}$. However, $\Delta y_o \neq \Delta y_{o'}$ due to rotational motions ($\Delta \alpha_{o'}$) and the amplification of lever arm, l_4. This link amplification effect is taken into consideration by the matrix $\mathbf{T_d}$. Displacement Δy_o of the four-bar compliant stage is illustrated in Figure 5.9.

The force transformation matrix is,

$$\mathbf{T_f} = \begin{bmatrix} 1 & 0 & 0 \\ 0 & 1 & 0 \\ 0 & -l_4 & 1 \end{bmatrix} \tag{5.59}$$

where,

$$\mathbf{F_{o'}} = \mathbf{T_f F_o} \tag{5.60}$$

and $\mathbf{F_o} = \begin{bmatrix} F_{ox} & F_{oy} & M_{oz} \end{bmatrix}^T$.

The displacement transformation matrix is,

$$\mathbf{T_d} = \begin{bmatrix} 1 & 0 & 0 \\ 0 & 1 & -l_4 \\ 0 & 0 & 1 \end{bmatrix} \tag{5.61}$$

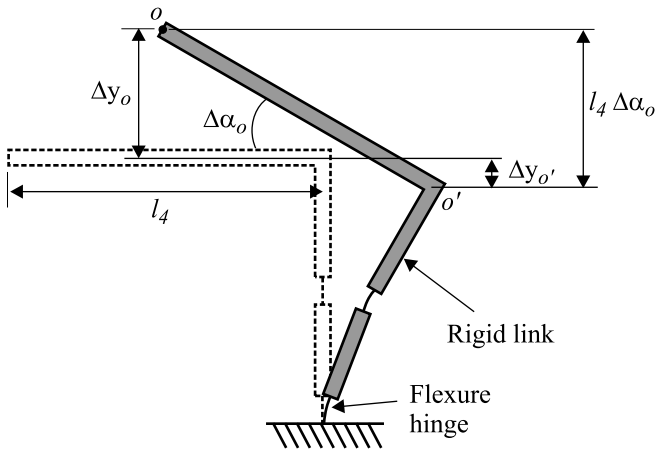

Figure 5.9: Calculation of compliances at Point o. Dashed lines represent initial position of the four-bar compliant structure. The flexure hinge is drawn as a solid line and the rigid link is drawn as a block

The output displacements at Point o of Link 1 is,

$$\begin{bmatrix} \Delta x_o \\ \Delta y_o \\ \Delta \alpha_o \end{bmatrix}_{L_1} = \mathbf{T_d C_{L_1 o', F_{o'}}} \left(\mathbf{T_f F_o} \right) \tag{5.62}$$

Therefore, the compliance of Link 1 at Point o is,

$$\mathbf{C_{L_1 o, F_o}} = \mathbf{T_d C_{L_1 o', F_{o'}} T_f} \tag{5.63}$$

Since Link 2 is a mirrored structure of Link 1 along the y^o-axis, the compliance of Link 2 at Point o can be obtained as shown below,

$$\mathbf{C_{L_2 o, F_o}} = \begin{bmatrix} \mathbf{C_{L_1 o, F_o}}(1,1) & -\mathbf{C_{L_1 o, F_o}}(1,2) & \mathbf{C_{L_1 o, F_o}}(1,3) \\ -\mathbf{C_{L_1 o, F_o}}(2,1) & \mathbf{C_{L_1 o, F_o}}(2,2) & -\mathbf{C_{L_1 o, F_o}}(2,3) \\ \mathbf{C_{L_1 o, F_o}}(3,1) & -\mathbf{C_{L_1 o, F_o}}(3,2) & \mathbf{C_{L_1 o, F_o}}(3,3) \end{bmatrix} \tag{5.64}$$

5.1.1.4 Compliance matrix $\mathbf{C_{o,F_o}}$

Since Link 1 and 2 are arranged parallel to each other (see Figure 5.2), the compliance matrix of the four-bar compliant mechanism, $\mathbf{C_{o,F_o}}$ can be found using the rule of calculating the equivalent compliances for parallel connections of springs,

$$\mathbf{C_{o,F_o}} = \left(\mathbf{C^{-1}_{L_1o,F_o}} + \mathbf{C^{-1}_{L_2o,F_o}}\right)^{-1} \tag{5.65}$$

The output displacements of the four-bar compliant mechanism due to applied forces/moment can be expressed as,

$$\begin{bmatrix} \Delta x_o \\ \Delta y_o \\ \Delta \alpha_o \end{bmatrix}_{4bar} = \mathbf{C_{o,F_o}F_o} \tag{5.66}$$

5.1.2 Derivation of the compliance matrix, $\mathbf{C_{o,F_{in}}}$ and $\mathbf{C_{in,F_o}}$

The compliance matrix, $\mathbf{C_{L_1o',F_{in}}}$ of Link 1 at Point o' due to F_{in} is firstly calculated. Then, the compliance matrix at Point o, $\mathbf{C_{L_1o,F_{in}}}$ is calculated by multiplying the transformation matrix, $\mathbf{T_d}$ to $\mathbf{C_{L_1o',F_{in}}}$.

5.1.2.1 Derivation of $\mathbf{C_{L_1o',F_{in}}}$ and $\mathbf{C_{L_1o,F_{in}}}$

When input force F_{in} is applied, compliances of Link 1 at Point o' and Point o are only affected by the compliances of Hinge 1 due to its open-chain configuration. The compliance matrix at Point o', $\mathbf{C_{L_1o',F_{in}}}$ due to Hinge 1 is expressed as,

$$\mathbf{C_{L_1o',F_{in}}} = \mathbf{T_{\pi/2}} \begin{bmatrix} \partial \Delta x^1_{o'}/\partial F_{in} \\ \partial \Delta y^1_{o'}/\partial F_{in} \\ \partial \Delta \alpha^1_{o'}/\partial F_{in} \end{bmatrix} \tag{5.67}$$

where the partial derivative terms in Equation 5.67 are derived as follows: The $\Delta\alpha^1_1$-, Δy^1_1- and Δx^1_1-displacement are derived using the local coordinate of x^1y^1. Therefore Equation 5.67 is rotated by 90°.
From Equations 5.4 , 5.11 and 5.19, $\Delta\alpha^1_1$-, Δy^1_1- and Δx^1_1-displacements are,

$$\Delta\alpha^1_1 = \left[\frac{\Delta\alpha_z}{M_z}\right]_1 \{-F_{o'x}\left(l_2 + l_3 + 2R_2\right) - F_{in}l_1 + M_{o'z}\} + \left[\frac{\Delta\alpha_z}{M_z}\right]_1 \left(-F_{o'x} - F_{in}\right) R_1$$

$$\Delta y_1^1 = -\left[\frac{\Delta y}{F_y}\right]_1 (F_{o'x} + F_{in}) + \left[\frac{\Delta \alpha_z}{M_z}\right]_1 \{-F_{o'x}(l_2 + l_3 + 2R_2) - F_{in} l_1 + M_{o'z}\} R_1$$

$$\Delta x_1^1 = \left[\frac{\Delta x}{F_x}\right]_1 F_{o'x}$$

The $\Delta\alpha_1^1$-, Δy_1^1- and Δx_1^1-compliances of Hinge 1 caused by F_{in} are obtained by taking the partial derivatives of $\Delta\alpha_1^1$, Δy_1^1 and Δx_1^1 with respect to the input force F_{in} acting at Point 1_{in} (see Figure 5.3),

$$\frac{\partial \Delta\alpha_1^1}{\partial F_{in}} = -(l_1 + R_1)\left[\frac{\Delta \alpha_z}{M_z}\right]_1 \tag{5.68}$$

$$\frac{\partial \Delta y_1^1}{\partial F_{in}} = -\left[\frac{\Delta y}{F_y}\right]_1 - (l_1 R_1)\left[\frac{\Delta \alpha_z}{M_z}\right]_1 \tag{5.69}$$

$$\frac{\partial \Delta x_1^1}{\partial F_{in}} = 0 \tag{5.70}$$

The $\Delta\alpha_{o'}^1$-displacement is the same as $\Delta\alpha_1^1$-displacement. Therefore, the results of the partial derivatives with respect to F_{in} are the same as Equation 5.68.

$$\frac{\partial \Delta\alpha_{o'}^1}{\partial F_{in}} = -(l_1 + R_1)\left[\frac{\Delta \alpha_z}{M_z}\right]_1 \tag{5.71}$$

From Equations 5.15 and 5.24, the $\Delta y_{o'}^1$- and $\Delta x_{o'}^1$-displacements are,

$$\Delta y_{o'}^1 = \Delta y_1^1 + \Delta\alpha_{o'}^1 (l_2 + l_3 + 2R_2)$$

$$\Delta x_{o'}^1 = \Delta x_1^1$$

The $\Delta y_{o'}^1$- and $\Delta x_{o'}^1$-compliances of Hinge 1 caused by F_{in} are obtained by taking the partial derivatives of $\Delta y_{o'}^1$ and $\Delta x_{o'}^1$ with respect to the input force at Point 1_{in},

$$\begin{aligned}\frac{\partial \Delta y^1_{o'}}{\partial F_{in}} &= \frac{\partial \Delta y^1_1}{\partial F_{in}} + \frac{\partial \Delta \alpha^1_{o'}}{\partial F_{in}} (l_2 + l_3 + 2R_2) \\ &= \left\{ -\left[\frac{\Delta y}{F_y}\right]_1 - (l_1 R_1) \left[\frac{\Delta \alpha_z}{M_z}\right]_1 \right\} + \left\{ -(l_1 + R_1) \left[\frac{\Delta \alpha_z}{M_z}\right]_1 (l_2 + l_3 + 2R_2) \right\} \\ &= -\left[\frac{\Delta y}{F_y}\right]_1 - \left\{ l_1 R_1 + (l_2 + l_3 + 2R_2)(l_1 + R_1) \left[\frac{\Delta \alpha_z}{M_z}\right]_1 \right\} \end{aligned} \tag{5.72}$$

$$\begin{aligned}\frac{\partial \Delta x^1_{o'}}{\partial F_{in}} &= \frac{\partial \Delta x^1_1}{\partial F_{in}} \\ &= 0 \end{aligned} \tag{5.73}$$

By substituting Equations 5.71, 5.72 and 5.73 into Equation 5.67, $\mathbf{C_{L_1 o', F_{in}}}$ can be found.
The compliance matrix at Point o, $\mathbf{C_{L_1 o, F_{in}}}$is,

$$\mathbf{C_{L_1 o, F_{in}}} = \mathbf{T_d C_{L_1 o', F_{in}}} \tag{5.74}$$

5.1.2.2 Derivation of $\mathbf{C_{o, F_{in}}}$

The output displacement of Link 1, $\mathbf{D_{L_1 o, F_{in}}}$ at Point o due to input force F_{in} is,

$$\mathbf{D_{L_1 o, F_{in}}} = \mathbf{C_{L_1 o, F_{in}}} F_{in} \tag{5.75}$$

By using Equation 5.63, the output displacement of Link 1, $\mathbf{D_{L_1 o, F_o}}$ at Point o due to output force $\mathbf{F_o}$ is,

$$\mathbf{D_{L_1 o, F_o}} = \mathbf{C_{L_1 o, F_o} F_o} \tag{5.76}$$

By equating Equations 5.75 and 5.76, the equivalent output force $\mathbf{F_{L_1 o, eqv}}$ at Point o when $F_{in} = 1$N (unit force) can be calculated as below, where $\mathbf{F_{L_1 o, eqv}} = \mathbf{F_o}$ in Equation 5.76,

$$\mathbf{F_{L_1 o, eqv}} = \left[\mathbf{C_{L_1 o, F_o}}\right]^{-1} \mathbf{C_{L_1 o, F_{in}}} \tag{5.77}$$

By multiplying the equivalent output force $\mathbf{F_{L_1 o, eqv}}$ to $\mathbf{C_{o, F_o}}$, the output displacement of the four-bar compliant structure caused by F_{in} from Link 1 can be found. Since a unit force of F_{in} is used to calculate the equivalent output force, the output displacement obtained can also represent the output compliance of the stage caused by F_{in},

$$\mathbf{C_{o,F_{in}}} = \mathbf{D_{o,F_{in}}} = \mathbf{C_{o,F_o}}\mathbf{F_{L_1o,eqv}} \tag{5.78}$$

$\mathbf{C_{in,F_o}}$ is the transpose of $\mathbf{C_{o,F_{in}}}$ and can be obtained as below,

$$\mathbf{C_{in,F_o}} = [\mathbf{C_{o,F_{in}}}]^T \tag{5.79}$$

5.1.3 Derivation of the compliance matrix, $C_{in,F_{in}}$

The input displacements, $u_{in,F_{in}}$ due to input force F_{in} can be calculated as below, where $\mathbf{C_{in,F_o}}$ is obtained from Equation 5.79 and $\mathbf{F_{L_1o,eqv}}$ is obtained from Equation 5.77. Note that $\mathbf{F_{L_1o,eqv}}$ is the equivalent force calculated at Point o when input force F_{in} is applied at Link 1. Since a unit force of F_{in} is used to obtain the equivalent output force, the input displacements $u_{in,F_{in}}$ obtained can also represent the input compliances of the stage caused by F_{in},

$$\begin{aligned} C_{in,F_{in}} &= u_{in,F_{in}} \\ &= \mathbf{C_{in,F_o}}\mathbf{F_{L_1o,eqv}} \end{aligned} \tag{5.80}$$

where $u_{in,F_{in}}$ is the displacement at Point 1_{in} (see Figure 5.1) of the four-bar compliant mechanism due to F_{in}.

5.1.4 The Jacobian matrix of four-bar compliant mechanisms

The relationship between the input and output displacements can be derived from Equation 5.1 for a given F_o. For example, when there is no external force, $F_o = 0$, and therefore,

$$\mathbf{U_o} = \mathbf{C_{o,F_{in}}}F_{in} \tag{5.81}$$

$$F_{in} = \mathbf{C_{o,F_{in}}^{-1}}\mathbf{U_o} \tag{5.82}$$

and,

$$U_{in} = C_{in,F_{in}}F_{in} \tag{5.83}$$

$$F_{in} = C_{in,F_{in}}^{-1}U_{in} \tag{5.84}$$

By equating Equation 5.82 and Equation 5.84 ,

$$\mathbf{U_o} = \mathbf{C_{o,F_{in}}} C^{-1}_{in,F_{in}} U_{in} \tag{5.85}$$

A constant Jacobian matrix is used in this thesis (as explained in Section 4.2) to relate the output displacements ($\mathbf{U_o}$) to the input displacements (U_{in}) of the compliant mechanisms; therefore the Jacobian matrix is defined as below,

$$\mathbf{J} = \mathbf{C_{o,F_{in}}} C^{-1}_{in,F_{in}} \tag{5.86}$$

5.1.5 Case studies of the four-bar compliant mechanism

For comparison purposes, the four-bar compliant mechanism studied in this section is the same as that in Chapter 4. Material properties, link lengths and flexure hinge dimensions of the mechanism are shown in Table 5.2.

Two cases were studied where analytical matrices of the kinetostatic model of Case 1 were calculated by deliberately choosing the flexure hinge equations with large differences when compared to the FEA results (refer to Figures 3.12-3.14). Meanwhile, analytical matrices of Case 2 were obtained by choosing the flexure hinge equations with small differences (refer to Figures 3.12-3.14 and Table 3.9). Table 5.3 shows the flexure hinge equations chosen from various published research studies for Cases 1 and 2 respectively. Table 5.4 shows the analytical results of Cases 1 and 2. Since $\mathbf{C_{o,F_{in}}} = \mathbf{C^{-1}_{in,F_o}}$, the result of $\mathbf{C_{o,F_{in}}}$ is not repeated in Table 5.4.

Material properties	
E	71.7 GPa
Poisson's ratio, v	0.33

Link length	l_1	l_2	l_3	l_4
(mm)	2	4	0	10

Flexure hinge	t_1, t_2	R_1, R_2	t_1/R_1, t_2/R_2	b
(mm)	1	3	0.33	5

Table 5.2: Material properties, link lengths and flexure hinge dimensions of the four-bar compliant mechanism

Case 1

t/R	$\Delta\alpha_z/M_z$	$\Delta y/F_y$	$\Delta x/F_x$
0.33	Paros and Weisbord (1965) (Full) / Lobontiu (2003) / Wu and Zhou (2002)	Schotborgh *et al.* (2005)	Schotborgh *et al.* (2005)

Case 2

t/R	$\Delta\alpha_z/M_z$	$\Delta y/F_y$	$\Delta x/F_x$
0.33	Schotborgh *et al.* (2005)	This thesis (Equation 3.19)	This thesis (Equation 3.17)

Table 5.3: Flexure hinge equations chosen for Cases 1 and 2 for the derivation of kinetostatics of the four-bar compliant mechanism

Case 1	Analytical results
$\mathbf{C_{o,F_o}}$ ($\mu m/N$, $\mu rad/N$ $\mu m/Nm$, $\mu rad/Nm$)	$\begin{matrix} 1.14 & 0 & -1.18 \\ 0 & 0.01 & 0 \\ -1.18 & 0 & 147.04 \end{matrix}$
$\mathbf{C_{in,F_o}}$ ($\mu m/N$, $\mu rad/N$)	$0.57 \quad 0 \quad -0.37$
$C_{in,F_{in}}$ ($\mu m/N$)	0.283
$\mathbf{J}_{analytical,4bar}$	$\begin{matrix} 2.001 \\ 0 \\ -1.27 \end{matrix}$

Case 2	Analytical results
$\mathbf{C_{o,F_o}}$ ($\mu m/N$, $\mu rad/N$ $\mu m/Nm$, $\mu rad/Nm$)	$\begin{matrix} 1.92 & 0 & -0.81 \\ 0 & 0.01 & 0 \\ -0.81 & 0 & 100.62 \end{matrix}$
$\mathbf{C_{in,F_o}}$ ($\mu m/N$, $\mu rad/N$)	$0.96 \quad 0 \quad -0.25$
$C_{in,F_{in}}$ ($\mu m/N$)	0.48
$\mathbf{J}_{analytical,4bar}$	$\begin{matrix} 2.002 \\ 0 \\ -0.52 \end{matrix}$

Table 5.4: Case studies - Analytical matrices of the kinetostatic model of the four-bar compliant mechanism

5.1.5.1 Discussion

The resulting compliance and Jacobian of the two cases in Table 5.4 suggest that the four-bar compliant mechanism has high translational stiffness in the y^o-direction and high rotational stiffness along the z^o-direction which are in agreement to the one-DOF characteristic of a four-bar mechanism. It can also be observed that the analytical results of Cases 1 and 2 are noticeably different except for the transla-

tional term in the Jacobian matrix. The translational terms (Δx_o) of the two Jacobian matrices are similar but the rotational terms ($\Delta \alpha_o$) are different. The similarity of the Δx_o terms in the Jacobian matrices is explained by the fact that the Jacobian represents the kinematics of the micro-motion structures; therefore the Jacobian is almost independent of the compliances or stiffnesses of flexure hinges. The choice of flexure hinge equations used to calculate the analytical results has minimal effects on the results of the Jacobian matrix. The choice of flexure hinge equations influence the $\Delta \alpha_o$ term of the Jacobian matrix by a very small amount, which is 0.75 $\mu rad/\mu m$. This influence on the $\Delta \alpha_o$ term is insignificant. The analytical Jacobian results will be compared to the FEA and experimental results to justify their accuracies.

The differences between the compliance results of Cases 1 and 2 suggest that the choice of flexure hinge compliance equations affects the results of the kinetostatic model. Since the kinetostatic model is derived to have flexure hinge compliances as one of the variables, flexure hinge equations with small differences when compared to FEA results can be selected based on the scheme developed in Chapter 3, and these hinge equations can be incorporated into the kinetostatic model to accurately predict both the kinematics and statics of compliant mechanisms. The modelling results of Cases 1 and 2 will be compared to the FEA and experimental results in Chapters 6 and 7 in order to verify their accuracies.

5.2 Kinetostatic modelling of 3-RRR micro-motion stages

The kinetostatic model of a 3-RRR micro-motion stage is shown below,

$$\begin{bmatrix} \mathbf{U_o} \\ \mathbf{U_{in}} \end{bmatrix} = \begin{bmatrix} \mathbf{C_{o,F_o}} & \mathbf{C_{o,F_{in}}} \\ \mathbf{C_{in,F_o}} & \mathbf{C_{in,F_{in}}} \end{bmatrix} \begin{bmatrix} \mathbf{F_o} \\ \mathbf{F_{in}} \end{bmatrix} \tag{5.87}$$

where $\mathbf{U_o} = \begin{bmatrix} \Delta x_o & \Delta y_o & \Delta \alpha_o \end{bmatrix}^T$ is a 3x1 matrix representing the output displacements of the stage,
$\mathbf{U_{in}} = \begin{bmatrix} u_{1in} & u_{2in} & u_{3in} \end{bmatrix}^T$ is a 3x1 matrix representing the input displacements of the stage,
$\mathbf{F_o} = \begin{bmatrix} F_{ox} & F_{oy} & M_{oz} \end{bmatrix}^T$ is a 3x1 matrix representing the output forces/moment acting at Point o,
$\mathbf{F_{in}} = \begin{bmatrix} F_{1in} & F_{2in} & F_{3in} \end{bmatrix}^T$ is a 3x1 matrix representing the input forces,
$\mathbf{C_{o,F_o}}$ is a 3x3 compliance matrix relating the output displacements to the output forces /moment,
$\mathbf{C_{o,F_{in}}}$ is a 3x3 compliance matrix relating the output displacements to the input forces,
$\mathbf{C_{in,F_o}}$ is a 3x3 compliance matrix relating the input displacements to the output forces/moment,
$\mathbf{C_{in,F_{in}}}$ is a 3x3 compliance matrix relating the input displacements to the input forces.

5.2.1 Derivation of the output compliance matrix, $\mathbf{C_{o,F_o}}$

Due to the symmetrical structure of the 3-RRR compliant micro-motion stage (see Figure 5.10), the 3-RRR structure can be divided into three links in order to calculate the $\mathbf{C_{o,F_o}}$ matrix. Each link consists of a RRR topology which has three flexure hinges. The flexure hinge compliances are $[\Delta\alpha_z/M_z]_j$, $[\Delta y/F_y]_j$ and $[\Delta x/F_x]_j$, where j =1, 2, 3. The RRR compliant structure is shown in Figure 5.10b together with its dimensions, displacements, local coordinates of flexure hinges and the applied forces/moment. The compliances at Point o' contributed by each flexure hinge in the structure are firstly calculated. These compliance matrices are named $\mathbf{C_{h1}}$, $\mathbf{C_{h2}}$ and $\mathbf{C_{h3}}$. The three flexure hinges of the RRR structure are arranged in series; therefore the compliance matrix of the RRR structure at Point o' can be ob-

tained by summing $\mathbf{C_{h1}}$, $\mathbf{C_{h2}}$ and $\mathbf{C_{h3}}$ together. The compliance matrices of the three RRR links are referred to as $\mathbf{C_{L1o,F_o}}$, $\mathbf{C_{L2o,F_o}}$ and $\mathbf{C_{L3o,F_o}}$ respectively. The three RRR links of the 3-RRR compliant structure are arranged in parallel; therefore $\mathbf{C_{o,F_o}}$ matrix in Equation 5.87 is calculated by summing $\mathbf{C_{L1o,F_o}}$, $\mathbf{C_{L2o,F_o}}$ and $\mathbf{C_{L3o,F_o}}$ using the rule of parallel connection of springs (see Figure 5.11).

5.2.1.1 Compliances of the RRR mechanism due to Hinge 1

The compliance matrix of the RRR mechanism due to Hinge 1 is expressed as,

$$\mathbf{C_{h1}} = \begin{bmatrix} \partial\Delta x^1_{o'}/\partial F_{o'x} & \partial\Delta x^1_{o'}/\partial F_{o'y} & \partial\Delta x^1_{o'}/\partial M_{o'z} \\ \partial\Delta y^1_{o'}/\partial F_{o'x} & \partial\Delta y^1_{o'}/\partial F_{o'y} & \partial\Delta y^1_{o'}/\partial M_{o'z} \\ \partial\Delta \alpha^1_{o'}/\partial F_{o'x} & \partial\Delta \alpha^1_{o'}/\partial F_{o'y} & \partial\Delta \alpha^1_{o'}/\partial M_{o'z} \end{bmatrix} \tag{5.88}$$

where the partial derivative terms in Equation 5.88 are derived as follows:

From Figure 5.12, forces/moment acting at Point o' and Point 1_{in}[†] can be resolved into forces/moment acting at Point 1 as follows.

$$\begin{aligned} F_{1x} &= F_{o'x} \\ F_{1y} &= F_{o'y} - F_{1in} \\ M_{1z} &= -F_{o'x}l_4 + F_{o'y}l_1 + M_{o'z} - F_{1in}l_5 \end{aligned} \tag{5.89}$$

Derivation of $\partial\Delta\alpha^1_{o'}/\partial F_{o'x}$, $\partial\Delta\alpha^1_{o'}/\partial F_{o'y}$ ***and*** $\partial\Delta\alpha^1_{o'}/\partial M_{o'z}$

The rotational displacements about the z-axis, $\Delta\alpha^1_1$-displacement at Point 1 is,

$$\begin{aligned} \Delta\alpha^1_1 &= \left[\frac{\Delta\alpha_z}{M_z}\right]_1 M_{1z} + \left[\frac{\Delta\alpha_z}{M_z}\right]_1 F_{1y}R_1 \\ &= \left[\frac{\Delta\alpha_z}{M_z}\right]_1 (-F_{o'x}l_4 + F_{o'y}l_1 + M_{o'z} - F_{1in}l_5) + \left[\frac{\Delta\alpha_z}{M_z}\right]_1 (F_{o'y} - F_{1in})\, R_1 \\ &= \left[\frac{\Delta\alpha_z}{M_z}\right]_1 \{-F_{o'x}l_4 + F_{o'y}\,(l_1 + R_1) + M_{o'z} - F_{1in}\,(l_5 + R_1)\} \end{aligned} \tag{5.90}$$

The $\Delta\alpha^1_1$-compliances of Hinge 1 caused by $F_{o'x}$, $F_{o'y}$ and $M_{o'z}$ are obtained by taking the partial derivatives of $\Delta\alpha^1_1$ with respect to the forces/moment acting at

[†]Input forces acting at this point are going to be used to calculate compliance matrices $\mathbf{C_{o,F_{in}}}$, $\mathbf{C_{F_{in},o}}$ and $\mathbf{C_{in,F_{in}}}$ later in this chapter.

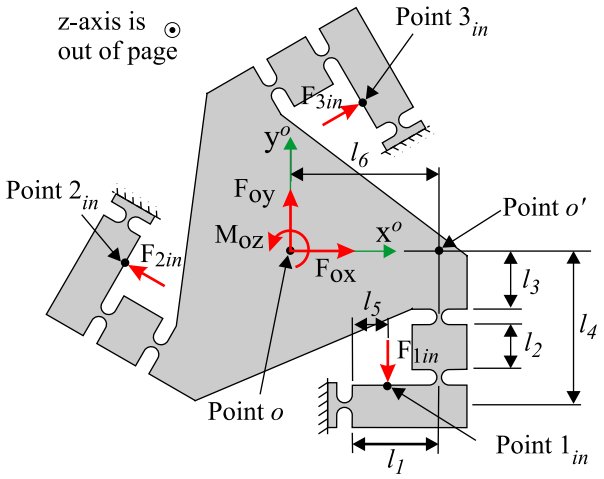

(a) 3-RRR compliant mechanism

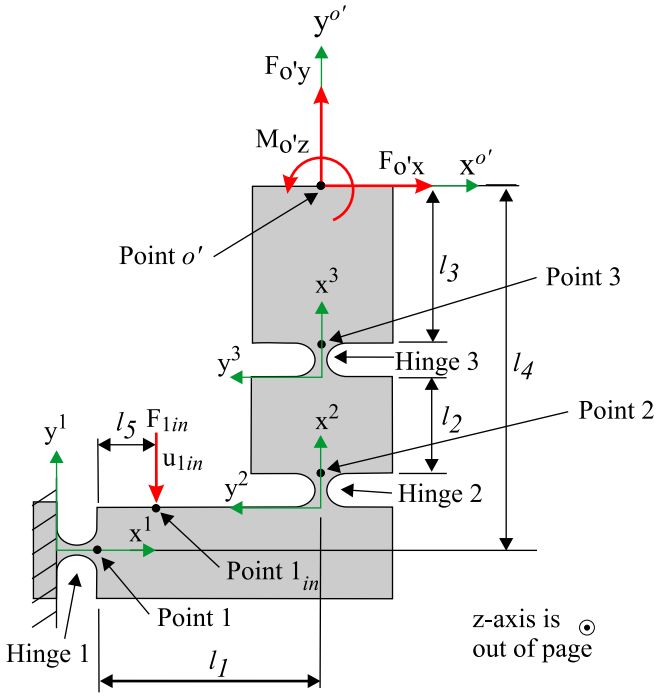

(b) RRR compliant mechanism

Figure 5.10: 3-RRR compliant micro-motion stage

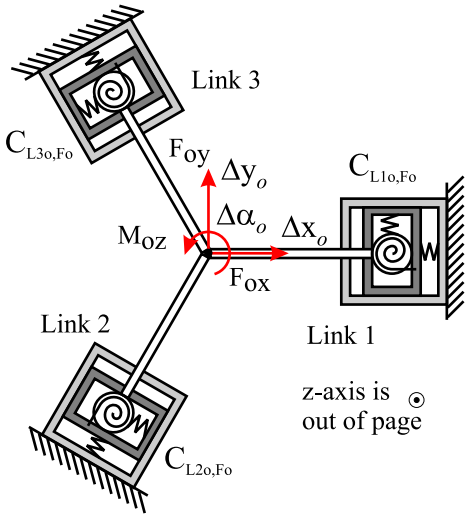

Figure 5.11: Parallel spring model of a 3-RRR micro-motion stage

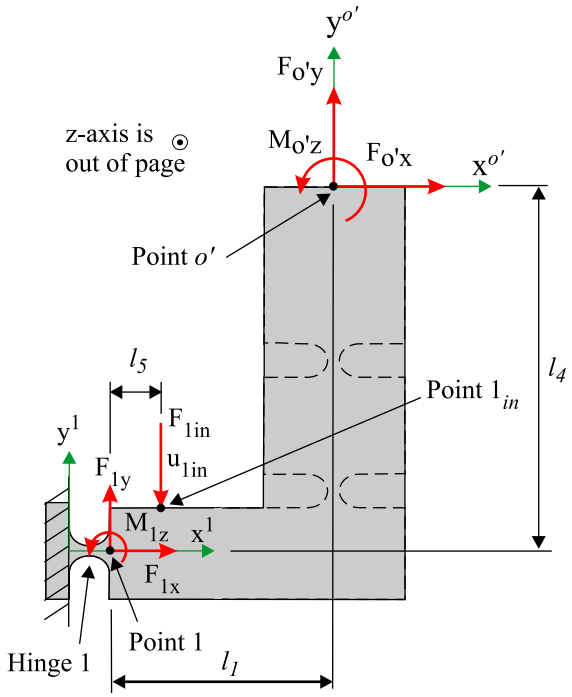

Figure 5.12: Compliances due to Hinge 1

Point o',

$$\frac{\partial \Delta\alpha_1^1}{\partial F_{o'x}} = -l_4 \left[\frac{\Delta\alpha_z}{M_z}\right]_1 \tag{5.91}$$

$$\frac{\partial \Delta\alpha_1^1}{\partial F_{o'y}} = (l_1 + R_1) \left[\frac{\Delta\alpha_z}{M_z}\right]_1 \tag{5.92}$$

$$\frac{\partial \Delta\alpha_1^1}{\partial M_{o'z}} = \left[\frac{\Delta\alpha_z}{M_z}\right]_1 \tag{5.93}$$

The results of the partial derivatives of $\Delta\alpha_1^1$ in Equations 5.91, 5.92 and 5.93 describe the relationship between the $\Delta\alpha_1^1$-displacement and the forces/moment.

The rotational displacements, $\Delta\alpha_{o'}^1$-displacement at Point o' is the same as $\Delta\alpha_1^1$-displacement. Therefore, their results of the partial derivatives are the same as Equations 5.91, 5.92 and 5.93,

$$\frac{\partial \Delta\alpha_{o'}^1}{\partial F_{o'x}} = -l_4 \left[\frac{\Delta\alpha_z}{M_z}\right]_1 \tag{5.94}$$

$$\frac{\partial \Delta\alpha_{o'}^1}{\partial F_{o'y}} = (l_1 + R_1) \left[\frac{\Delta\alpha_z}{M_z}\right]_1 \tag{5.95}$$

$$\frac{\partial \Delta\alpha_{o'}^1}{\partial M_{o'z}} = \left[\frac{\Delta\alpha_z}{M_z}\right]_1 \tag{5.96}$$

Derivation of $\partial\Delta y_{o'}^1/\partial F_{o'x}$, $\partial\Delta y_{o'}^1/\partial F_{o'y}$ ***and*** $\partial\Delta y_{o'}^1/\partial M_{o'z}$

The translational displacements along the y-axis, Δy_1^1-displacement at Point 1 is,

$$\begin{aligned}
\Delta y_1^1 &= \left[\frac{\Delta y}{F_y}\right]_1 F_{1y} + \left[\frac{\Delta\alpha_z}{M_z}\right]_1 M_{1z} R_1 \\
&= \left[\frac{\Delta y}{F_y}\right]_1 (F_{o'y} - F_{1in}) \\
&\quad + \left[\frac{\Delta\alpha_z}{M_z}\right]_1 (-F_{o'x} l_4 + F_{o'y} l_1 + M_{o'z} - F_{1in} l_5)\, R_1
\end{aligned} \tag{5.97}$$

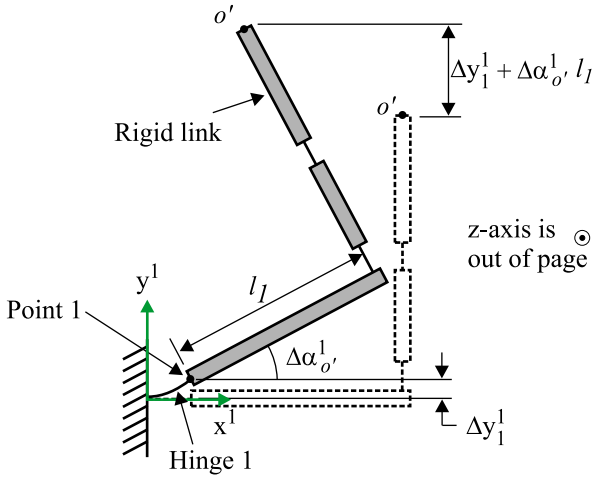

Figure 5.13: $\Delta y_{o'}^1$-displacement caused by the amplification of link, l_1. Dashed lines represent initial position of the RRR structure. The flexure hinge is drawn as a solid line and the rigid link is drawn as a block

The Δy_1^1-compliances of Hinge 1 caused by $F_{o'x}$, $F_{o'y}$ and $M_{o'z}$ are obtained by taking the partial derivatives of Δy_1^1 with respect to the forces/moment acting at Point o',

$$\frac{\partial \Delta y_1^1}{\partial F_{o'x}} = -l_4 R_1 \left[\frac{\Delta\alpha_z}{M_z}\right]_1 \tag{5.98}$$

$$\frac{\partial \Delta y_1^1}{\partial F_{o'y}} = \left[\frac{\Delta y}{F_y}\right]_1 + l_1 R_1 \left[\frac{\Delta\alpha_z}{M_z}\right]_1 \tag{5.99}$$

$$\frac{\partial \Delta y_1^1}{\partial M_{o'z}} = R_1 \left[\frac{\Delta\alpha_z}{M_z}\right]_1 \tag{5.100}$$

Due to the amplification of the link with distance l_1, the translational displacements, $\Delta y_{o'}^1$-displacement at Point o' is the summation of Δy_1^1-displacement at Point 1 and the amplified displacements caused by the rotational motions of the link (see Figure 5.13). Therefore, the $\Delta y_{o'}^1$-displacement is,

$$\Delta y_{o'}^1 = \Delta y_1^1 + \Delta\alpha_{o'}^1 l_1 \tag{5.101}$$

The $\Delta y^1_{o'}$-compliances of Hinge 1 caused by $F_{o'x}$, $F_{o'y}$ and $M_{o'z}$ are obtained by taking the partial derivatives of $\Delta y^1_{o'}$ with respect to all the forces/moment acting at Point o',

$$\begin{aligned}\frac{\partial \Delta y^1_{o'}}{\partial F_{o'x}} &= \frac{\partial \Delta y^1_1}{\partial F_{o'x}} + \frac{\partial \Delta \alpha^1_{o'}}{\partial F_{o'x}} l_1 \\ &= -l_4 R_1 \left[\frac{\Delta \alpha_z}{M_z}\right]_1 + \left(-l_4 \left[\frac{\Delta \alpha_z}{M_z}\right]_1 l_1\right) \\ &= -l_4 \left(l_1 + R_1\right) \left[\frac{\Delta \alpha_z}{M_z}\right]_1 \end{aligned} \tag{5.102}$$

$$\begin{aligned}\frac{\partial \Delta y^1_{o'}}{\partial F_{o'y}} &= \frac{\partial \Delta y^1_1}{\partial F_{o'y}} + \frac{\partial \Delta \alpha^1_{o'}}{\partial F_{o'y}} l_1 \\ &= \left[\frac{\Delta y}{F_y}\right]_1 + l_1 R_1 \left[\frac{\Delta \alpha_z}{M_z}\right]_1 + \left(l_1 + R_1\right) \left[\frac{\Delta \alpha_z}{M_z}\right]_1 l_1 \\ &= \left[\frac{\Delta y}{F_y}\right]_1 + \left\{l_1 R_1 + l_1 \left(l_1 + R_1\right)\right\} \left[\frac{\Delta \alpha_z}{M_z}\right]_1 \end{aligned} \tag{5.103}$$

$$\begin{aligned}\frac{\partial \Delta y^1_{o'}}{\partial M_{o'z}} &= \frac{\partial \Delta y^1_1}{\partial M_{o'z}} + \frac{\partial \Delta \alpha^1_{o'}}{\partial M_{o'z}} l_1 \\ &= R_1 \left[\frac{\Delta \alpha_z}{M_z}\right]_1 + \left[\frac{\Delta \alpha_z}{M_z}\right]_1 l_1 \\ &= \left(l_1 + R_1\right) \left[\frac{\Delta \alpha_z}{M_z}\right]_1 \end{aligned} \tag{5.104}$$

Derivation of $\partial \Delta x^1_{o'}/\partial F_{o'x}$, $\partial \Delta x^1_{o'}/\partial F_{o'y}$ ***and*** $\partial \Delta x^1_{o'}/\partial M_{o'z}$

The translational displacements along the x-axis, Δx^1_1-displacement at Point 1 is,

$$\begin{aligned}\Delta x^1_1 &= \left[\frac{\Delta x}{F_x}\right]_1 F_{1x} \\ &= \left[\frac{\Delta x}{F_x}\right]_1 F_{o'x} \end{aligned} \tag{5.105}$$

The Δx^1_1-compliances of Hinge 1 caused by $F_{o'x}$, $F_{o'y}$ and $M_{o'z}$ are obtained by taking the partial derivatives of Δx^1_1 with respect to the forces/moment acting at Point o',

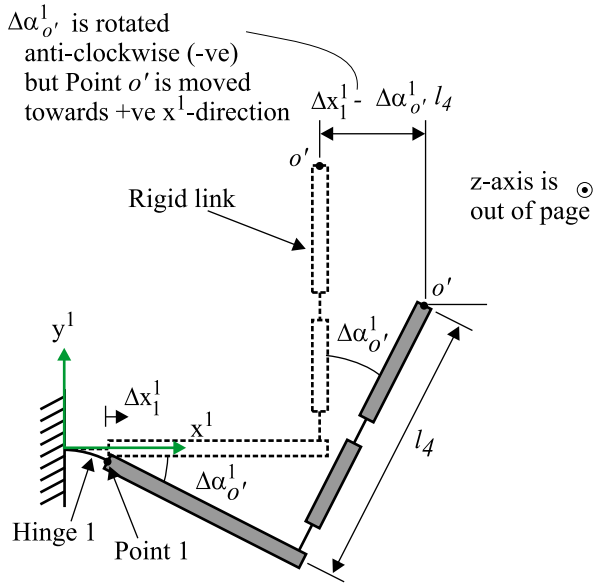

Figure 5.14: $\Delta x^1_{o'}$-displacement caused by the amplification of link with distance l_4. Dashed lines represent initial position of the RRR structure. The flexure hinge is drawn as a solid line and the rigid link is drawn as a block.

$$\frac{\partial \Delta x^1_1}{\partial F_{o'x}} = \left[\frac{\Delta x}{F_x}\right]_1 \tag{5.106}$$

$$\frac{\partial \Delta x^1_1}{\partial F_{o'y}} = 0 \tag{5.107}$$

$$\frac{\partial \Delta x^1_1}{\partial M_{o'z}} = 0 \tag{5.108}$$

Due to the amplification of the link with distance l_4, the translational displacements, $\Delta x^1_{o'}$-displacement at Point o' is the summation of Δx^1_1-displacement at Point 1 and the amplified displacements caused by the rotational motions of the link (see Figure 5.14). Therefore, the $\Delta x^1_{o'}$-displacement is,

$$\Delta x^1_{o'} \;=\; \Delta x^1_1 - \Delta\alpha^1_{o'} l_4 \tag{5.109}$$

The negative sign of $\Delta\alpha^1_{o'} l_4$ is due to the fact that when $\Delta\alpha^1_{o'}$ is rotated towards the anti-clockwise direction (negative rotations), Point o' is moved towards the positive Δx^1-direction.

The $\Delta x^1_{o'}$-compliances of Hinge 1 caused by $F_{o'x}$, $F_{o'y}$ and $M_{o'z}$ are obtained by taking the partial derivatives of $\Delta x^1_{o'}$ with respect to the forces/moment acting at

Point o',

$$\begin{aligned}\frac{\partial \Delta x^1_{o'}}{\partial F_{o'x}} &= \frac{\partial \Delta x^1_1}{\partial F_{o'x}} - \frac{\partial \Delta \alpha^1_{o'}}{\partial F_{o'x}} l_4 \\ &= \left[\frac{\Delta x}{F_x}\right]_1 - \left(-l_4 \left[\frac{\Delta \alpha_z}{M_z}\right]_1 l_4\right) \\ &= \left[\frac{\Delta x}{F_x}\right]_1 + l_4^2 \left[\frac{\Delta \alpha_z}{M_z}\right]_1 \end{aligned} \tag{5.110}$$

$$\begin{aligned}\frac{\partial \Delta x^1_{o'}}{\partial F_{o'y}} &= \frac{\partial \Delta x^1_1}{\partial F_{o'y}} - \frac{\partial \Delta \alpha^1_{o'}}{\partial F_{o'y}} l_4 \\ &= -l_4 \left(l_1 + R_1\right) \left[\frac{\Delta \alpha_z}{M_z}\right]_1 \end{aligned} \tag{5.111}$$

$$\begin{aligned}\frac{\partial \Delta x^1_{o'}}{\partial M_{o'z}} &= \frac{\partial \Delta x^1_1}{\partial M_{o'z}} - \frac{\partial \Delta \alpha^1_{o'}}{\partial M_{o'z}} l_4 \\ &= -l_4 \left[\frac{\Delta \alpha_z}{M_z}\right]_1 \end{aligned} \tag{5.112}$$

By substituting Equations 5.94-5.96, 5.102-5.104 and 5.110-5.112 into Equation 5.88, the compliance matrix of the RRR structure due to Hinge 1, $\mathbf{C_{h1}}$ can be obtained.

5.2.1.2 Compliances of the RRR mechanism due to Hinge 2

The compliance matrix of the RRR structure due to Hinge 2 is expressed as,

$$\mathbf{C_{h2}} = \begin{bmatrix} \partial \Delta x^2_{o'}/\partial F_{o'x} & \partial \Delta x^2_{o'}/\partial F_{o'y} & \partial \Delta x^2_{o'}/\partial M_{o'z} \\ \partial \Delta y^2_{o'}/\partial F_{o'x} & \partial \Delta y^2_{o'}/\partial F_{o'y} & \partial \Delta y^2_{o'}/\partial M_{o'z} \\ \partial \Delta \alpha^2_{o'}/\partial F_{o'x} & \partial \Delta \alpha^2_{o'}/\partial F_{o'y} & \partial \Delta \alpha^2_{o'}/\partial M_{o'z} \end{bmatrix} \tag{5.113}$$

The procedures of deriving all the components of $\mathbf{C_{h2}}$ in Equation 5.113 is the same as that presented in Section 5.1.1.1. Therefore, the detailed procedures will not be presented again in this section.

Derivation of $\partial\Delta\alpha_{o'}^2/\partial F_{o'x}$, $\partial\Delta\alpha_{o'}^2/\partial F_{o'y}$ ***and*** $\partial\Delta\alpha_{o'}^2/\partial M_{o'z}$

$$\frac{\partial\Delta\alpha_{o'}^2}{\partial F_{o'x}} = -\left(l_2+l_3+2R_3+R_2\right)\left[\frac{\Delta\alpha_z}{M_z}\right]_2 \tag{5.114}$$

$$\frac{\partial\Delta\alpha_{o'}^2}{\partial F_{o'y}} = 0 \tag{5.115}$$

$$\frac{\partial\Delta\alpha_{o'}^2}{\partial M_{o'z}} = \left[\frac{\Delta\alpha_z}{M_z}\right]_2 \tag{5.116}$$

Derivation of $\partial\Delta y_{o'}^2/\partial F_{o'x}$, $\partial\Delta y_{o'}^2/\partial F_{o'y}$ ***and*** $\partial\Delta y_{o'}^2/\partial M_{o'z}$

$$\begin{aligned}\frac{\partial\Delta y_{o'}^2}{\partial F_{o'x}} &= \frac{\partial\Delta y_2^2}{\partial F_{o'x}}+\frac{\partial\Delta\alpha_{o'}^2}{\partial F_{o'x}}\left(l_2+l_3+2R_3\right)\\ &= -\left[\frac{\Delta y}{F_y}\right]_2-\left\{\left(l_2+l_3+2R_3\right)R_2\right.\\ &\quad\left.+\left(l_2+l_3+2R_3\right)\left(l_2+l_3+2R_3+R_2\right)\right\}\left[\frac{\Delta\alpha_z}{M_z}\right]_2\end{aligned} \tag{5.117}$$

$$\begin{aligned}\frac{\partial\Delta y_{o'}^2}{\partial F_{o'y}} &= \frac{\partial\Delta y_2^2}{\partial F_{o'y}}+\frac{\partial\Delta\alpha_{o'}^2}{\partial F_{o'y}}\left(l_2+l_3+2R_3\right)\\ &= 0\end{aligned} \tag{5.118}$$

$$\begin{aligned}\frac{\partial\Delta y_{o'}^2}{\partial M_{o'z}} &= \frac{\partial\Delta y_2^2}{\partial M_{o'z}}+\frac{\partial\Delta\alpha_{o'}^2}{\partial M_{o'z}}\left(l_2+l_3+2R_3\right)\\ &= \left(l_2+l_3+R_2+2R_3\right)\left[\frac{\Delta\alpha_z}{M_z}\right]_2\end{aligned} \tag{5.119}$$

Derivation of $\partial\Delta x_{o'}^2/\partial F_{o'x}$, $\partial\Delta x_{o'}^2/\partial F_{o'y}$ ***and*** $\partial\Delta x_{o'}^2/\partial M_{o'z}$

$$\frac{\partial\Delta x_{o'}^2}{\partial F_{o'x}} = 0 \tag{5.120}$$

$$\frac{\partial\Delta x_{o'}^2}{\partial F_{o'y}} = \left[\frac{\Delta x}{F_x}\right]_2 \tag{5.121}$$

$$\frac{\partial \Delta x^2_{o'}}{\partial M_{o'z}} = 0 \tag{5.122}$$

By substituting Equations 5.114-5.116, 5.117-5.119 and 5.120-5.122 into Equation 5.113, the compliance matrix of the RRR structure due to Hinge 2, $\mathbf{C_{h2}}$ can be obtained.

5.2.1.3 Compliances of the RRR mechanism due to Hinge 3

The compliance matrix of the RRR structure due to Hinge 3 is expressed as,

$$\mathbf{C_{h3}} = \begin{bmatrix} \partial \Delta x^3_{o'}/\partial F_{o'x} & \partial \Delta x^3_{o'}/\partial F_{o'y} & \partial \Delta x^3_{o'}/\partial M_{o'z} \\ \partial \Delta y^3_{o'}/\partial F_{o'x} & \partial \Delta y^3_{o'}/\partial F_{o'y} & \partial \Delta y^3_{o'}/\partial M_{o'z} \\ \partial \Delta \alpha^3_{o'}/\partial F_{o'x} & \partial \Delta \alpha^3_{o'}/\partial F_{o'y} & \partial \Delta \alpha^3_{o'}/\partial M_{o'z} \end{bmatrix} \tag{5.123}$$

The procedure of deriving all the components of $\mathbf{C_{h3}}$ in Equation 5.123 is the same as that presented in Section 5.1.1.2. Therefore, the detailed procedure will not be presented again in this section.

Derivation of $\partial \Delta \alpha^3_{o'}/\partial F_{o'x}$, $\partial \Delta \alpha^3_{o'}/\partial F_{o'y}$ ***and*** $\partial \Delta \alpha^3_{o'}/\partial M_{o'z}$

$$\frac{\partial \Delta \alpha^3_{o'}}{\partial F_{o'x}} = -(l_3 + R_3)\left[\frac{\Delta \alpha_z}{M_z}\right]_3 \tag{5.124}$$

$$\frac{\partial \Delta \alpha^3_{o'}}{\partial F_{o'y}} = 0 \tag{5.125}$$

$$\frac{\partial \Delta \alpha^3_{o'}}{\partial M_{o'z}} = \left[\frac{\Delta \alpha_z}{M_z}\right]_3 \tag{5.126}$$

Derivation of $\partial \Delta y^3_{o'}/\partial F_{o'x}$, $\partial \Delta y^3_{o'}/\partial F_{o'y}$ ***and*** $\partial \Delta y^3_{o'}/\partial M_{o'z}$

$$\begin{aligned} \frac{\partial \Delta y^3_{o'}}{\partial F_{o'x}} &= \frac{\partial \Delta y^3_3}{\partial F_{o'x}} + \frac{\partial \Delta \alpha^3_{o'}}{\partial F_{o'x}} l_3 \\ &= -\left[\frac{\Delta y}{F_y}\right]_3 - l_3\left(l_3 + 2R_3\right)\left[\frac{\Delta \alpha_z}{M_z}\right]_3 \end{aligned} \tag{5.127}$$

$$\begin{aligned}\frac{\partial \Delta y^3_{o'}}{\partial F_{o'y}} &= \frac{\partial \Delta y^3_3}{\partial F_{o'y}} + \frac{\partial \Delta \alpha^3_{o'}}{\partial F_{o'y}} l_3 \\ &\quad 0 \end{aligned} \tag{5.128}$$

$$\begin{aligned}\frac{\partial \Delta y^3_{o'}}{\partial M_{o'z}} &= \frac{\partial \Delta y^3_3}{\partial M_{o'z}} + \frac{\partial \Delta \alpha^3_{o'}}{\partial M_{o'z}} l_3 \\ &= (l_3 + R_3) \left[\frac{\Delta \alpha_z}{M_z}\right]_3 \end{aligned} \tag{5.129}$$

Derivation of $\partial \Delta x^3_{o'}/\partial F_{o'x}$**,** $\partial \Delta x^3_{o'}/\partial F_{o'y}$ ***and*** $\partial \Delta x^3_{o'}/\partial M_{o'z}$

$$\frac{\partial \Delta x^3_{o'}}{\partial F_{o'x}} = 0 \tag{5.130}$$

$$\frac{\partial \Delta x^3_{o'}}{\partial F_{o'y}} = \left[\frac{\Delta x}{F_x}\right]_3 \tag{5.131}$$

$$\frac{\partial \Delta x^3_{o'}}{\partial M_{o'z}} = 0 \tag{5.132}$$

By substituting Equations 5.124-5.126, 5.127-5.129 and 5.130-5.132 into Equation 5.123, the compliance matrix of the RRR structure due to Hinge 3, $\mathbf{C_{h3}}$ can be obtained.

5.2.1.4 Compliance matrices of Links 1, 2 and 3

Since the three flexure hinges are arranged in series in the RRR structure, the overall compliances of the RRR structure at Point o' can be calculated by summing the compliance matrices, $\mathbf{C_{h1}}$, $\mathbf{C_{h2}}$ and $\mathbf{C_{h3}}$. However, the compliance matrices $\mathbf{C_{h2}}$ and $\mathbf{C_{h3}}$ are defined using the local coordinate of x^2y^2, and x^3y^3 respectively. These local coordinates are orientated 90°from the coordinate of $x^{o'}y^{o'}$. Therefore, $\mathbf{C_{h2}}$ and $\mathbf{C_{h3}}$ need to be rotated by 90° before the summation. The rotated $\mathbf{C_{h2}}$ and $\mathbf{C_{h3}}$ are referred to as $\mathbf{C'_{h2}}$ and $\mathbf{C'_{h3}}$ respectively.

$$\mathbf{C'_{h2}} = \mathbf{T_{\pi/2}} \mathbf{C_{h2}} \tag{5.133}$$

$$\mathbf{C'_{h3}} = \mathbf{T_{\pi/2}} \mathbf{C_{h3}} \tag{5.134}$$

where $T_{\pi/2}$ is obtained from Equation 5.56.

The compliance matrix at Point o' of Link 1, which is the first RRR link in the 3-RRR micro-motion structure is,

$$\mathbf{C_{L_1o',F_{o'}}} = \mathbf{C_{h1}} + \mathbf{C'_{h2}} + \mathbf{C'_{h3}} \tag{5.135}$$

where the subscript "L_1" indicates Link 1 of the 3-RRR structure.

The output displacements at Point o' of Link 1 is,

$$\begin{bmatrix} \Delta x_{o'} \\ \Delta y_{o'} \\ \Delta \alpha_{o'} \end{bmatrix}_{L_1} = \mathbf{C_{L_1o',F_{o'}}} \mathbf{F_{o'}} \tag{5.136}$$

where $\mathbf{F_{o'}} = \begin{bmatrix} F_{o'x} & F_{o'y} & M_{o'z} \end{bmatrix}^T$.

When output forces are applied at Point o instead of Point o' (see Figure 5.10a) and the displacements at this point is desired, matrix $\mathbf{T_f}$ can be used to transfer the output forces from Point o to Point o'. Once $\mathbf{C_{L_1o',F_{o'}}}$ is determined using Equation 5.135, the compliances at Point o can be calculated by transforming $\mathbf{C_{L_1o',F_{o'}}}$ to Point o using a matrix, $\mathbf{T_d}$. Intuitively, we know that $\Delta x_o = \Delta x_{o'}$ and $\Delta \alpha_o = \Delta \alpha_{o'}$. However, $\Delta y_o \neq \Delta y_{o'}$ due to rotational motions ($\Delta \alpha_{o'}$) and the amplification of lever arm, l_6. This link amplification effect is taken into consideration by the matrix $\mathbf{T_d}$. The displacement, Δy_o of the RRR stage is illustrated in Figure 5.15.

The force transformation matrix is,

$$\mathbf{T_f} = \begin{bmatrix} 1 & 0 & 0 \\ 0 & 1 & 0 \\ 0 & -l_6 & 1 \end{bmatrix} \tag{5.137}$$

where,

$$\mathbf{F_{o'}} = \mathbf{T_f} \mathbf{F_o} \tag{5.138}$$

and,

$$\mathbf{F_o} = \begin{bmatrix} F_{ox} & F_{oy} & M_{oz} \end{bmatrix}^T.$$

The displacement transformation matrix is,

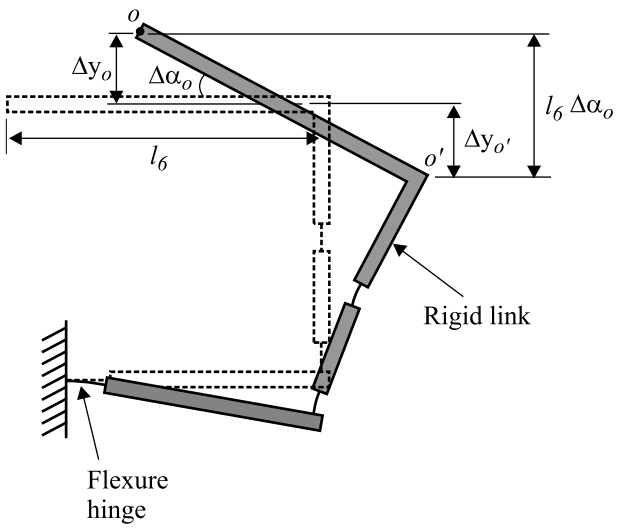

Figure 5.15: Calculation of compliances at Point o. Dashed lines represent initial position of the RRR structure. The flexure hinge is drawn as a solid line and the rigid link is drawn as a block

$$\mathbf{T_d} = \begin{bmatrix} 1 & 0 & 0 \\ 0 & 1 & -l_6 \\ 0 & 0 & 1 \end{bmatrix} \tag{5.139}$$

The output displacements at Point o of Link 1 is,

$$\begin{bmatrix} \Delta x_o \\ \Delta y_o \\ \Delta \alpha_o \end{bmatrix}_{L_1} = \mathbf{T_d C_{L_1 o', F_{o'}}} \left(\mathbf{T_f F_o}\right) \tag{5.140}$$

Therefore, the compliance of Link 1 at Point o is,

$$\mathbf{C_{L_1 o, F_o}} = \mathbf{T_d C_{L_1 o', F_{o'}} T_f} \tag{5.141}$$

Since Links 2 and 3 are arranged to be -120° and 120° apart from Link 1, the compliance of Links 2 and 3 at Point o can be obtained as shown below:

The displacements, $\mathbf{D_{L_2 o, F_o}}$ and $\mathbf{D_{L_3 o, F_o}}$ at Point o due to compliances of Links 2 and 3 respectively are,

$$\mathbf{D_{L2o,F_o}} = \mathbf{T_{-2\pi/3}} \mathbf{C_{L1o,F_o}} \mathbf{T^T_{-2\pi/3}} \mathbf{F_o} \tag{5.142}$$

$$\mathbf{D_{L3o,F_o}} = \mathbf{T_{2\pi/3}} \mathbf{C_{L1o,F_o}} \mathbf{T^T_{2\pi/3}} \mathbf{F_o} \tag{5.143}$$

where,

$$\mathbf{T_{2\pi/3}} = \begin{bmatrix} cos(2\pi/3) & -sin(2\pi/3) & 0 \\ sin(2\pi/3) & cos(2\pi/3) & 0 \\ 0 & 0 & 1 \end{bmatrix} \tag{5.144}$$

$$\mathbf{T_{-2\pi/3}} = \begin{bmatrix} cos(-2\pi/3) & -sin(-2\pi/3) & 0 \\ sin(-2\pi/3) & cos(-2\pi/3) & 0 \\ 0 & 0 & 1 \end{bmatrix} \tag{5.145}$$

and $\mathbf{T^T_{2\pi/3}}$ and $\mathbf{T^T_{-2\pi/3}}$ are the transpose of $\mathbf{T_{2\pi/3}}$ and $\mathbf{T_{-2\pi/3}}$ respectively.
Therefore from Equations 5.142 and 5.143, compliance matrices of Links 2 and 3 can be expressed as,

$$\mathbf{C_{L2o,F_o}} = \mathbf{T_{-2\pi/3}} \mathbf{C_{L1o,F_o}} \mathbf{T^T_{-2\pi/3}} \tag{5.146}$$

$$\mathbf{C_{L3o,F_o}} = \mathbf{T_{2\pi/3}} \mathbf{C_{L1o,F_o}} \mathbf{T^T_{2\pi/3}} \tag{5.147}$$

Since Links 1, 2 and 3 are arranged in parallel to each other (see Figure 5.11), the compliance matrix of the 3-RRR compliant micro-motion stage, $\mathbf{C_{o,F_o}}$ can be found using the rule of calculating the equivalent compliances for parallel connections of springs.

$$\mathbf{C_{o,F_o}} = \left(\mathbf{C^{-1}_{L1o,F_o}} + \mathbf{C^{-1}_{L2o,F_o}} + \mathbf{C^{-1}_{L3o,F_o}}\right)^{-1} \tag{5.148}$$

The output displacements of the 3-RRR compliant stage due to applied forces/moment can be expressed as,

$$\begin{bmatrix} \Delta x_o \\ \Delta y_o \\ \Delta \alpha_o \end{bmatrix}_{3RRR} = \mathbf{C_{o,F_o}} \mathbf{F_o} \tag{5.149}$$

5.2.2 Derivation of the compliance matrix, $\mathbf{C_{o,F_{in}}}$ and $\mathbf{C_{in,F_o}}$

The compliance matrix which relates the output displacements at Point o to input forces F_{1in}, F_{2in} and F_{3in} is,

$$\mathbf{C_{o,F_{in}}} = \begin{bmatrix} \mathbf{C_{o,F_{1in}}} & \mathbf{C_{o,F_{2in}}} & \mathbf{C_{o,F_{3in}}} \end{bmatrix} \tag{5.150}$$

where $\mathbf{C_{o,F_{1in}}}$, $\mathbf{C_{o,F_{2in}}}$ and $\mathbf{C_{o,F_{3in}}}$ are 3x1 matrices relating the output displacements to the input forces.

In order to find $\mathbf{C_{o,F_{1in}}}$ in Equation 5.150, the 3-RRR compliant stage is divided into three RRR links, similar to the calculation of $\mathbf{C_{o,F_o}}$. The compliance matrix ($\mathbf{C_{L_1o',F_{1in}}}$) of Link 1 at Point o' due to F_{1in} is firstly calculated. Then, the compliance matrix at Point o, $\mathbf{C_{L_1o,F_{1in}}}$ is calculated by multiplying the transformation matrix, $\mathbf{T_d}$ to $\mathbf{C_{L_1o',F_{1in}}}$.

5.2.2.1 Derivation of $\mathbf{C_{L_1o',F_{1in}}}$ and $\mathbf{C_{L_1o,F_{1in}}}$

When input force F_{1in} is applied, compliances of the RRR Link 1 at Point o' and Point o are only affected by the compliances of Hinge 1 due to its open-chain configuration. The compliance matrix at Point o', $\mathbf{C_{L_1o',F_{1in}}}$ due to Hinge 1 is expressed as,

$$\mathbf{C_{L_1o',F_{1in}}} = \begin{bmatrix} \partial\Delta x^1_{o'}/\partial F_{1in} \\ \partial\Delta y^1_{o'}/\partial F_{1in} \\ \partial\Delta \alpha^1_{o'}/\partial F_{1in} \end{bmatrix} \tag{5.151}$$

where the partial derivative terms in Equation 5.151 are derived as follows:
From Equations 5.90 , 5.97 and 5.105, $\Delta\alpha^1_1$-, Δy^1_1- and Δx^1_1-displacements are,

$$\Delta\alpha^1_1 = \left[\frac{\Delta\alpha_z}{M_z}\right]_1 \{-F_{o'x}l_4 + F_{o'y}(l_1 + R_1) + M_{o'z} - F_{1in}(l_5 + R_1)\}$$

$$\Delta y^1_1 = \left[\frac{\Delta y}{F_y}\right]_1 (F_{o'y} - F_{1in}) + \left[\frac{\Delta\alpha_z}{M_z}\right]_1 (-F_{o'x}l_4 + F_{o'y}l_1 + M_{o'z} - F_{1in}l_5) R_1$$

$$\Delta x^1_1 = \left[\frac{\Delta x}{F_x}\right]_1 F_{o'x}$$

The $\Delta\alpha^1_1$-, Δy^1_1- and Δx^1_1-compliances of Hinge 1 caused by F_{1in} are obtained by taking the partial derivatives of $\Delta\alpha^1_1$, Δy^1_1 and Δx^1_1 with respect to the input force

F_{1in} acting at Point 1_{in} (see Figure 5.12),

$$\frac{\partial \Delta\alpha_1^1}{\partial F_{1in}} = -(l_5 + R_1)\left[\frac{\Delta\alpha_z}{M_z}\right]_1 \tag{5.152}$$

$$\frac{\partial \Delta y_1^1}{\partial F_{1in}} = -\left[\frac{\Delta y}{F_y}\right]_1 - (l_5 R_1)\left[\frac{\Delta\alpha_z}{M_z}\right]_1 \tag{5.153}$$

$$\frac{\partial \Delta x_1^1}{\partial F_{1in}} = 0 \tag{5.154}$$

The $\Delta\alpha_{o'}^1$-displacement is the same as $\Delta\alpha_1^1$-displacement. Therefore, the results of the partial derivatives with respect to F_{1in} are the same as Equation 5.152.

$$\frac{\partial \Delta\alpha_{o'}^1}{\partial F_{1in}} = -(l_5 + R_1)\left[\frac{\Delta\alpha_z}{M_z}\right]_1 \tag{5.155}$$

From Equations 5.101 and 5.109, the $\Delta y_{o'}^1$- and $\Delta x_{o'}^1$-displacements are,

$$\Delta y_{o'}^1 = \Delta y_1^1 + \Delta\alpha_{o'}^1 l_1$$

$$\Delta x_{o'}^1 = \Delta x_1^1 - \Delta\alpha_{o'}^1 l_4$$

The $\Delta y_{o'}^1$- and $\Delta x_{o'}^1$-compliances of Hinge 1 caused by F_{1in} are obtained by taking the partial derivatives of $\Delta y_{o'}^1$ and $\Delta x_{o'}^1$ with respect to the input force, F_{1in} acting at Point 1_{in},

$$\begin{aligned}
\frac{\partial \Delta y_{o'}^1}{\partial F_{1in}} &= \frac{\partial \Delta y_1^1}{\partial F_{1in}} + \frac{\partial \Delta\alpha_{o'}^1}{\partial F_{1in}} l_1 \\
&= \left\{-\left[\frac{\Delta y}{F_y}\right]_1 - (l_5 R_1)\left[\frac{\Delta\alpha_z}{M_z}\right]_1\right\} + \left\{-(l_5 + R_1)\left[\frac{\Delta\alpha_z}{M_z}\right]_1 l_1\right\} \\
&= -\left[\frac{\Delta y}{F_y}\right]_1 - \left\{(l_5 R_1 + l_1(l_5 + R_1))\left[\frac{\Delta\alpha_z}{M_z}\right]_1\right\}
\end{aligned} \tag{5.156}$$

$$\begin{aligned}\frac{\partial \Delta x^1_{o'}}{\partial F_{1in}} &= \frac{\partial \Delta x^1_1}{\partial F_{1in}} - \frac{\partial \Delta \alpha^1_{o'}}{\partial F_{1in}} l_4 \\ &= -\left\{ -\left(l_5 + R_1\right) \left[\frac{\Delta \alpha_z}{M_z}\right]_1 l_4 \right\} \\ &= l_4 \left(l_5 + R_1\right) \left[\frac{\Delta \alpha_z}{M_z}\right]_1 \end{aligned} \tag{5.157}$$

By substituting Equations 5.155, 5.156 and 5.157 into Equation 5.151, $\mathbf{C_{L1o',F1in}}$ can be found.
The compliance matrix at Point o, $\mathbf{C_{L1o,F1in}}$is,

$$\mathbf{C_{L1o,F1in}} = \mathbf{T_d C_{L1o',F1in}} \tag{5.158}$$

5.2.2.2 Derivation of $\mathbf{C_{o,F1in}}$, $\mathbf{C_{o,F2in}}$ and $\mathbf{C_{o,F3in}}$

The output displacement of Link 1, $\mathbf{D_{L1o,F1in}}$ at Point o due to input force F_{1in} is,

$$\mathbf{D_{L1o,F1in}} = \mathbf{C_{L1o,F1in}} F_{1in} \tag{5.159}$$

By using Equation 5.141, the output displacement of Link 1, $\mathbf{D_{L1o,Fo}}$ at Point o due to output force $\mathbf{F_o}$ is,

$$\mathbf{D_{L1o,Fo}} = \mathbf{C_{L1o,Fo} F_o} \tag{5.160}$$

By equating Equations 5.159 and 5.160, the equivalent output force $\mathbf{F_{L1o,eqv}}$ at Point o when $F_{1in} = 1$N (unit force) can be calculated as below, where $\mathbf{F_{L1o,eqv}} = \mathbf{F_o}$ in Equation 5.160,

$$\mathbf{F_{L1o,eqv}} = \left[\mathbf{C_{L1o,Fo}}\right]^{-1} \mathbf{C_{L1o,F1in}} \tag{5.161}$$

By multiplying the equivalent output force $\mathbf{F_{L1o,eqv}}$ to $\mathbf{C_{o,Fo}}$, the output displacement of the 3-RRR compliant stage caused by F_{1in} from Link 1 can be found. Since a unit force of F_{1in} is used to calculate the equivalent output force, the output displacement obtained can also represent the output compliance of the stage caused by F_{1in}:

$$\mathbf{C_{o,F1in}} = \mathbf{D_{o,F1in}} = \mathbf{C_{o,Fo} F_{L1o,eqv}} \tag{5.162}$$

Since Links 2 and 3 are orientated by -120° and 120° from Link 1, $\mathbf{C_{o,F2in}}$ and $\mathbf{C_{o,F3in}}$ can be found as shown below,

$$\mathbf{C_{o,F_{2in}}} = \mathbf{T_{-2\pi/3}} \mathbf{C_{o,F_{1in}}} \tag{5.163}$$

$$\mathbf{C_{o,F_{3in}}} = \mathbf{T_{2\pi/3}} \mathbf{C_{o,F_{1in}}} \tag{5.164}$$

By substituting Equations 5.162, 5.163 and 5.164 into Equation 5.150, the compliance matrix $\mathbf{C_{o,F_{in}}}$ of the 3-RRR stage can be obtained.

And $\mathbf{C_{in,F_o}}$ is the transpose of $\mathbf{C_{o,F_{in}}}$ and can be obtained as below,

$$\mathbf{C_{in,F_o}} = [\mathbf{C_{o,F_{in}}}]^T \tag{5.165}$$

5.2.3 Derivation of the compliance matrix, $\mathbf{C_{in,F_{in}}}$

The compliance matrix which relates the input displacements at Points 1_{in}, 2_{in} and 3_{in} to input forces F_{1in}, F_{2in} and F_{3in} is,

$$\mathbf{C_{in,F_{in}}} = \begin{bmatrix} \mathbf{C_{in,F_{1in}}} & \mathbf{C_{in,F_{2in}}} & \mathbf{C_{in,F_{3in}}} \end{bmatrix} \tag{5.166}$$

where $\mathbf{C_{in,F_{in}}}$ is a 3x3 matrix, $\mathbf{C_{in,F_{1in}}}$, $\mathbf{C_{in,F_{2in}}}$ and $\mathbf{C_{in,F_{3in}}}$ are 3x1 matrices.

The input displacements, $\mathbf{D_{in,F_{1in}}}$ due to input force F_{1in} can be calculated as below, where $\mathbf{C_{in,F_o}}$ is obtained from Equation 5.165 and $\mathbf{F_{L_1o,eqv}}$ is obtained from Equation 5.161. Note that $\mathbf{F_{L_1o,eqv}}$ is the equivalent force calculated at Point o when input force F_{1in} is applied at Link 1. Since a unit force of F_{1in} is used to obtain the equivalent output force, the input displacements $\mathbf{D_{in,F_{1in}}}$ obtained can also represents the input compliances of the stage caused by F_{1in}:

$$\begin{aligned} \mathbf{C_{in,F_{1in}}} &= \mathbf{D_{in,F_{1in}}} \\ &= \begin{bmatrix} u_{1in,F_{1in}} \\ u_{2in,F_{1in}} \\ u_{3in,F_{1in}} \end{bmatrix} = \mathbf{C_{in,F_o}} \mathbf{F_{L_1o,eqv}} \end{aligned} \tag{5.167}$$

where $u_{1in,F_{1in}}$, $u_{2in,F_{1in}}$ and $u_{3in,F_{1in}}$ are displacements at Points 1_{in}, 2_{in} and 3_{in} (see Figure 5.10) of the 3-RRR stage due to F_{1in}.

Similarly for Links 2 and 3,

$$\begin{aligned}\mathbf{C_{in,F_{2in}}} &= \mathbf{D_{in,F_{2in}}} \\ &= \begin{bmatrix} u_{1in,F_{2in}} \\ u_{2in,F_{2in}} \\ u_{3in,F_{2in}} \end{bmatrix} = \mathbf{C_{in,F_o}F_{L_2o,eqv}}\end{aligned} \tag{5.168}$$

$$\mathbf{F_{L_2o,eqv}} = \mathbf{T_{-2\pi/3}F_{L_1o,eqv}}$$

where $u_{1in,F_{2in}}$, $u_{2in,F_{2in}}$ and $u_{3in,F_{2in}}$ are displacements at the three input points of the 3-RRR stage due to F_{2in},

$$\begin{aligned}\mathbf{C_{in,F_{3in}}} &= \mathbf{D_{in,F_{3in}}} \\ &= \begin{bmatrix} u_{1in,F_{3in}} \\ u_{2in,F_{3in}} \\ u_{3in,F_{3in}} \end{bmatrix} = \mathbf{C_{in,F_o}F_{3o,eqv}}\end{aligned} \tag{5.169}$$

$$\mathbf{F_{L_3o,eqv}} = \mathbf{T_{2\pi/3}F_{L_1o,eqv}}$$

where $u_{1in,F_{3in}}$, $u_{2in,F_{3in}}$ and $u_{3in,F_{3in}}$ are displacements at the three input points of the 3-RRR stage due to F_{3in}.
By substituting Equations 5.167, 5.168 and 5.169 into Equation 5.166, compliance matrix $\mathbf{C_{in,F_{in}}}$ can be obtained.

5.2.4 The Jacobian matrix of 3-RRR micro-motion stages

The relationship between the input and output displacements can be derived from Equation 5.87 for a given $\mathbf{F_o}$. For example, when there is no external force, $\mathbf{F_o} = \mathbf{0}$, and therefore,

$$\mathbf{U_o} = \mathbf{C_{o,F_{in}}F_{in}} \tag{5.170}$$

$$\mathbf{F_{in}} = \mathbf{C^{-1}_{o,F_{in}}U_o} \tag{5.171}$$

and,

$$\mathbf{U_{in}} = \mathbf{C_{in,F_{in}}}\mathbf{F_{in}} \tag{5.172}$$

$$\mathbf{F_{in}} = \mathbf{C^{-1}_{in,F_{in}}}\mathbf{U_{in}} \tag{5.173}$$

By equating Equation 5.171 and Equation 5.173 ,

$$\mathbf{U_o} = \mathbf{C_{o,F_{in}}}\mathbf{C^{-1}_{in,F_{in}}}\mathbf{U_{in}} \tag{5.174}$$

A constant Jacobian matrix is used in this thesis (as explained in Section 4.2) to relate the output displacements ($\mathbf{U_o}$) to the input displacements ($\mathbf{U_{in}}$) of the compliant mechanisms; therefore the Jacobian matrix is defined as below,

$$\mathbf{J} = \mathbf{C_{o,F_{in}}}\mathbf{C^{-1}_{in,F_{in}}} \tag{5.175}$$

5.2.5 Case studies of the 3-RRR compliant micro-motion stage

For comparison purposes, the 3-RRR compliant micro-motion stage studied in this section is the same as that in Chapter 4. Material properties, link lengths and flexure hinge dimensions of the mechanism are shown in Table 5.5.

Two cases were studied where analytical matrices of the kinetostatic models of Case 1 were calculated by deliberately choosing the flexure hinge equations with large differences when compared to FEA results (refer to Figures 3.12-3.14). Meanwhile, analytical matrices of Case 2 were obtained by choosing the flexure hinge equations with small differences (refer to Figures 3.12-3.14 and Table 3.9). Table 5.6 shows the flexure hinge equations chosen from various published research studies for Cases 1 and 2 respectively. Table 5.7 shows the analytical results of Cases 1 and 2 respectively.

5.2.5.1 Discussion

It can be observed in Table 5.7 that the off-diagonal terms of the compliance matrix, $\mathbf{C_{o,F_o}}$ are zero. This is expected as the 3-RRR compliant stage has a Remote-Centre-of-Compliance (RCC) configuration and deformations occur only along the direction of the applied force/moment (Kim *et al.*, 2000). The 3-RRR stage was designed to have a somewhat decoupled characteristic where the input displacements of one link have small effects on the input displacements of the other links.

This characteristic can be observed in $\mathbf{C_{in,F_{in}}}$. The off-diagonal terms of $\mathbf{C_{in,F_{in}}}$ are approximately a factor of 8 smaller than its diagonal terms. It can also be observed that the analytical results of Cases 1 and 2 are noticeably different except for the Jacobian matrix. This is because the Jacobian matrix represents the kinematics of the micro-motion structures; therefore it is almost independent of the compliances or stiffnesses of flexure hinges. The choice of flexure hinge equations used to calculate the analytical results has minimal effects on the results of the Jacobian matrix.

The differences of results of Cases 1 and 2 suggest that the choice of flexure hinge compliance equations affects the results of the kinetostatic model. Since the kinetostatic model is derived to have flexure hinge compliances as one of the variables, flexure hinge equations with small errors can be selected based on the scheme developed in Chapter 3 in order to obtain an accurate kinetostatic model. The modelling results of Cases 1 and 2 will be compared to the FEA and experimental results in Chapters 6 and 7 respectively in order to verify their accuracies.

Material properties	
E	71.7 GPa
Poisson's ratio, v	0.33

Link length	l_1	l_2	l_3	l_4	l_5	l_6
(mm)	47.9	22.17	0	30	4	12

Flexure hinge	t_1	t_2	t_3	R_1	R_2	R_3	t_1/R_1	t_2/R_2	t_3/R_3	b
(mm)	0.84	0.7	0.5	1.1	1.87	3	0.764	0.374	0.167	12.7

Table 5.5: Material properties, link lengths and flexure hinge dimensions of the 3-RRR compliant micro-motion stage

Case 1	t/R	$\Delta\alpha_z/M_z$	$\Delta y/F_y$	$\Delta x/F_x$
Flexure hinge 1	0.764	Paros and Weisbord (1965) (Full)/ Lobontiu (2003)/ Wu and Zhou (2002)	Schotborgh *et al.* (2005)	Schotborgh *et al.* (2005)
Flexure hinge 2	0.374	Paros and Weisbord (1965) (Full)/ Lobontiu (2003)/ Wu and Zhou (2002)	Schotborgh *et al.* (2005)	Schotborgh *et al.* (2005)
Flexure hinge 3	0.167	Paros and Weisbord (1965) (Full)/ Lobontiu (2003)/ Wu and Zhou (2002)	Schotborgh *et al.* (2005)	Schotborgh *et al.* (2005)

Case 2	t/R	$\Delta\alpha_z/M_z$	$\Delta y/F_y$	$\Delta x/F_x$
Flexure hinge 1	0.764	Schotborgh *et al.* (2005)	This thesis (Equation 3.19)	This thesis (Equation 3.17)
Flexure hinge 2	0.374	Schotborgh *et al.* (2005)	This thesis (Equation 3.19)	This thesis (Equation 3.17)
Flexure hinge 3	0.167	Schotborgh *et al.* (2005)	This thesis (Equation 3.19)	This thesis (Equation 3.17)

Table 5.6: Flexure hinge equations chosen for Cases 1 and 2 for the derivation of kinetostatics of the 3-RRR micro-motion stage

Case 1	Analytical results
$\mathbf{C_{o,F_o}}$ ($\mu m/N$, $\mu rad/N$ $\mu m/Nm$, $\mu rad/Nm$)	$\begin{matrix} 10.104 & 0 & 0 \\ 0 & 10.104 & 0 \\ 0 & 0 & 23960 \end{matrix}$
$\mathbf{C_{o,F_{in}}}$ ($\mu m/N$, $\mu rad/N$)	$\begin{matrix} 0.775 & 0.222 & -0.998 \\ 0.705 & -1.024 & 0.319 \\ -29.789 & -29.789 & -29.789 \end{matrix}$
$\mathbf{C_{in,F_{in}}}$ ($\mu m/N$)	$\begin{matrix} 0.146 & -0.017 & -0.017 \\ -0.017 & 0.146 & -0.017 \\ -0.017 & -0.017 & 0.146 \end{matrix}$
$\mathbf{J_{analytical}}$	$\begin{matrix} 4.758 & 1.367 & -6.125 \\ 4.326 & -6.284 & 1.958 \\ -268.114 & -268.114 & -268.114 \end{matrix}$

Case 2	Analytical results
$\mathbf{C_{o,F_o}}$ ($\mu m/N$, $\mu rad/N$ $\mu m/Nm$, $\mu rad/Nm$)	$\begin{matrix} 12.250 & 0 & 0 \\ 0 & 12.250 & 0 \\ 0 & 0 & 27402 \end{matrix}$
$\mathbf{C_{o,F_{in}}}$ ($\mu m/N$, $\mu rad/N$)	$\begin{matrix} 0.948 & 0.267 & -1.215 \\ 0.856 & -1.249 & 0.393 \\ -34.297 & -34.297 & -34.297 \end{matrix}$
$\mathbf{C_{in,F_{in}}}$ ($\mu m/N$)	$\begin{matrix} 0.176 & -0.024 & -0.024 \\ -0.024 & 0.176 & -0.024 \\ -0.024 & -0.024 & 0.176 \end{matrix}$
$\mathbf{J_{analytical}}$	$\begin{matrix} 4.746 & 1.338 & -6.083 \\ 4.284 & -6.252 & 1.968 \\ -266.328 & -266.328 & -266.328 \end{matrix}$

Table 5.7: Case studies - Analytical matrices of the kinetostatic model of the 3-RRR micro-motion stage

5.3 Concluding remarks

The kinetostatic results (both compliance and Jacobian matrices) of the four-bar and the 3-RRR compliant micro-motion stages for Cases 1 and 2 are noticeably different except for some of the terms in the Jacobian matrices. The Jacobian matrix represents the kinematics of the micro-motion structures; therefore the accuracies of flexure hinge compliance equations are expected to have minimal effects on the results of the Jacobian matrix.

The differences between the compliance results of Cases 1 and 2 a) show the influences of the choice of flexure hinge compliance equations on the accuracy of the kinetostatic models, and also b) highlight the advantage of the closed-form kinetostatic model (with flexure hinge compliance equations as one of the variables in the equations) where the most suitable flexure hinge equations can be used to calculate the kinetostatics of compliant mechanisms accurately. The kinetostatic results of Cases 1 and 2 will be compared to the FEA and experimental results in Chapters 6 and 7 respectively in order to verify their accuracies.

CHAPTER 6

Finite Element Analysis

In Chapter 4, the kinematics of the four-bar and the 3-RRR compliant micro-motion stages were modelled using the PRBM method and the loop-closure theory. In Chapter 5, the kinetostatics of the two micro-motion stages were derived. In order to verify the accuracies of the kinematic and the kinetostatic models, two-dimensional finite-element-analysis (FEA) models of these compliant stages were generated using ANSYS for comparison purposes. This chapter presents the FEA modelling techniques for both the four-bar compliant mechanism and the 3-RRR compliant micro-motion stage using ANSYS. The results of the comparison between the Jacobian matrix obtained using the PRBM method and the FEA model are presented. The results of the comparison between the compliance and Jocobian matrices obtained using the kinetostatic model and the FEA model are also presented.

6.1 FEA modelling of micro-motion stages

FEA models of the micro-motion stages were generated using ANSYS. Similar to the FEA modelling technique in Chapter 3, the micro-motion stages were generated using 8-node, two-dimensional, plane elements (PLANE82) with two-DOF on each node. The DOF are the translations in the nodal x and y directions. Thicknesses of the models were taken into account by using the plane stress element type with thickness option. To ensure that the mesh size was fine enough especially near the flexure hinge locations, a number of analyses were carried out where different mesh sizes were used. The output was checked each time the

mesh size was decreased. When a consistent output was obtained, it implied that the mesh was fine enough. When nodal displacements were measured from the same node which forces are applied, pressures were applied on a line instead to avoid inaccuracy of results associated with singularities on the nodes.

6.1.1 FEA modelling of the four-bar micro-motion stage

Meshes and constraints of the FEA model of the four-bar compliant stage are shown in Figure 6.1. The following procedures were carried out to obtain the compliance and Jacobian matrices of the stage:

1. To obtain the compliant matrix $\mathbf{C_{o,F_o}}$ of the stage, a point force F^*_{ox} was applied at a distance from Point o but along the same line of action as force F_{ox} (see Figure 6.1). Pressure P_{oy}, which is equivalent to a unit point force F_{oy}, was applied on a line as shown in Figure 6.1. The corresponding nodal deformations (Δx_o, Δy_o , $\Delta \alpha_o$) at Point o were measured after these forces/ pressures were applied. In order to obtain the compliances corresponding to a unit moment, two equal but opposite forces, F_m were applied as shown. Rotational deformations ($\Delta \alpha_o$) can not be measured directly from the node at Point o because the nodes of PLANE82 elements do not have a rotational DOF. However, $\Delta \alpha_o$ can be easily calculated using the similar method as presented in Chapter 3.

2. To obtain the compliance matrix $\mathbf{C_{o,F_{in}}}$ of the stage, pressure P_{in}, which is equivalent to a unit input force, was applied on the line where Point 1_{in} was located as shown in Figure 6.3, and the corresponding nodal deformations (Δx_o, Δy_o , $\Delta \alpha_o$) at Point o were measured.

3. To obtain the compliance matrix $\mathbf{C_{in,F_o}}$ of the stage, unit point forces were applied at Point o and the corresponding nodal deformation (U_{in}) at Point 1_{in} was measured. Moment was applied using two equal but opposite forces, F_m.

4. To obtain the compliance matrix $C_{in,F_{in}}$ of the stage, pressure P_{in}, which is equivalent to a unit input force F_{in}, was applied on the line where Point 1_{in} was located, and the corresponding nodal deformations at this point was measured.

5. To obtain the Jacobian matrix, a pressure P_{in} was applied on the line where Point 1_{in} was located. The corresponding input displacement (U_{in}) at Point 1_{in} and the output displacements (Δx_o, Δy_o , $\Delta \alpha_o$) at Point o were measured.

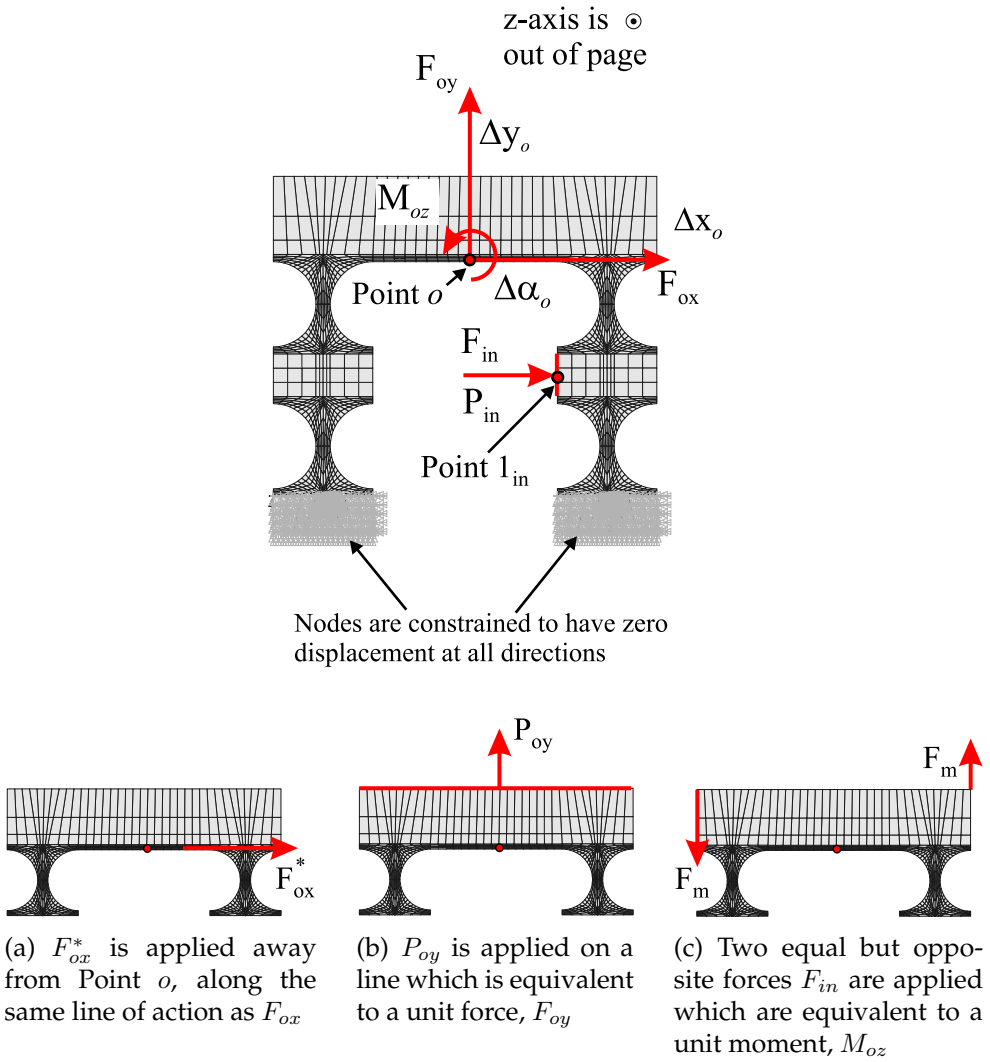

(a) F^*_{ox} is applied away from Point o, along the same line of action as F_{ox}

(b) P_{oy} is applied on a line which is equivalent to a unit force, F_{oy}

(c) Two equal but opposite forces F_{in} are applied which are equivalent to a unit moment, M_{oz}

Figure 6.1: The FEA model of the four-bar compliant micro-motion stage

The Jacobian matrix was obtained where the output displacements were divided by the input displacement,

$$\mathbf{J_{FEA,4bar}} = \begin{bmatrix} \Delta x_o/U_{in} \\ \Delta y_o/U_{in} \\ \Delta \alpha_o/U_{in} \end{bmatrix}$$

Figure 6.2 shows the deformation results of the four-bar compliant mechanism. The FEA results show relatively insignificant link deformations for the loading case along the x-direction. The degree-of-freedom of the four-bar compliant structure was along the x-direction; therefore the four-bar structure was expected to have lower structural stiffness along this direction compared to that along the y- and about the z-directions. The four-bar compliant mechanism was considered

	FEA results		
$\mathbf{C_{o,F_o}}$ ($\mu m/N$, $\mu rad/N$ $\mu m/Nm$, $\mu rad/Nm$)	1.904	0	0.904
	0	4.909	0
	−0.911	0	112.9
$\mathbf{C_{o,F_{in}}}$ ($\mu m/N$, $\mu rad/N$)	0.961		
	0		
	−0.252		
$C_{in,F_{in}}$ ($\mu m/N$)	0.459		
$\mathbf{J_{FEA}}$	2.07		
	0		
	−0.62		

Table 6.1: FEA compliance and Jacobian matrices of the four-bar compliant mechanism (with rigid-link deformations)

as a non over-constrained structure for the loading case along the x-direction and most of the deformations occurred at flexure hinges instead of links.

It was observed in Figure 6.2b that the FEA predicted significant deformations of the link for the loading case along the y-direction. The four-bar compliant structure was considered as an over-constrained structure for this loading case because the structural stiffness along the y-direction was large and significant link deformations were observed.

Some local deformations of the FEA mesh were observed when moments were applied (Figure 6.2c). Nodal deformations at the nodes where F_m was applied were not used for the calculation of the rotational deformations, $\Delta\alpha_o$ in order to avoid modelling inaccuracies due to the local deformations. Nodal deformations of nodes as shown in Figure 6.2c were measured and these nodal deformations were used instead to calculate the rotational deformations of the four-bar compliant mechanism.

Table 6.1 shows the FEA results of the four-bar compliant mechanism.

6.1.1.1 Comparison of analytical results with ANSYS

The Jacobian matrix obtained using the PRBM method in Chapter 4, the analytical compliance and Jacobian matrices of Cases 1 and 2 obtained in Chapter 5 were

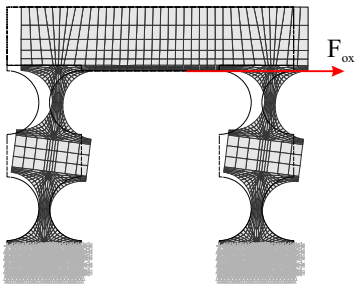

(a) Loading along the x-direction

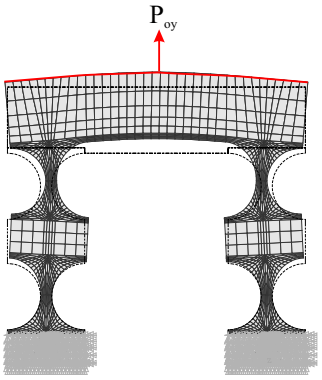

(b) Loading along the y-direction

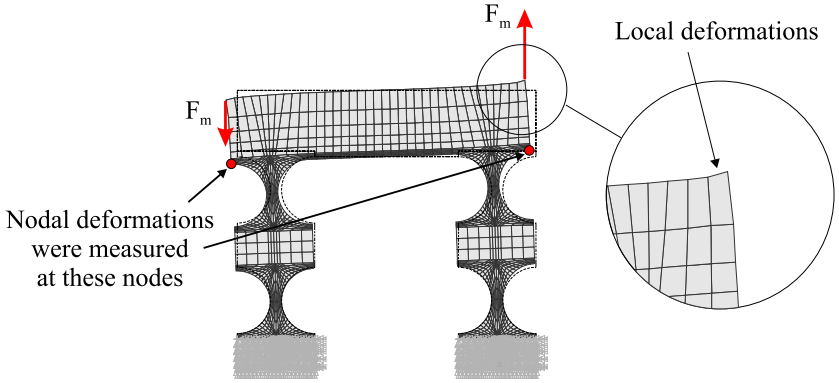

(c) Loading about the z-direction

Figure 6.2: ANSYS results of structural deformations of the four-bar compliant mechanism

compared to the ANSYS results. Table 6.2 shows the differences of the kinetostatic results of Cases 1 and 2, and the Jacobian results derived using the PRBM method when compared to the FEA results.

	Kinetostatic model - Case 1		Kinetostatic model - Case 2	
	Analytical results	% diff. compared to FEA	Analytical results	% diff. compared to FEA
$\mathbf{C_{o,F_o}}$ ($\mu m/N$, $\mu rad/N$ $\mu m/Nm$, $\mu rad/Nm$)	$\begin{matrix} 1.14 & 0 & -1.18 \\ 0 & 0.015 & 0 \\ -1.18 & 0 & 147.04 \end{matrix}$	$\begin{matrix} -40.1 & -- & 30.1 \\ -- & -99.7 & -- \\ 29.1 & -- & 30.2 \end{matrix}$	$\begin{matrix} 1.92 & 0 & -0.81 \\ 0 & 0.01 & 0 \\ -0.81 & 0 & 100.62 \end{matrix}$	$\begin{matrix} 1.0 & -- & -11.0 \\ -- & -99.7 & -- \\ 12.0 & -- & -11.0 \end{matrix}$
$\mathbf{C_{o,F_{in}}}$ ($\mu m/N$, $\mu rad/N$)	$0.57 \quad 0 \quad -0.37$	$-40.2 \quad -- \quad 30.1$	$0.96 \quad 0 \quad -0.25$	$1.1 \quad -- \quad -11$
$C_{in,F_{in}}$ ($\mu m/N$)	0.28	-38.3	0.48	4.5

	Analytical results	Differences compared to FEA ($\mu m/\mu m$, $\mu rad/\mu m$)
$\mathbf{J_{kineto,Case1}}$	$\begin{matrix} 2.001 \\ 0 \\ -1.27 \end{matrix}$	$\begin{matrix} -0.067 \\ 0 \\ -0.65 \end{matrix}$
$\mathbf{J_{kineto,Case2}}$	$\begin{matrix} 2.002 \\ 0 \\ -0.52 \end{matrix}$	$\begin{matrix} -0.068 \\ 0 \\ 0.10 \end{matrix}$
$\mathbf{J_{PRBM}}$	$\begin{matrix} 2.857 \\ 0 \\ 0 \end{matrix}$	$\begin{matrix} 0.787 \\ 0 \\ 0.62 \end{matrix}$

Table 6.2: Analytical results of the four-bar compliant mechanism and their differences compared to FEA results

6.1.1.2 Discussion

From Table 6.2, it is observed that the differences of the compliance terms (along the y-direction) in $\mathbf{C_{o,F_o}}$ for both Cases 1 and 2 are large (99.7% different) when compared to the FEA results. This is because the kinetostatic model derived in this thesis assumes that no deformations occur at rigid-links. However, rigid-link deformations are observed from the ANSYS results for the loading case along the y-direction of the four-bar compliant mechanism (see Figure 6.2b). The differences between the FEA and analytical compliances along the y-direction are attributed to the unmodelled rigid-link deformations in the kinetostatic model. To support the above statement, an investigation was carried out where rigid-links were modelled to have high stiffness in the ANSYS model by increasing the Young's modulus of the material. Pressures were once applied as shown in Figure 6.1b and the corresponding nodal deformations, Δy_o at Point o were measured. The new calculated FEA compliance along the y-direction is 0.011 $\mu m/N$. Table 6.3 shows the results of the comparison between the FEA determined compliance (obtained by modelling links to have high stiffnesses) and the analytical compliances of Cases 1 and 2. It is observed from Table 6.3 that the differences of the compliance along the y-direction are reduced from 99.7% (see Table 6.2) to 30.3% (see Table 6.3) for Case 1, and from 99.7% (see Table 6.2) to 11% (see Table 6.3) for Case 2. The results of Case 2 are closer to the FEA results compared to that of Case 1 because the flexure hinge compliance equations used to calculate the kinetostatic results of Case 2 are closer to the FEA results than that of Case 1. Results in Table 6.3 show that the derived kinetostatic results (Case 2) are in close agreement to the FEA results when the deformations of rigid-links of compliant mechanisms are insignificant.

By observing the kinetostatic results of Cases 1 and 2 in Table 6.2 (for the results of $\mathbf{C_{o,F_{in}}}$ and $C_{in,F_{in}}$) and Table 6.3 (for the results of $\mathbf{C_{o,F_o}}$) of the four-bar compliant micro-motion stage, it can be noted that the differences of compliance matrices, $\mathbf{C_{o,F_o}}$, $\mathbf{C_{o,F_{in}}}$ and $C_{in,F_{in}}$ are significantly reduced for Case 2. The average absolute difference of $\mathbf{C_{o,F_o}}$is reduced from 32% to 9.2%. The average absolute difference of $\mathbf{C_{o,F_{in}}}$ is reduced from 35.2% to 6.1%. The difference of $\mathbf{C_{in,F_{in}}}$ is reduced from 38.3% to 4.5%. These results show that the flexure hinge compliance equations affect the results of the kinetostatic models. The kinetostatic results are closer to the FEA results when flexure hinge compliance equations which have small differences when compared to the FEA results (Case 2) are used compared to if hinge equations which have large differences (Case 1) are used. The results of comparisons also highlight the advantage of the derived closed-form kinetostatic model with flexure hinge compliances as one of the variables in the equation. The

	Kinetostatic model - Case 1					
	Analytical results			% diff. compared to FEA		
$\mathbf{C_{o,F_o}}$ ($\mu m/N$, $\mu rad/N$ $\mu m/Nm$, $\mu rad/Nm$)	1.14	0	−1.18	−40.1	−−	30.1
	0	0.015	0	−−	30.3	−−
	−1.18	0	147.04	29.1	−−	30.2
	Kinetostatic model - Case 2					
	Analytical results			% diff. compared to FEA		
	1.92	0	−0.81	1.0	−−	−11.0
	0	0.01	0	−−	−11.0	−−
	−0.81	0	100.62	12.0	−−	−11.0

Table 6.3: Analytical compliance results of the four-bar compliant mechanism and their differences compared to FEA results (links are modelled to have high stiffness in the FEA model)

most suitable flexure hinge equations can be chosen using the scheme developed in Chapter 3 in order to obtain an accurate kinetostatic model of compliant mechanisms.

The differences of the Δx_o term in the Jacobian matrices of Cases 1 and 2 are similar. This is because the Jacobian matrix represents the kinematics of the micro-motion structures; therefore it is almost independent to the compliances or stiffnesses of flexure hinges. The choice of flexure hinge equations used to calculate the analytical results has minimal effects on the results of the Jacobian matrix. The choice of the flexure hinge equations influence the $\Delta\alpha_o$ term in the Jacobian matrix by a very small amount, which is 0.75 $\mu rad/\mu m$ and this influence on the $\Delta\alpha_o$ term is insignificant.

The Jacobian matrix of the four-bar compliant mechanism obtained from the kinetostatic models are closer to the FEA determined Jacobian than that of the Jacobian derived using the PRBM method in this thesis (see Table 6.2). This is expected as the Jacobian obtained from the kinetostatic model considers flexure hinges to have three-DOF while the kinematics derived using the PRBM in this thesis models flexure hinges to have only one-DOF. It can be observed in Table 6.2 that the PRBM method produces larger predictions of motions compared to the FEA and the kinetostatic results. The PRBM Jacobian does not provide the prediction of the $\Delta\alpha_o$-deformation of the four-bar compliant mechanism while the kinetostatic and FEA results show small $\Delta\alpha_o$-deformations in the Jacobian matrices. This suggests that the PRBM method is not as accurate as the kinetostatic model

when the Δx- and Δy-deformations of flexure hinges are not incorporated into the PRBM model. The PRBM could possibly provide an over estimation of motions of compliant mechanisms. This is a disadvantage to researchers in design processes. The PRBM method can be extended to model flexure hinges to have multi-DOF. Pham *et al.* (2005) extended the PRBM method to include all six DOFs of flexure hinges in the kinematic model of a 3-RRR compliant mechanism. This extended modelling method is named the PRB-D method. However, there are 42 variables which require 42 equations to solve. It is possible to model flexure hinges to have only three-DOF using the PRBM method; however the method could still produce a large number of variables to be solved. Unlike the kinetostatic model derived in this thesis, the kinetostatic model is a simple closed-form model and it does not require extensive computational loads.

6.1.2 FEA modelling of the 3-RRR micro-motion stage

Meshes and constraints of the FEA model of the 3-RRR micro-motion stage are shown in Figure 6.3. The following procedures were carried out to obtain the compliance and Jacobian matrices of the stage:

1. To obtain the compliance matrix $\mathbf{C_{o,F_o}}$ of the stage, forces F^*_{ox} and F^*_{oy} were applied at a distance from Point o but along the same lines of action as F_{ox} and F_{oy} (see Figure 6.3). The corresponding nodal deformations (Δx_o, Δy_o , $\Delta \alpha_o$) at Point o were measured. In order to obtain the compliances corresponding to a unit moment, two equal but opposite forces, F_m were applied as shown. Rotational deformation ($\Delta \alpha_o$) could not be measured directly from the node at Point o because the nodes of the element type PLANE82 do not have a rotational DOF. However, $\Delta \alpha_o$ can be easily calculated using the similar method as presented in Chapter 3.

2. To obtain the compliance matrix $\mathbf{C_{o,F_{in}}}$ of the stage, pressures (P_{1in}, P_{2in}, P_{3in}) corresponding to unit input forces were applied on lines where Points 1_{in}, 2_{in} and 3_{in} were located as shown in Figure 6.3, and the corresponding nodal deformations (Δx_o, Δy_o , $\Delta \alpha_o$) at Point o were measured.

3. To obtain the compliance matrix $\mathbf{C_{in,F_o}}$ of the stage, unit input forces were applied at Point o and the corresponding nodal deformations (u_{1in}, u_{2in}, u_{3in}) at Points 1_{in}, 2_{in} and 3_{in} were measured. Moment was applied using two equal but opposite forces, F_m.

4. To obtain the compliance matrix $\mathbf{C_{in,F_{in}}}$ of the stage, pressures (P_{1in}, P_{2in}, P_{3in}) corresponding to unit input forces were applied on lines where Points

1_{in}, 2_{in} and 3_{in} were located, and the corresponding nodal deformations at these points were measured.

5. To obtain the Jacobian matrix, pressures (P_{1in}, P_{2in}, P_{3in}) were applied independently on lines where Points 1_{in}, 2_{in} and 3_{in} were located. The corresponding input displacements (u_{1in}, u_{2in}, u_{3in}) at Points 1_{in}, 2_{in} and 3_{in}, and the output displacement (Δx_o, Δy_o , $\Delta \alpha_o$) at Point o were measured. The Jacobian matrix was obtained where the output displacements were divided by the input displacements.
For example, when u_{1in} was applied at Point 1_{in},

$$\begin{bmatrix} \Delta x_o \\ \Delta y_o \\ \Delta \alpha_o \end{bmatrix} = \begin{bmatrix} J_{FEA_{11}} & J_{FEA_{12}} & J_{FEA_{13}} \\ J_{FEA_{21}} & J_{FEA_{22}} & J_{FEA_{23}} \\ J_{FEA_{31}} & J_{FEA_{32}} & J_{FEA_{33}} \end{bmatrix} \begin{bmatrix} u_{1in} \\ 0 \\ 0 \end{bmatrix} = \begin{bmatrix} J_{FEA_{11}} u_{1in} \\ J_{FEA_{21}} u_{1in} \\ J_{FEA_{31}} u_{1in} \end{bmatrix}$$

$$\begin{bmatrix} J_{FEA_{11}} \\ J_{FEA_{21}} \\ J_{FEA_{31}} \end{bmatrix} = \begin{bmatrix} \Delta x_o / u_{1in} \\ \Delta y_o / u_{1in} \\ \Delta \alpha_o / u_{1in} \end{bmatrix}$$

where $J_{FEA_{ij}}$ (i = j = 1, 2, 3) are the row and column components of the FEA determined Jacobian matrix, J_{FEA}.

Unlike the four-bar compliant mechanism, the 3-RRR compliant stage is a non over-constrained structure for all loading cases. The rigid-link deformations are insignificant and cannot be observed from the FEA results. Therefore, the results of the kinetostatic model are expected to be in close agreement to the FEA results. Table 6.4 shows the results of the compliance and Jacobian matrices of the micro-motion stage. Since $\mathbf{C_{in,F_o}}$ is the transpose of $\mathbf{C_{o,F_{in}}}$, the results of $\mathbf{C_{in,F_o}}$ are not repeated in Table 6.4.

6.1.2.1 Comparison of analytical results with FEA

The Jacobian results derived using the PRBM method in Chapter 4 and the results of kinetostatic models of Cases 1 and 2 obtained in Chapter 5 were compared to the FEA results. Table 6.5 shows the differences when compared to FEA results.

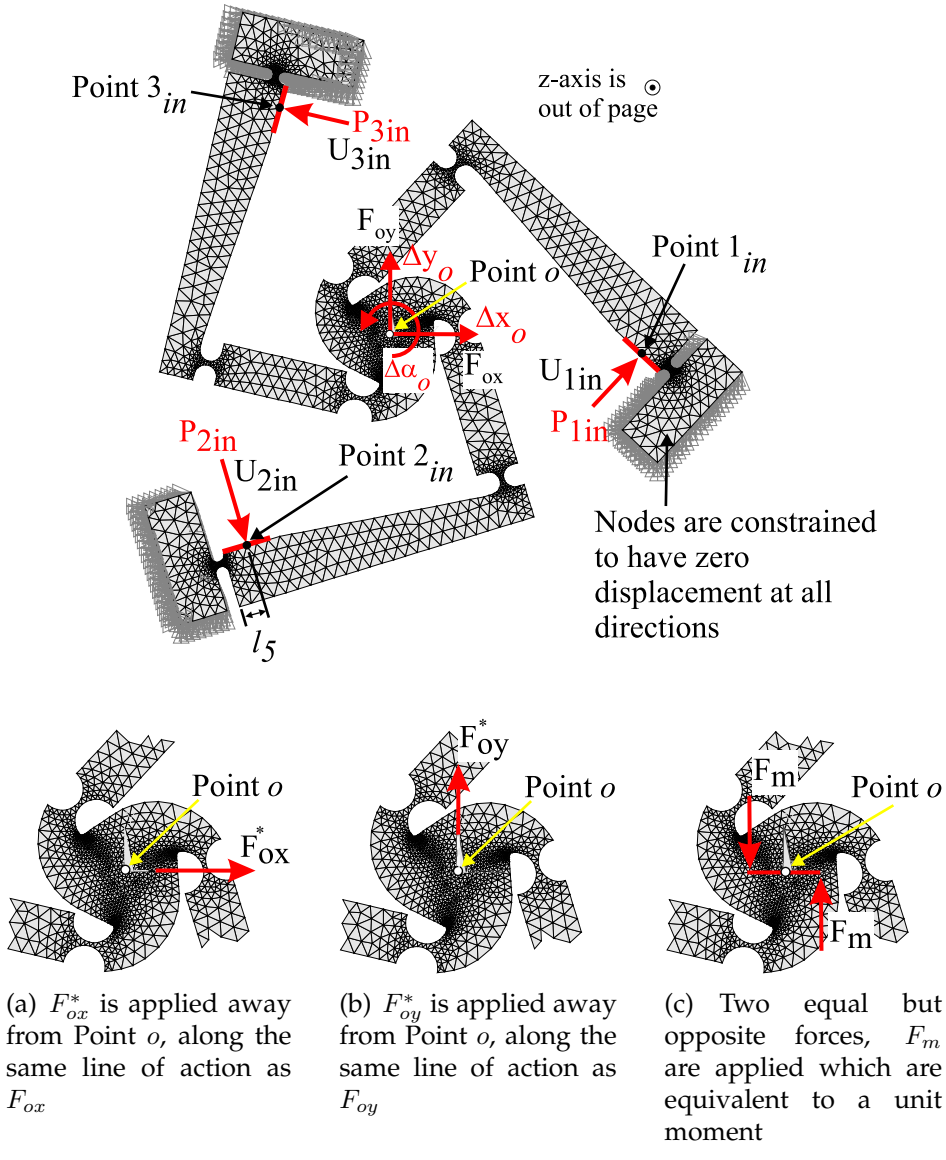

(a) F^*_{ox} is applied away from Point o, along the same line of action as F_{ox}

(b) F^*_{oy} is applied away from Point o, along the same line of action as F_{oy}

(c) Two equal but opposite forces, F_m are applied which are equivalent to a unit moment

Figure 6.3: FEA model of the 3-RRR compliant micro-motion stage

	FEA results
$\mathbf{C_{o,F_o}}$ ($\mu m/N$, $\mu rad/N$ $\mu m/Nm$, $\mu rad/Nm$)	$11.498 \quad 0 \quad 0$ $0 \quad 11.476 \quad 0$ $0 \quad 0 \quad 27966$
$\mathbf{C_{o,F_{in}}}$ ($\mu m/N$, $\mu rad/N$)	$0.879 \quad 0.257 \quad -1.136$ $0.803 \quad -1.162 \quad 0.357$ $-32.141 \quad -32.245 \quad -32.115$
$\mathbf{C_{in,F_{in}}}$ ($\mu m/N$)	$0.182 \quad -0.024 \quad -0.024$ $-0.024 \quad 0.182 \quad -0.024$ $-0.024 \quad -0.024 \quad 0.182$
$\mathbf{J_{FEA}}$	$4.259 \quad 1.250 \quad -5.499$ $3.897 \quad -5.645 \quad 1.734$ $-240.768 \quad -241.315 \quad -240.481$

Table 6.4: FEA compliance and Jacobian matrices of the 3-RRR micro-motion stage

	Kinetostatic model - Case 1						Kinetostatic model - Case 2					
	Analytical results			% diff. compared to FEA			Analytical results			% diff. compared to FEA		
$\mathbf{C_{o,F_o}}$	10.104	0	0	−12.1	−−	−−	12.250	0	0	6.5	−−	−−
($\mu m/N$, $\mu rad/N$	0	10.104	0	−−	−11.9	−−	0	12.250	0	−−	6.8	−−
$\mu m/Nm$, $\mu rad/Nm$)	0	0	23960	−−	−−	−14.3	0	0	27402	−−	−−	−2.0
$\mathbf{C_{o,F_{in}}}$	0.775	0.222	−0.998	−11.8	−13.4	−12.2	0.948	0.267	−1.215	7.8	3.9	7.0
	0.705	−1.024	0.319	−12.2	−11.9	−10.6	0.856	−1.249	0.393	6.6	7.5	10.2
($\mu m/N$, $\mu rad/N$)	−29.789	−29.789	−29.789	−7.3	−7.6	−7.2	−34.297	−34.297	−34.297	6.7	6.4	6.8
$\mathbf{C_{in,F_{in}}}$	0.146	−0.017	−0.017	−20.0	−29.3	−29.3	0.176	−0.024	−0.024	−3.2	−3.1	−3.1
	−0.017	0.146	−0.017	−29.3	−20.0	−29.3	−0.024	0.176	−0.024	−3.1	−3.2	−3.1
($\mu m/N$)	−0.017	−0.017	0.146	−29.3	−29.3	−20.0	−0.024	−0.024	0.176	−3.1	−3.1	−3.2

J ($\mu m/\mu m$, $\mu rad/\mu m$)	Analytical results			% diff. compared to FEA		
$\mathbf{J_{kineto,Case1}}$	4.758	1.367	−6.125	11.7	9.4	11.4
	4.326	−6.284	1.958	11.0	11.3	12.9
	−268.114	−268.114	−268.114	11.4	11.1	11.5
$\mathbf{J_{kineto,Case2}}$	4.746	1.338	−6.083	11.4	7.0	10.6
	4.284	−6.252	1.968	9.9	10.8	13.5
	−266.328	−266.328	−266.328	10.6	10.4	10.7
$\mathbf{J_{PRBM}}$	4.664	1.471	−6.134	9.5	17.7	11.6
	4.390	−6.235	1.844	12.7	10.5	6.3
	−288.734	−288.734	−288.734	19.9	19.7	20.1

Table 6.5: Analytical results of the 3-RRR micro-motion stage and their differences compared to FEA results

6.1.2.2 Discussion

It is noted that the differences of compliance matrices, $\mathbf{C_{o,F_o}}$, $\mathbf{C_{o,F_{in}}}$ and $\mathbf{C_{in,F_{in}}}$ are significantly reduced for Case 2. The average absolute difference of $\mathbf{C_{o,F_o}}$is reduced from 12.9% to 5%. The average absolute difference of $\mathbf{C_{o,F_{in}}}$ is reduced from 10.5% to 7%. The absolute difference of $\mathbf{C_{in,F_{in}}}$ is reduced from 24% to 3.1%. These results show that the choice of the flexure hinge compliance equations affects the results of the kinetostatic models. The kinetostatic results are closer to the FEA results when flexure hinge compliance equations which have small differences (when compared to FEA results) are used compared to that if hinge equations with large differences (Case 1) are used. The results of comparisons also highlight the advantage of the derived closed-form kinetostatic model where the accuracy of the kinetostatic model can be improved by choosing the suitable flexure hinge equations using the scheme developed in Chapter 3.

The small differences of the kinetostatic model in Case 2 are attributed to the assumption made in deriving the kinetostatic model. The kinetostatic model assumes that the deformations of rigid-links of the micro-motion stage is small and can be ignored. Although the rigid-link deformations of the 3-RRR micro-motion stage are insignificant, the small differences between the kinetostatic results and the FEA results can be attributed to these unmodelled rigid-link deformations in the kinetostatic model.

The differences of the Jacobian results are also reduced slightly but not as much as the compliance matrices. This is because the Jacobian matrix represents the kinematics of the micro-motion structures. The choice of flexure hinge equations used to calculate the analytical results has minimal effects on the results of the Jacobian matrix. Nevertheless, the overall accuracy of the analytical kinetostatic results are improved significantly, especially for the compliance matrices when the suitable flexure hinge equations are used (Case 2). This highlights the advantage of the derived closed-form kinetostatic model with flexure hinge compliances as one of the variables in the equations and the significances of the developed scheme in Chapter 3.

The Jacobian matrix obtained from the kinetostatic model is also compared to the Jacobian matrix obtained using the PRBM method. The Jacobian matrices of the 3-RRR compliant stage obtained from the kinetostatic models are more accurate than that of the Jacobian derived using the PRBM method especially for the rotational terms in the matrix (see Table 6.5). This is expected as the Jacobian results obtained from the kinetostatic model consider flexure hinges to have three-DOF while the PRBM derived in this thesis models flexure hinges to have only

one-DOF. It can be observed in Table 6.5 that the PRBM Jacobian predicts much larger $\Delta\alpha_o$-deformations compared to that of the FEA and the kinetostatic models. This suggests that the PRBM, which models flexure hinges to have only one-DOF, could possibly provides an over estimation of motions of compliant mechanisms which is a disadvantage to researchers during design phases. It is possible to extend the PRBM method to model flexure hinges to have multi-DOF as mentioned in Section 6.1.1.2. However, the extended PRBM method could produce a large number of variables to be solved, which require extensive computational effort. On the other hand, the kinetostatic model derived in this thesis is a simple closed-form model and it does not require extensive computational effort.

6.2 Concluding remarks

It was found that the kinetostatic results of Case 2 were closer to the FEA results than that of Case 1 especially for the compliance matrices. These results showed that the accuracy of the flexure hinge compliance equations had some effects on the accuracy of the kinetostatic models. The results also indicated the importance of the selection of flexure hinge compliance equations when calculating the kinetostatics of compliant micro-motion stages. The work presented in this chapter highlights a) the significances of the scheme developed in Chapter 3, and b) the advantage of the derived closed-form kinetostatic model with flexure hinge compliances as one of the variables in the equation.

For the four-bar compliant mechanism, the differences of the compliance matrices obtained from the kinetostatic model (Case2) was within 12% when compared to the FEA results. The differences between the Jacobian matrix obtained from the kinetostatic model was within 4% for the translational motion Δx_o and was within 15% for the rotational motion $\Delta\alpha_o$ when compared to the FEA results. For the 3-RRR micro-motion stage, the differences of the compliance matrices obtained from the kinetostatic model (Case2) was within 10% when compared to the FEA results. The differences of the Jacobian matrix obtained from the kinetostatic model was within 11% when compared to the FEA results. These differences are mainly attributed to the unmodelled rigid-link deformations in the kinetostatic models.

The developed kinetostatic model in this thesis is advantageous over the FEA model. The kinetostatic model is derived in closed-form equations to estimate the kinematics and statics of compliant mechanisms; therefore FEA software is not required. Also, designs of micro-motion stages can be analysed quickly by changing the parameters in the analytical model. FEA models, on the other hand, require each individual design to be modelled and meshed separately using FEA

software (such as ANSYS) and the modelling process could be time consuming. Furthermore, commercial FEA modelling software may be expensive.

CHAPTER 7

Experimental Validation of the Kinetostatic and FEA Models

Experiments were conducted to measure the compliances and the Jacobian of the 3-RRR micro-motion stage. The experimentally determined compliance and Jacobian results were used to verify the accuracy of the analytical and FEA models presented in the previous chapters. The differences between the experimental, FEA and analytical results are presented and discussed in this chapter.

The experimentally determined compliance matrices of $\mathbf{C_{o,F_o}}$, $\mathbf{C_{o,F_{in}}}$ and $\mathbf{J_{exp}}$ matrix are presented. However the compliance matrix of $\mathbf{C_{in,F_{in}}}$ could not be measured due to the limitations of the experimental setup; therefore this result is not presented. Although the analytical $\mathbf{C_{in,F_{in}}}$ results could not be verified experimentally, the analytical results were verified with FEA results in Chapter 6.

The FEA results of $\mathbf{C_{o,F_o}}$, $\mathbf{C_{o,F_{in}}}$ and $\mathbf{J}$ matrices were also compared with the experimental results. Although the accuracy of the FEA determined $\mathbf{C_{in,F_{in}}}$ could not be verified experimentally, it was expected that the order of accuracy of the FEA determined $\mathbf{C_{in,F_{in}}}$ was approximately the same as the FEA determined $\mathbf{C_{o,F_o}}$, $\mathbf{C_{o,F_{in}}}$ and $\mathbf{J}$ matrices because the FEA modelling concept of determining these matrices was the same.

7.1 Experimentally determined compliance matrix, $\mathbf{C_{o,F_o}}$

The experimental setup of the compliance measurements is shown in Figure 7.1. Aluminium targets were mounted to the end-effector as shown in Figure 7.1. Three eddy-current sensors were mounted on the translation stages. The translation stages are used to position the sensors to their corresponding measurement ranges from the aluminium targets. The voltage signals of eddy-current sensors were recorded using a dSPACE DS1104 DSP controller board via the inbuilt analog-to-digital converters (ADCs).

Weights of 20, 50, 100 and 200g were hung on the stage along its x and y axes to provide the corresponding loading forces. To apply moments, a loading rod was mounted to the end-effector and weights were hung on the loading rod with a distance of 15 mm from the centre of the end-effector (see Figure 7.1b). When weights were applied, the corresponding voltage signals of the eddy-current sensors were recorded and converted to displacements according to their sensitivities (see Appendix A for sensor calibrations). The translational displacements, Δx_o and Δy_o, and the rotational displacements $\Delta \alpha_o$ of the end-effector were calculated from the displacements measured by the three eddy-current sensors.

The measured displacement Δy_o (when moments were applied via the loading rod) consists of a displacement component caused by forces, $F_{oy} = F_W$ and a displacement component caused by moments, $M_{oz} = F_W \times l$ where F_W is the force applied via the hanging weights (see Figure 7.2) and l = 15mm. In order to obtain the Δy_o-displacement which was only caused by M_{oz}, the displacement caused by F_{oy} was subtracted as shown in the equation below.

$$\Delta y_{o,Moz} = \Delta y_T - \Delta y_{o,Foy} \tag{7.1}$$

where $\Delta y_{o,Moz}$ is the displacement due to M_{oz}, $\Delta y_{o,Foy}$ is the displacement due to F_{oy} (measured when weights were applied at the centre of the end-effector) and Δy_T is the total displacement measured when weights are applied at a distance l from the centre of the end-effector.

Graphs of displacements versus forces or moments were plotted and the slopes of these graphs were obtained. There are a total of nine groups of graphs where each group of graphs represent each entry in the compliance matrix $\mathbf{C_{o,F_o}}$. There are a total of sixty sets of measurements in each group, providing a reasonable sample size to ensure the consistency of the experimental results. Figure 7.3 shows

the histogram of the measurement data of each entry of the $\mathbf{C_{o,F_o}}$ matrix together with the means and standard deviations.

7.1.1 Discussion

It can be observed in Figure 7.3 that the measurement data of $C_{o,Fo_{11}}$, $C_{o,Fo_{22}}$ and $C_{o,Fo_{33}}$ are normally distributed with small standard deviations (σ). The maximum deviation ($2\sigma/mean$) of the measurement from the mean value is 2%. This shows the consistency of the experimental data. The experimental results show that the compliances at the x- ($C_{o,Fo_{11}}$) and y-axis ($C_{o,Fo_{22}}$) are almost identical. This is expected because the 3-RRR compliant mechanism has a symmetrical topology.

The non-diagonal results are not normally distributed. This is because the compliances of the non-diagonal terms are very small. The 3-RRR micro-motion stage is a RCC device where deformations occur only along the direction of the applied forces/moments. Deformations at the non-loading directions are very small and the voltage signals that are recorded by the sensor are not accurate partly due to the limitation of the sensor resolutions. The maximum recorded voltage signal when measuring the deformations at the non-loading directions of the stage was within 1.1 mV which was less than the resolution of the eddy-current sensors (approximately 1.8mV). Therefore, it was most likely that random signal noises were recorded instead of the "actual" signals.

Since the compliances at the non-loading directions are very small, these compliances are ignored. The experimentally determined output compliance matrix is,

$$[\mathbf{C_{o,F_o}}]_{exp} = \begin{bmatrix} 13.12 & 0 & 0 \\ 0 & 12.95 & 0 \\ 0 & 0 & 28012 \end{bmatrix} \tag{7.2}$$

Analytical and FEA determined $\mathbf{C_{o,F_o}}$ matrices were compared to the experimental result of Equation 7.2 and the results of the comparisons are presented in Section 7.4.

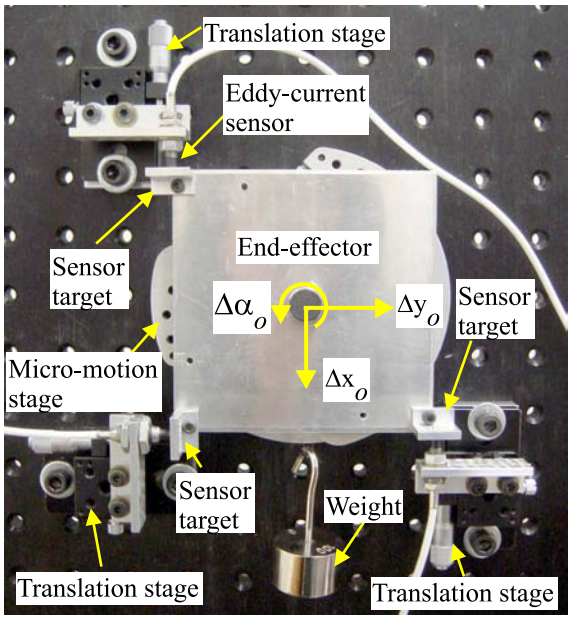

(a) Measurement of the translational compliances along the x- and y-axis

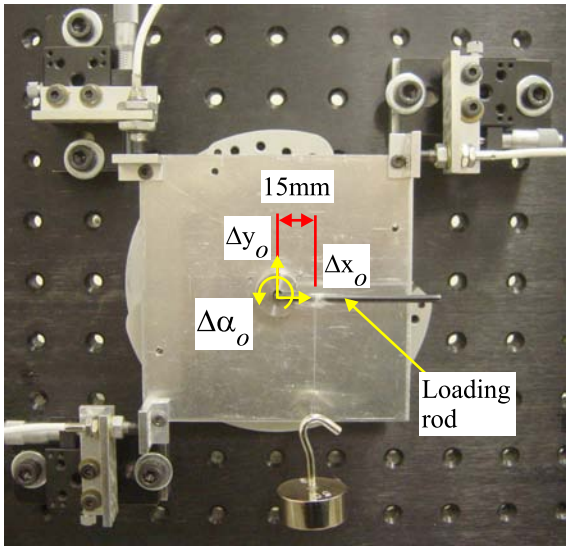

(b) Measurement of the rotational compliance about the z-axis

Figure 7.1: Experimental setup - the measurement of the compliances, $\mathbf{C_{o,F_o}}$

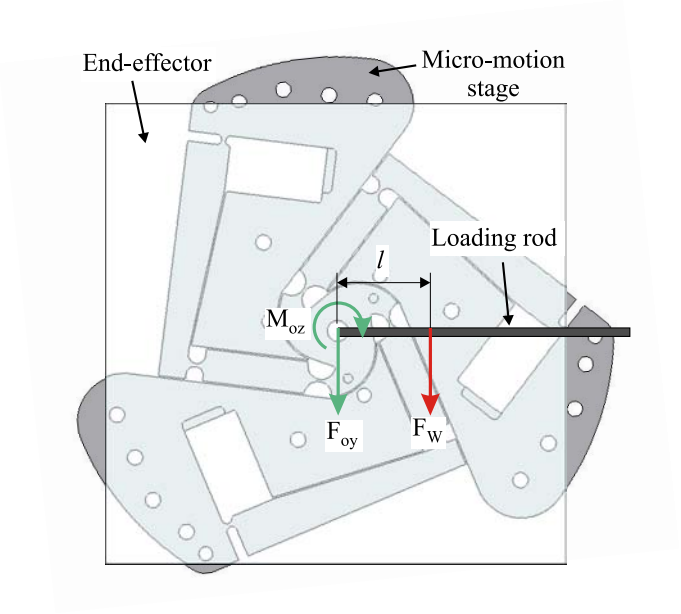

Figure 7.2: Equivalent forces/moment on the end-effector of the 3-RRR micro-motion stage when moments were applied via the loading rod

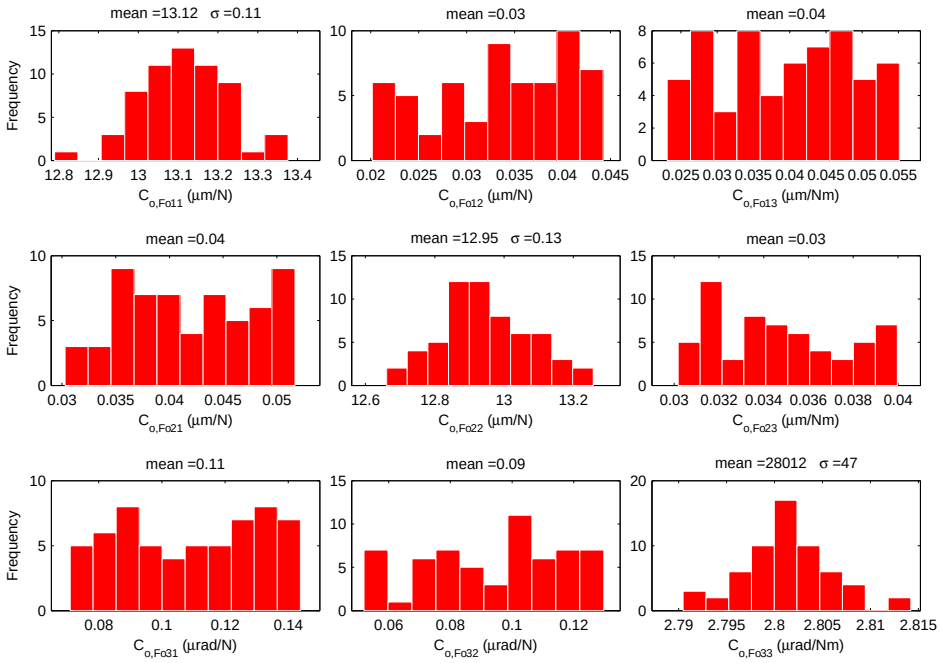

Figure 7.3: Histogram of the measurement data of C_{o,F_o}

7.2 Experimentally determined compliance matrix, $\mathbf{C_{o,F_{in}}}$

The experimental setup of the compliance measurements of $\mathbf{C_{o,F_{in}}}$ is shown in Figure 7.4. Weights of 20, 50, 100 and 200g were hung at the input locations of the stage as shown to provide the input forces. Three eddy-current sensors were used to measure the translational motions (Δx_o and Δy_o) along the x- and y-axis, and the rotational motions ($\Delta \alpha_o$) about the z-axis. The sensors were positioned as shown to measure the displacements of the targets. Similarly to the measurement of $\mathbf{C_{o,F_o}}$, graphs of displacements versus forces or moments were plotted and the slope of each graph was obtained. There are a total of nine groups of graphs where each group of graphs represent each entry in the compliance matrix of $\mathbf{C_{o,F_{in}}}$. There are a total of sixty sets of measurements in each group, providing a reasonable sample size to ensure the consistency of the experimental results. Figure 7.5 shows the histogram of the measurement data of each entry of the $\mathbf{C_{o,F_{in}}}$ matrix together with the means and standard deviations.

7.2.1 Discussion

It can be observed in Figure 7.5 that the measurement data of all the terms in $\mathbf{C_{o,F_{in}}}$ are normally distributed with small standard deviations (σ). The maximum deviation ($2\sigma/mean$) of the measurement from the mean value is 3.8%. This shows the consistency of the experimental data.

It can be noted that the first rotational compliance term of $[\mathbf{C_{o,F_{in}}}]_{exp}$ is larger than the rest of the two compliance terms. This does not match with the symmetrical characteristic of the micro-motion stage. An investigation was conducted and a manufacturing error was found at the preload mechanism of the first link (Handley, 2006). A diagram of the preload mechanism is shown in Figure 7.6. It can be seen that this preload mechanism uses a grub screw to apply compressive loads on the piezo-actuator to hold it in place. In order to measure the compliances ($\mathbf{C_{o,F_{in}}}$) of the micro-motion stage, weights were hung at the centre of the threaded hole using a pin as shown in Figure 7.7. Unfortunately the location of the threaded hole was mistakenly machined to have l_5= 4.5 mm instead of 4 mm. The distance of l_5 for the first link is 0.5 mm larger than the second and the third link. Therefore, the rotational compliance of the first link is larger than the rest of the links due to larger amount of moments applied. In order to have a meaningful comparison, the FEA and analytical models (except for $\mathbf{C_{o,F_o}}$ which is not affected by the location of the input forces) were modified to take the manufacturing error

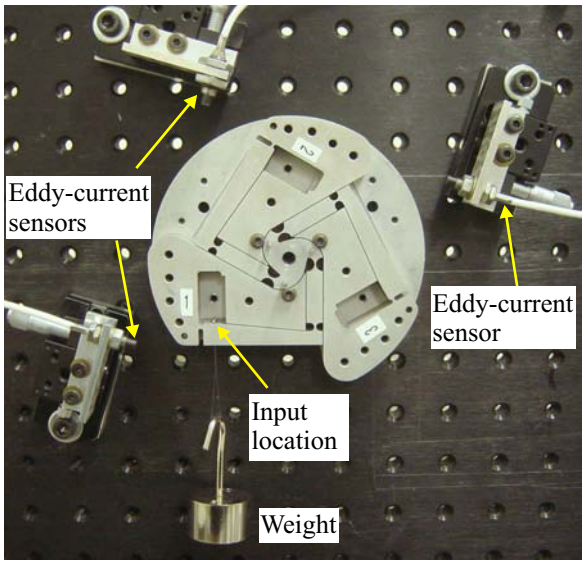

(a) Weights were hung at the input point

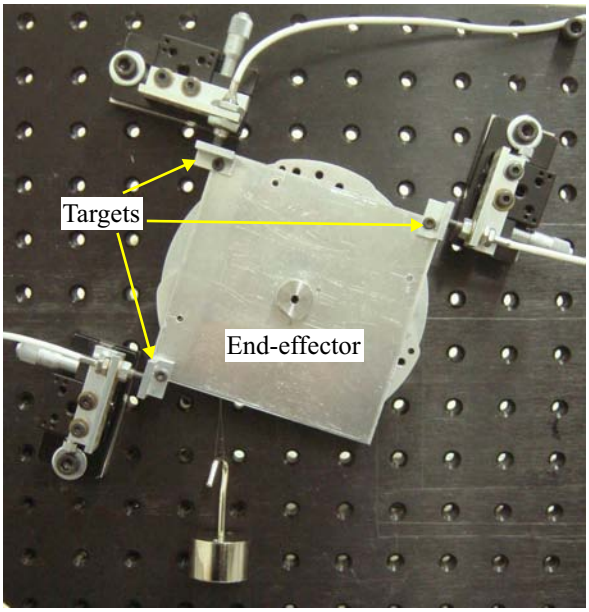

(b) Three eddy-current sensors were used to measure the displacements of the targets

Figure 7.4: Experimental setup of the measurement of $\mathbf{C_{o,F_{in}}}$

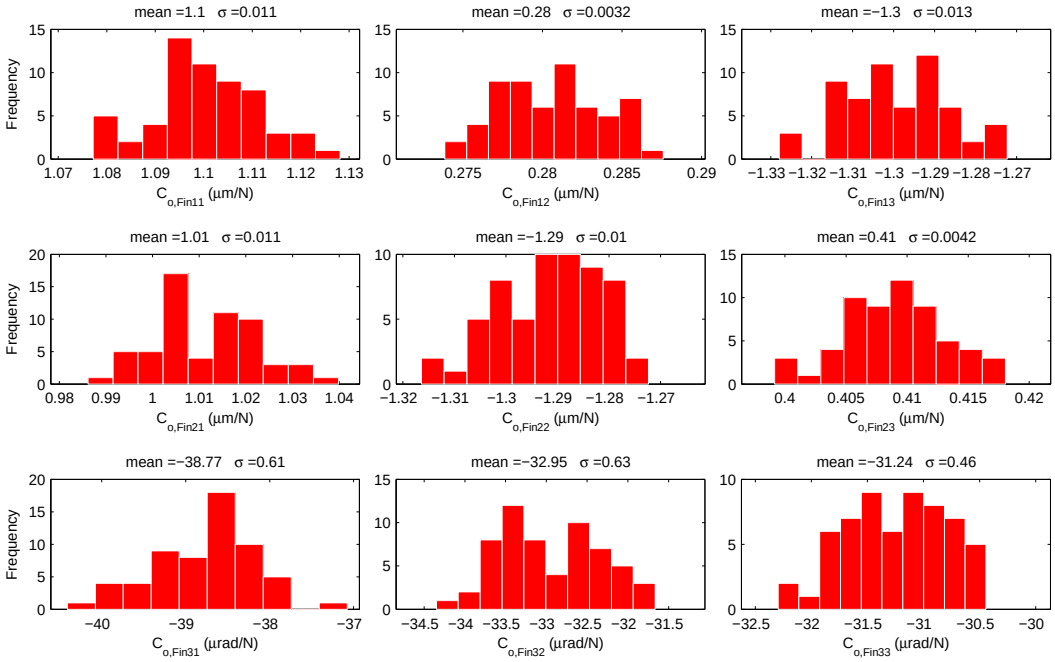

Figure 7.5: Histogram of the measurement data of $\mathbf{C_{o,F_{in}}}$

into considerations.

The experimentally determined compliance matrix $\mathbf{C_{o,F_{in}}}$ is,

$$[\mathbf{C_{o,F_{in}}}]_{exp} = \begin{bmatrix} 1.10 & 0.28 & -1.30 \\ 1.01 & -1.29 & 0.41 \\ -38.77 & -32.95 & -31.24 \end{bmatrix} \tag{7.3}$$

Analytical and FEA determined $\mathbf{C_{o,F_{in}}}$ matrices were compared to the experimental result of Equation 7.3 and the results of the comparisons are presented in Section 7.4.

7.3 Experimentally determined Jacobian matrix

The experimental technique presented by Handley (2006) was used to measure the Jacobian matrix of the 3-RRR micro-motion stage. An experimental Jacobian

NOTE: This figure is included on page 155 of the print copy of the thesis held in the University of Adelaide Library

Figure 7.6: Preload mechanism – compressive load on the piezo-actuator (Handley, 2006)

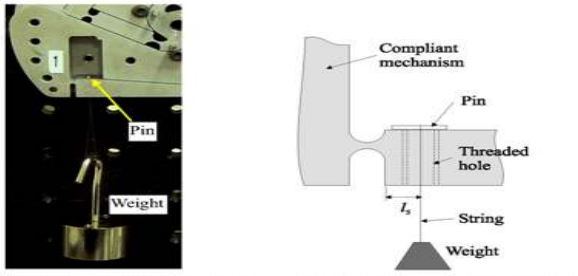

(a) Close-up photograph of the experimental setup

(b) Schematic of the experimental setup

Figure 7.7: Weights were hung at the input location of the micro-motion stage using a pin

NOTE: This figure is included on page 156 of the print copy of the thesis held in the University of Adelaide Library.

Figure 7.8: Closed-loop PI controller using strain gauge feedback (Handley, 2006)

matrix of the same stage was presented in Handley's thesis. The Jacobian was remeasured in this thesis to ensure that the experimental results did not vary over time. A more detailed experimental procedure than that of Handley (2006) is presented in this thesis.

The input displacements of the 3-RRR micro-motion stage were provided by three piezoelectric actuators. These three Tokin AE0505D16 stack actuators were assembled into the compliant mechanism using three preload mechanisms. Compressive forces were applied via a grub screw to hold the piezo-actuator in place (see Figure 7.6). A locked nut was used to secure the grub screw and the piezoactuator.

The preload forces will ensure constant contact between the piezos and the compliant mechanism during operations. Each piezo-actuator has a maximum elongation of 11.6±2μm with a 100V input voltage. Each piezo-actuator was driven by a Physik Instrumente (PI) amplifier, which provides a bipolar voltage ranging from -20V to 120V. The amplifiers have a maximum output power of 30W. Measurement Group EA-06-125TG-350 strain gauges were mounted to piezoactuators to measure their displacements. A full-bridge arrangement was used so that the strain gauges were temperature compensated. All strain gauges were connected to a strain gauge conditioner. Strain gauges serve as displacement sensors to the system; therefore the piezo-actuators could be controlled using closed-loop proportional-integral (PI) control. The closed-loop control is shown in Figure 7.8.

7.3.1 Strain gauge calibrations

The procedures of calibrating strain gauges and the Jacobian are similar to that of Handley (2006). Strain gauges were calibrated after they were assembled into the compliant mechanism. A Philtec D20 fibre-optic sensor was used to calibrate these strain gauges. A front surface mirror, which was the target of the fibre-optic

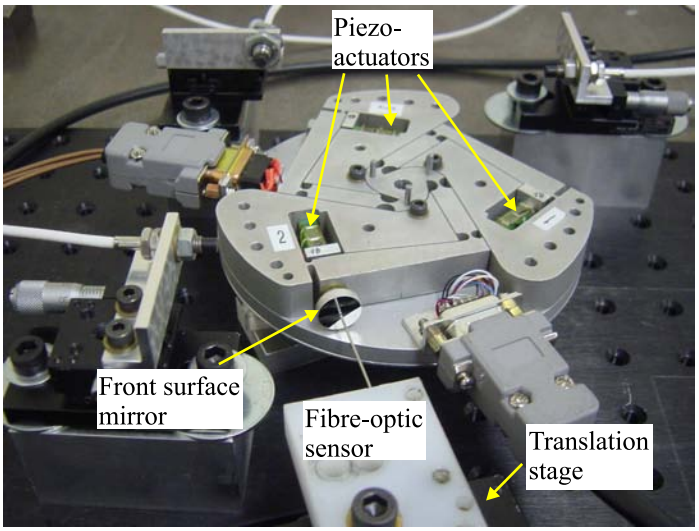

Figure 7.9: Strain gauge calibration setup

sensor, was attached to the side of an input link as shown in Figure 7.9. The fibre-optic sensor was positioned as shown to measure the displacement of the mirror. The fibre-optic sensor was mounted on a NanoFlex^{TM} translation stage which had a travel range of 5 mm and a resolution of 50 nm. The translation stage was used to position the fibre-optic sensor to its measurement range. The fibre-optic sensor was aligned with the axis of the preload mechanism so that the displacements at the point of force input were recorded. In order to check the alignment, the tip of the fibre-optic sensor was positioned in the middle of the lock nut as shown in Figure 7.10. As mentioned by Handley (2006), there are advantages of measuring the displacement of the compliant input link rather than the length of change of the piezo-actuator. The advantages are a) the measured Jacobian will give the relationship between the input link displacement and the end-effector displacements, which is in accordance with the way the analytical Jacobian matrix was derived, and b) any unmodelled compliance in the preload mechanism will not cause discrepancies between the experimental and analytical results.

Each piezo-actuator was elongated by providing an increasing voltage from 0 to 100V. The output voltages of each strain gauge and their corresponding input link displacements (measured by the fibre-optic sensor) were recorded. Graphs of displacements against strain gauge voltages were plotted and linear lines were fitted through the data points. Slopes of these graphs which represent the sensitivity of the strain gauge were obtained. The average sensitivity of each strain gauge is shown in Table 7.1.

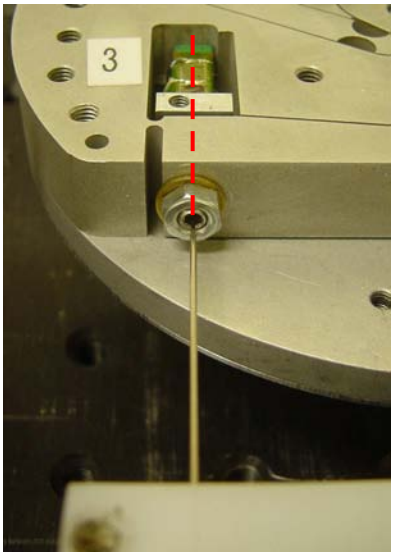

(a) Fibre-optic sensor is aligned with the preload mechanism axis

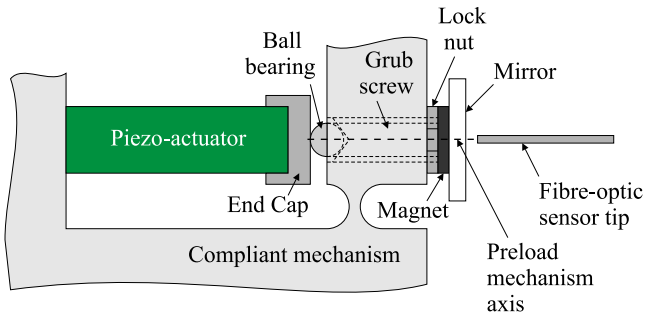

(b) Schematic of the preload mechanism and the alignment of the fibre-optic sensor (Handley, 2006)

Figure 7.10: Alignment of the fibre-optic sensor with the axis of the preload mechanism

	Sensitivity (μm/V)
Strain gauge 1	0.8513
Strain gauge 2	0.7926
Strain gauge 3	0.8235

Table 7.1: Average sensitivities of strain gauges

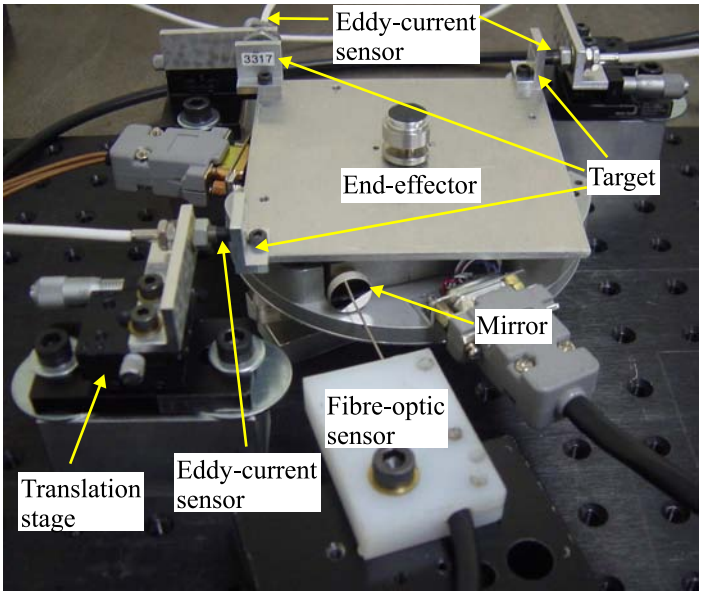

Figure 7.11: Experimental setup of measuring the Jacobian of the 3-RRR micro-motion stage

7.3.2 Jacobian measurements

The output displacements (Δx_o, Δy_o, $\Delta \alpha_o$) of the end-effector were measured using the three eddy-current sensors as shown in Figure 7.11. Targets of the eddy-current sensors were mounted to the end-effector. The three eddy-current sensors were positioned as shown in the figure to measure the displacement of the targets. The translational displacements, Δx_o and Δy_o, and the rotational motions, $\Delta \alpha_o$ of the end-effector were calculated from displacements measured by the eddy-current sensors. The piezo-actuator driver was connected to the dSPACE board via the inbuilt digital-to-analog converters (DACs), while the strain gauge conditioning circuitry and the eddy-current transducers were connected to the dSPACE board via the inbuilt ADCs. A schematic of the experimental setup is shown in Figure 7.12.

The piezo-actuator was extended one at a time by applying an increasing voltage from 0 to 100V. Displacements of the other two piezo-actuators were constrained to be zero. The displacements of the three piezo-actuators were controlled using closed-loop PI feedback controllers constructed in Simulink, Matlab. Output displacements of the end-effector (Δx_o, Δy_o, $\Delta \alpha_o$) were measured by the three eddy-current sensors while each of the piezo-actuator was displaced (that is the input displacement, u_{1in} , u_{2in}, u_{3in}) individually. Graphs of output displacements versus input displacements were plotted and the slope of each graph was obtained. There are a total of nine groups of graphs where each group of graphs

NOTE: This figure is included on page 160 of the print copy of the thesis held in the University of Adelaide Library.

Figure 7.12: Schematic of the experimental setup to measure the Jacobian (Lu et al., 2004)

Eddycurrent sensor	Sensitivity (μm/V)
3316	10.264
3317	10.099
3338	10.184

Table 7.2: Sensitivities of the three eddycurrent sensors (0 to 10V)

represents each entry in the Jacobian matrix. There were a total of 150 sets of measurement in each group, providing a good sample size to ensure the consistency of the experimental results. Figure 7.13 shows the histogram together with the means and standard deviations of the measurement data of each entry of the Jacobian matrix, $J_{exp.}$

7.3.2.1 Discussion

It can be observed in Figure 7.13 that some of the measurement data of the J_{exp} terms follow the trend of a normally distributed curve with small standard deviations (σ). The maximum deviation ($2\sigma/mean$) of the measurement from the mean value is 0.8%. This shows the consistency of the experimental data.

It can be seen in Figure 7.13 that the mean value of $J_{exp_{31}}$ is smaller than $J_{exp_{32}}$ and $J_{exp_{33}}$. This was due to the manufacturing errors at the preload mechanism of the first link. As mentioned in Section 7.2.1, the distance of l_5 for the first link is 0.5 mm larger than the second and the third link. Therefore, the amplification ratio (output displacement over input displacement) of the first link was smaller than the rest of the links. The slight differences between $J_{exp_{32}}$ and $J_{exp_{33}}$ could be attributed to manufacturing errors and the uneven preload applied on the piezoactuators.

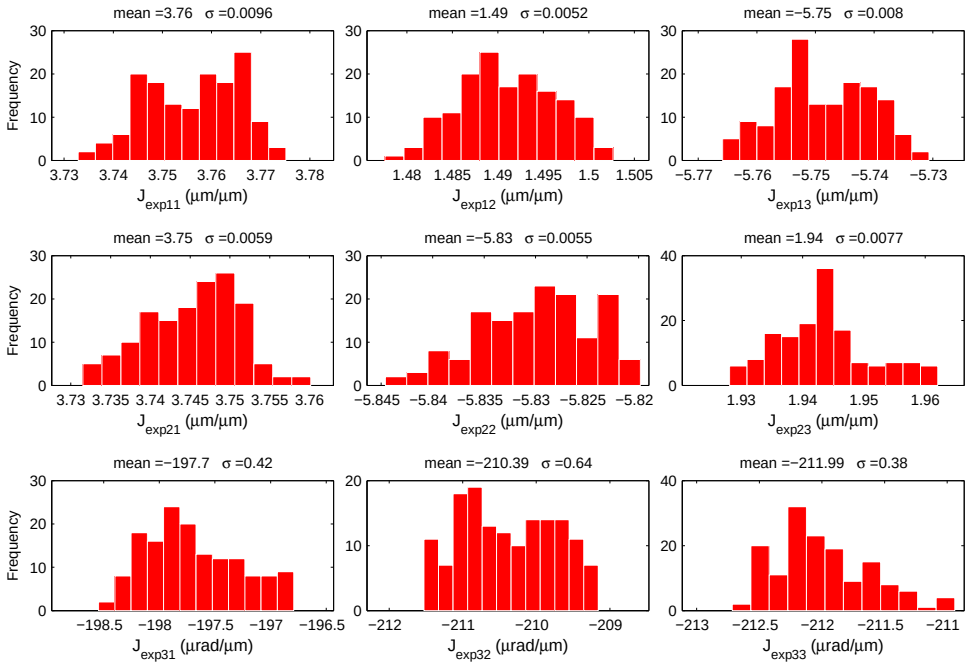

Figure 7.13: Histogram of the measurement data of $\mathbf{J_{exp}}$

7.3.3 Comparison of $\mathbf{J_{exp}}$ results

A comparison was conducted between the experimental Jacobian matrix presented in this thesis and that presented in Handley (2006). Table 7.3 shows the Jacobian matrices and their differences relative to the measured Jacobian in this thesis. The differences between the two Jacobian matrices are small (within 6.7%). The differences could be attributed to a) the differences of room temperatures when experiments were conducted, b) the differences of the calibrated strain gauge sensitivities, and c) the differences in the alignment of sensors during the experimental setup. The change of room temperature affects the measurement range of the sensors (see Appendix A). The measurement range of the sensors decrease with the increase of room temperature. If the measured voltages fall outside the measurement range of the sensors, the sensitivities of the sensors will be different from that shown in Table 7.2, which leads to the differences between the two measured Jacobians. The differences of the strain gauge sensitivities could not be quantified as there were not presented in Handley (2006). The distances between sensors and the alignment of the sensors to their aluminium targets may be slightly different from that of the experimental setup conducted by Handley (2006). The position-

$\mathbf{J_{exp}}$ (this thesis)			$\mathbf{J_{exp}}$ (Handley, 2006)			% difference		
3.76	1.49	−5.75	3.84	1.40	−5.62	2.1	−6.0	−2.3
3.75	−5.83	1.94	3.87	−5.44	1.84	3.2	−6.7	−5.2
−197.70	−210.39	−211.99	−199.77	−211.90	−209.42	1.0	0.7	−1.2

Table 7.3: Differences between the two experimental Jacobian matrices

ing and the alignment of sensors may contribute to the differences between the two experimental Jacobians. The sample size of the Jacobian measurements were not mentioned in Handley (2006); therefore the standard deviation and the consistency of Handley's results were unclear. Nevertheless, the two measured Jacobian matrices were closed to each other especially for the rotational terms, $J_{exp_{31}}$, $J_{exp_{32}}$ and $J_{exp_{33}}$.

7.4 Comparisons of analytical and FEA results with experimental results

In order to facilitate a comparison with experimental results, the FEA and analytical models (except for $\mathbf{C_{o,F_o}}$ which is not affected by the dimension l_5) were modified to take the manufacturing error into consideration. Table 7.4, 7.5 and 7.6 show the differences of the analytical and FEA results when compared to experimental results.

Experimentally determined $\mathbf{C_{o,F_o}}$		
13.12	0	0
0	12.95	0
0	0	28012

Kinetostatic Model						FEA compliance		
Case 1			Case 2					
10.10	0	0	12.25	0	0	11.50	0	0
0	10.10	0	0	12.25	0	0	11.48	0
0	0	23960	0	0	27402	0	0	27966
% difference compared to experimentally determined $\mathbf{C_{o,F_o}}$								
-23.0	$--$	$--$	-6.6	$--$	$--$	-12.4	$--$	$--$
$--$	-22.0	$--$	$--$	-5.4	$--$	$--$	-11.4	$--$
$--$	$--$	-14.5	$--$	$--$	-2.2	$--$	$--$	-0.16

Table 7.4: Comparison of analytical and FEA results of $\mathbf{C_{o,F_o}}$ with that of the experiments

Experimentally determined $\mathbf{C_{o,F_{in}}}$		
1.10	0.28	−1.30
1.01	−1.29	0.41
−38.77	−32.95	−31.24

Kinetostatic Model						FEA compliance		
Case 1			Case 2					
0.85	0.22	−1.00	1.04	0.27	−1.22	0.96	0.26	−1.14
0.77	−1.2	0.32	0.94	−1.25	0.39	0.88	−1.16	0.36
−32.72	−29.79	−29.79	−37.65	−34.30	−34.30	−35.24	−32.25	−32.12
% difference compared to experimentally determined $\mathbf{C_{o,F_{in}}}$								
−22.6	−20.6	−23.2	−5.4	−4.7	−6.5	−12.4	−8.3	−12.6
−23.5	−21.7	−22.2	−7.1	−3.3	−4.1	−12.9	−10.0	−13.0
−15.6	−9.6	−4.6	−2.9	4.1	9.8	−9.1	−2.1	2.8

Table 7.5: Comparison of analytical and FEA results of $\mathbf{C_{o,F_{in}}}$ with that of the experiments

Experimentally determined Jacobian, $\mathbf{J_{exp}}$		
3.76	1.49	−5.75
3.75	−5.83	1.94
−197.70	−210.39	−211.99

Analytical Jacobian						$\mathbf{J_{PRBM}}$			FEA Jacobian, $\mathbf{J_{FEA}}$		
Case 1			Case 2								
4.33	1.37	−6.13	4.32	1.34	−6.08	4.25	1.47	−6.13	3.95	1.25	−5.50
3.94	−6.28	1.96	3.90	−6.25	1.97	4.00	−6.24	1.84	3.62	−5.65	1.73
−244.07	−268.11	−268.11	−242.61	−266.33	−266.33	−262.95	−288.73	−288.73	−223.57	−241.32	−240.48
% difference compared to experimentally determined Jacobian, $\mathbf{J_{exp}}$											
15.2	−8.2	6.5	15.0	−10.2	5.8	13.0	−1.3	6.7	5.1	−16.1	−4.4
5.0	7.8	0.9	4.1	7.2	1.4	6.7	6.9	−5.0	−3.5	−3.2	−10.6
23.5	27.4	26.5	22.7	26.6	25.6	33.0	37.2	36.2	13.1	14.7	13.4

Table 7.6: Comparison of analytical and FEA Jacobians with the experimental Jacobian

7.4.1 Discussion

7.4.1.1 Differences between the analytical and experimental compliance matrices

From Table 7.4 and 7.5, it can be seen that the differences of the analytical compliance results in Case 2 are much smaller than that in Case 1 when compared to the experimental results. This is expected because the flexure hinge equations used to calculate the compliance matrices of Case 2 have smaller differences (when compared to the FEA results) than that of Case 1. The average absolute difference of $\mathbf{C_{o,F_o}}$ is reduced from 19.2% to 4.1%. The average absolute difference of $\mathbf{C_{o,F_{in}}}$ is reduced from 18.2% to 5.3%.

The differences between the analytical and the experimental compliance results could be attributed to a) measurement errors during experiments, b) unmodelled deformations of rigid-links in the analytical models, c) applied load types, and d) manufacturing errors of the 3-RRR micro-motion stage.

7.4.1.1.1 Measurement errors of compliance matrix, $\mathbf{C_{o,F_o}}$ During the measurements of $\mathbf{C_{o,F_o}}$, weights were hung from a spacer (which was used to separate the end-effector and the micro-motion stage) with a distance *k* from the centre of the micro-motion stage (see Figure 7.14a). Out-of-plane moments were generated due to the distance *k*. It was assumed that the out-of-plane moments will not cause any in-plane deformations to the micro-motion stage. However this out-of-plane deformations could contribute to the measurement errors. An investigation was carried out to study the effect of the out-of-plane rotational motions to the measurement errors. Weights were hung from the end-effector which was further from the centre of the stage as shown in Figure 7.14b and the compliances were once obtained. The compliances were found to be approximately 2.8% larger than that when the weights were hung from the spacer (see Figure 7.14a). The out-of-plane moment caused the end-effector to tilt with a small angle. This small tilting angle was exaggerated in Figure 7.15. Both the deformations of the micro-motion stage and the motions at the end of the end-effector caused by the tilting angle were measured during the experiments. This could explain why the experimentally determined $\mathbf{C_{o,F_o}}$ is larger than that of the analytical values. Although weights were hung at the spacer during the experiments, the motions of the end-effector caused by the out-of-plane moments could not be avoided.

7.4.1.1.2 Measurement errors of compliance matrix, $\mathbf{C_{o,F_{in}}}$ Measurement errors of $\mathbf{C_{o,F_{in}}}$ could be attributed to the hanging locations of the weights. Weights

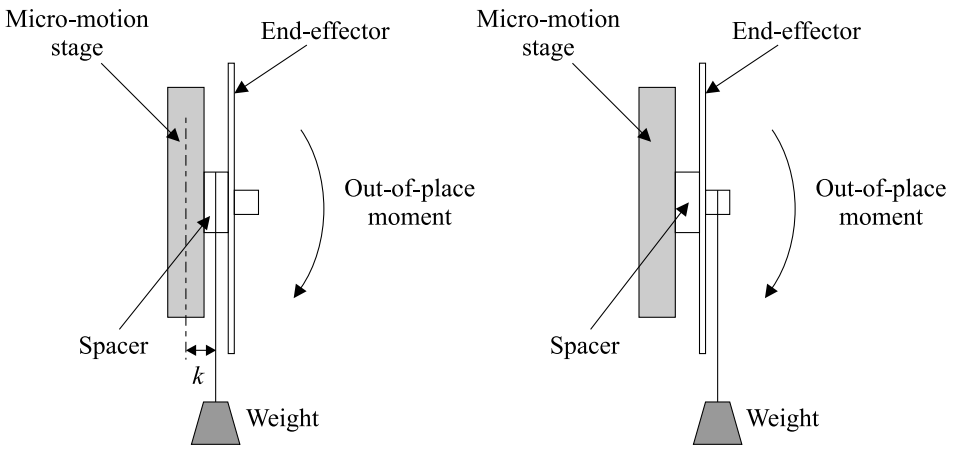

(a) Weight is hung from the spacer (b) Weight is hung from the end-effector

Figure 7.14: Side view of the experimental setup of measuring $\mathbf{C_{o,F_o}}$

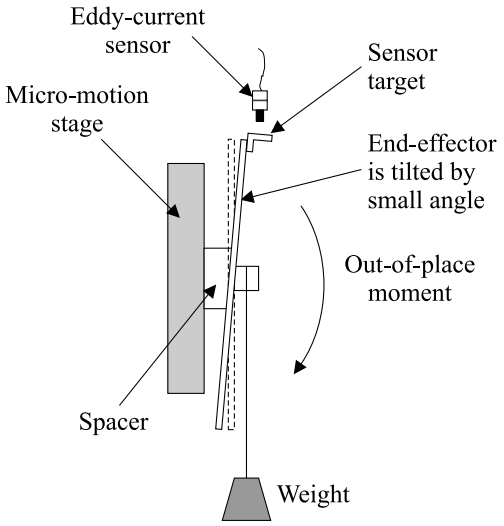

Figure 7.15: Small tilting angle (exaggerated in the diagram) of the end-effector

may not be hung exactly at the location of the input point. A pin was used as shown in Figure 7.7 to locate the weights at the input points. The pin was located as close to the centre of the hole (input point) as possible. However due to the thickness of the pin, misalignments were difficult to avoid.

7.4.1.1.3 Unmodelled deformations of rigid-links The kinetostatic model assumes that the deformations of rigid-links of the micro-motion stage are small, and therefore are ignored. This assumption is made because the 3-RRR compliant structure is not an over-constrained structure. Therefore, deformations are not expected at rigid-links. However, the small differences between analytical and the experimental results could be due to these unmodelled rigid-link deformations.

7.4.1.1.4 Applied load types It was observed that there are some errors when comparing the analytical $\mathbf{C}_{\mathbf{o},\mathbf{F_{in}}}$ results to that of experiments. This could be attributed to the difference of the type of loads applied. For the analytical model, point loads were applied at the input points to obtain their compliance results. However, during experiments, distributed loads were applied at the input locations through a pin instead. Applying point loads at the input locations during experiments were impractical due to the threaded hole and also due to the limitation of the experimental setup.

7.4.1.1.5 Manufacturing errors of the 3-RRR micro-motion stage The machining errors in the position and size of the holes of circular flexure hinges may have an influence on the compliances of hinges (Ryu and Gweon, 1997). The flexure hinge compliance equations in Appendix C were expressed as a function of t, b, θ_m, R and material properties of the hinge. Small variations in each of these dimensions during the manufacturing process would vary the compliances of the mechanism. This could partly explain the differences between the analytical compliance results (the ideal hinge models) of the 3-RRR micro-motion stage when compared to the experimental results.

7.4.1.2 Differences between the FEA and experimental compliance matrices

The differences between the FEA and experimental compliances could be attributed to a) measurement errors as explained in Section 7.4.1.1.1, b) the differences of the type of loads applied as explained in Section 7.4.1.1.4, and c) manufacturing errors of the 3-RRR micro-motion stage as explained in Section 7.4.1.1.5.

The FEA compliances were observed to be smaller than the experimentally determined compliances. The under-estimated FEA results may be attributed to the type of elements used in the FEA model, namely the plane stress element. As reported by Schotborgh *et al.* (2005), plane stress elements may provide a 5 to 10% under-estimation of the stiffnesses. Plane stress elements were chosen over plane strain elements because plain strain elements provide an even greater over-estimation of the stiffnesses (Schotborgh *et al.*, 2005). A three-dimensional (3-D) FEA model would provide more accurate results than the two-dimensional (2-D) model; however an accurate 3-D FEA model is not feasible due to the limited number of nodes available from the academic ANSYS license.

7.4.1.3 Differences between the Jacobian matrices

The Jacobian matrix of Case 2 was expected to be more accurate than that of Case 1; however both the Jacobian matrix of Cases 1 and 2 provide similar accuracies as shown in Table 7.6. This is because the Jacobian matrix represents the kinematics of the micro-motion structures; therefore the Jacobian is almost independent of compliances or stiffnesses of flexure hinges.

It can be observed in Table 7.6 that overall, the FEA Jacobian gives the closest prediction to the experimental results. The analytical Jacobian matrices obtained from the kinetostatic model give similarly close prediction of the translational motions but provide less accurate predictions of the rotational motions. However, these Jacobian matrices are more accurate than that of the Jacobian derived using the PRBM method especially in the rotational terms. This is because the Jacobian matrix obtained using the kinetostatic model considers flexure hinges to have three-DOF while the PRBM derived in this thesis models flexure hinges to have only one-DOF.

The differences between the analytical and the experimental Jacobians could also be attributed to the unmodelled rigid-link deformations in the analytical model as explained in Section 7.4.1.1.3 and the manufacturing errors of the 3-RRR micro-motion stage as explained in Section 7.4.1.1.5.

7.5 Concluding remarks

The kinetostatic results of Case 2 were closer to the experimental results than that of Case 1 especially for the compliance matrices. This indicated the importance of the selection of flexure hinge compliance equations when calculating the kinetostatics of compliant micro-motion stages. It also highlighted a) the significance of

the scheme developed in Chapter 3, and b) the advantage of the derived closed-form kinetostatic model with flexure hinge compliances as one of the variables in the equations. The accuracy of the compliance matrices obtained from the kinetostatic model (Case2) was within 7% when compared to the experimental results. The accuracy of the Jacobian matrix obtained from the kinetostatic model was within 15% for the translational motions and was within 26% for the rotational motion when compared to the experimental results. However, these differences could be attributed to measurement errors, the unmodelled rigid-link deformations in the kinetostatic model, the differences of applied load types and the manufacturing errors of the micro-motion stages.

The Jacobian matrix obtained from the kinetostatic model provides better prediction of the rotational motions of the 3-RRR micro-motion stage when compared to that of the PRBM (which does not model the Δx- and Δy-deformations of flexure hinges). As mentioned in Section 6.1.1.2, it is possible to extend the PRBM method to model flexure hinges to have multi-DOF. However, the extended PRBM method produces a large number of variables which required extensive computational effort to solve. Unlike the kinetostatic model derived in this thesis, the kinetostatic model is a simple closed-form model and it does not require extensive computational effort to solve.

CHAPTER 8

Conclusions and Future Work

This chapter summarises the work presented in this thesis, highlights the contributions of this thesis and presents the recommendations for future work.

8.1 Objectives of the study

There are two main objectives of this thesis. The first objective is to develop a scheme for selecting the most suitable circular flexure hinge equations from the previously derived formulations. There were various flexure hinge equations derived previously using different methods to predict the compliances of circular flexure hinges. However, it was found that some of these analytical/empirical compliance equations provided better accuracies than the others depending on the t/R ratios of circular flexure hinges, and flexure hinge compliance equations derived previously by any particular method may not be accurate for a large range of t/R ratios. There was no proper scheme developed on how to select the most suitable and accurate hinge equation from the previously derived formulations. Therefore, a scheme to guide designers for selecting the most suitable hinge equation based on the t/R ratios of circular flexure hinges is developed and presented in this thesis.

The second objective of this thesis is to develop a simple methodology of deriving an accurate kinetostatic model of four-bar and 3-RRR compliant micro-motion stages by incorporating the scheme developed in the first objective. The methodology models flexure hinges to have three-DOF. The kinetostatic model is derived to have closed-form equations. Material properties and link parameters are vari-

ables in this model. Compliances of flexure hinges are also one of the variables in the model. Therefore the most suitable flexure hinge equations can be selected based on the scheme developed in the first objective to calculate the kinetostatics of compliant micro-motion stages accurately.

8.2 Summary of the research work presented in this thesis

In Chapter 2, a thorough review of the literature on the modelling of flexure hinges was conducted. The chapter presents an overview on methods and equations derived previously using various methods to calculate the compliances of circular flexure hinges. It was identified that the compliance results of a circular flexure hinge calculated using these equations were different from each other. It was also found that the accuracy of these previously derived equations changes with the t/R ratio of circular flexure hinges. There was no proper scheme developed to guide researchers on how to select the most suitable flexure hinge compliance equations out of the previously derived formulations. Therefore, a scheme for selecting the most suitable hinge equation based on the t/R ratio of circular flexure hinges was developed in this thesis. A review of the literature on the kinetostatic modelling of compliant micro-motion stages was also conducted thoroughly. Several research groups derived kinetostatic models to predict the kinematics and statics of compliant mechanisms. However, there were only few research groups who studied the kinetostatics of 3-RRR compliant micro-motion stages. Some of these kinetostatic models involved an intensive number of transformation matrices which could lead to modelling complications and difficulties. Furthermore, not all the previously derived kinetostatic models provided the predictions of the kinematics and both the input and output stiffnesses of compliant micro-motion stages. The prediction of the input stiffness was particularly important for the design of piezo-driven compliant mechanisms because the maximum displacement of a piezo-actuator is governed by the structural input stiffness. High input stiffness will reduce the maximum displacement of a piezo-actuator, which leads to the reduction of the workspace of compliant mechanisms. As a conclusion, the kinetostatic modelling of compliant mechanisms, especially for 3-RRR micro-motion stages have still not been studied in great detail.

In Chapter 3, a scheme for selecting the most suitable circular flexure hinge equation based on the t/R ratio of hinges was developed and presented. Compliances of circular flexure hinges determined using a FEA simulation (ANSYS)

were used as a benchmark for comparisons. Experiments were conducted to measure the compliances of three flexure hinges in order to investigate the accuracy of the FEA results and to ensure that the FEA results were suitable to be used as the benchmark. The three flexure hinges have t/R ratios from each of the categories of thin ($t/R \leq 0.07$), intermediate ($0.07 < t/R \leq 0.2$) and thick ($0.2 < t/R \leq 0.8$) hinge respectively in order to cover a wide range of t/R ratios. The FEA results were in good agreement with the experimental results (within 3% difference for $\Delta\alpha_z$-compliance and 6% difference for Δy-compliance). The FEA results were also compared to the experimental results of Smith *et al.* (1997) to further justify the accuracy of the FEA model. The FEA results were in close agreement (within 6.2%) with the experimental results of Smith *et al.* (1997). Therefore, the FEA model presented in this thesis is suitable to serve as the benchmark for comparisons. The results of various flexure hinge compliance equations (Paros and Weisbord, 1965; Lobontiu, 2003; Wu and Zhou, 2002; Tseytlin, 2002; Smith *et al.*, 1987; Schotborgh *et al.*, 2005; Zhang and Fasse, 2001) were compared with that of the FEA model for flexure hinges with $0.05 \leq t/R \leq 0.8$. Based on the result of comparisons, the scheme for selecting the most suitable flexure hinge compliance equation was developed. Throughout the comparison process, it was also found that there was no accurate equation (within 5% error when compared to FEA results) to predict the Δx- and Δy-compliance of circular flexure hinges for a wide t/R range ($0.05 \leq t/R \leq 0.8$). Therefore, general empirical equations were developed based on FEA results to estimate the Δx- and Δy-compliance of circular flexure hinges for $0.05 \leq t/R \leq 0.8$.

Kinematic models of a four-bar and a 3-RRR micro-motion stage were derived using the PRBM method and the loop-closure theory, and were presented in Chapter 4. The kinematic model which was derived in a form of a Jacobian matrix was linear and simple. However the PRBM in this thesis does not model the Δx- and Δy-displacements of flexure hinges which led to modelling inaccuracy of compliant mechanisms. The modelling accuracy of the Jacobian matrix derived using the PRBM method was verified by comparing with FEA and experimental results in Chapters 6 and 7.

In Chapter 5, the derivation of kinetostatic models of a four-bar and a 3-RRR micro-motion stage were presented. Flexure hinges were modelled to have three-DOF. The kinetostatic model was derived to have closed-form equations where material properties, link lengths and flexure hinge compliances were variables in the model. Since flexure hinge compliances were one of the variables in the model, the scheme developed in Chapter 3 was incorporated into the model in order to obtain an accurate prediction of the kinetostatics of the two compliant stages. Two

cases were studies for both the four-bar and 3-RRR micro-motion stages where the kinetostatic models of Case 1 were calculated by deliberately choosing the flexure hinge equations with large differences (when compared to FEA results) based on the scheme developed in Chapter 3. Meanwhile, the kinetostatic models of Case 2 were obtained by choosing the flexure hinge equations with small differences. The compliance results of the two cases were noticeably different which indicated that the choice of flexure hinge compliance equations affects the accuracy of the kinetostatic models. The kinematic results which were derived in a form of Jacobian matrices showed close results for both cases. This was because the Jacobian matrix represented the kinematics of the micro-motion structures and the choice of flexure hinge equations used to calculate the analytical results has minimal effects on the results of the Jacobian matrix.

In Chapter 6, FEA models of the four-bar and the 3-RRR micro-motion stage were constructed using ANSYS. The FEA determined kinetostatic results of the compliant stages were used to validate the accuracy of the kinetostatic models. It was found that the kinetostatic results of Case 2 for both compliant mechanisms were closer to the FEA results than that of Case 1 except for the Jacobian matrix. This was because the Jacobian matrix represented the kinematics of the micro-motion structures. The choice of flexure hinge equations used to calculate the analytical results has minimal effects on the results of the Jacobian matrix. The improvement of the results of Case 2 indicated the importance of the selection of flexure hinge compliance equations when calculating the kinetostatics of compliant micro-motion stages. It also highlighted a) the significance of the scheme developed in Chapter 3, and b) the advantage of the derived closed-form kinetostatic model with flexure hinge compliances as one of the variables in the equation. The Jacobian matrix derived using the PRBM method and the loop-closure theory was also compared to the FEA results. It was found that the Jacobian results determined from the kinetostatic model were closer to the FEA results than that of the PRBM method in this thesis (which ignored the modelling of the Δx- and Δy-deformations of flexure hinges).

In Chapter 7, experiments were conducted to measure the compliances and Jacobian of the 3-RRR micro-motion stage in order to validate the kinematic model derived using the PRBM, the kinetostatic and the FEA models. It was found that the kinetostatic results of Case 2 were closer to the experimental results than that of Case 1 especially for the compliance matrices in the model. Overall, the FEA determined Jacobian provided the closest prediction to the experimental results. The analytical Jacobian matrices obtained from the kinetostatic model gave similarly close predictions of the translational motions but provided less accurate predic-

tions of the rotational motions. However, the Jacobian matrices obtained from the kinetostatic models were more accurate than that of the Jacobian derived using the PRBM method (which does not model the Δx- and Δy-deformations of flexure hinges) especially for the rotational terms. It is possible to extend the PRBM method to model flexure hinges to have multi-DOF. However, the extended PRBM method produces a large number of variables which require extensive computational effort to solve. Unlike the kinetostatic model derived in this thesis, the kinetostatic model is a simple closed-form model and it does not require extensive computational effort to solve.

8.3 Contributions

The work presented in this thesis has made several contributions to the current knowledge:

- A review on the accuracies and limitations of previously derived circular flexure hinge compliance equations was presented. This review has provided a good indication that the accuracy of most of the previously derived hinge equations vary with the t/R ratio of flexure hinges.
- A scheme for selecting the most suitable circular flexure hinge compliance equations based on the t/R ratio of a hinge was developed.
- A method was presented to derive linear and simple kinematic models using the PRBM and the loop-closure theory.
- A simple methodology was presented to derive a closed-form kinetostatic model of four-bar and 3-RRR compliant micro-motion stages. The kinetostatic model provides accurate predictions of kinematics, and both the input and output compliances of compliant micro-motion stages. The closed-form kinetostatic model was derived with flexure hinge compliance equations as one of the variables, and the most suitable flexure hinge equation can be used to accurately estimate the kinetostatics of compliant micro-motion stages.
- This work has given a good indication that the accuracy of the kinetostatic model is dependent on the accuracy of the flexure hinge compliance equations.
- The developed scheme for selecting flexure hinge equations and the derived kinetostatic model are useful for parametric studies and design optimisations of micro-motion stages.

8.4 Recommendations for future work

- The compliance equations ($\Delta x/F_x$ and $\Delta y/F_y$) of Schotborgh *et al*. (2005) had large errors compared to other research groups. This may be attributed to the uncertainties in their FEA model where the stiffnesses of hinges vary with the heights of the FEA model. The change of the hinge stiffness with the change of the height of their FEA model is recommended to be investigated in future.

- The current scheme for selecting flexure hinge equations was developed based on the t/R ratio of flexure hinges. The scheme could be extended to include more dimensions of flexure hinges, such as b/R and h/R, in order to provide more details on how the accuracy of various compliance equations vary with these hinge dimensions.

- The current scheme was developed for in-plane compliances of circular flexure hinges. The scheme can be extended to include out-of-plane compliances of the hinges.

- The kinetostatic model derived in this thesis suffered some inaccuracies which are attributed to the unmodelled deformation of rigid-links. The kinetostatic model could be extended to include the deformation of links in order to investigate the effect of these unmodelled deformations on the accuracy of the model.

- The kinetostatic model could be extended to include the out-of-plane flexure hinge compliances, such as $\Delta\alpha_x/M_x$, $\Delta\alpha_y/M_y$ and $\Delta z/F_z$; therefore it could be also applied to spatial compliant mechanisms.

- The kinetostatic model could be extended to include the piezo-actuator stiffness in order to predict the kinetostatic of the whole compliant micro-motion system.

- A 3-D FEA model of the micro-motion stages could be generated using other FEA software which could provide sufficient number of nodes to accurately model the stiffnesses and deformations of the structures. The measurement errors presented in Section 7.4.1.1.1 can be investigated using the 3-D FEA model. The results of the 2-D FEA compliant stage model are suggested to be compared to the results of the 3-D model in order to investigate the accuracy of the 2-D FEA model.

- The experimental setup of measuring the compliances ($\mathbf{C_{o,F_o}}$ and $\mathbf{C_{o,F_{in}}}$) of the 3-RRR micro-motion stage can be improved by using force/torque transducers to measure the applied forces/moments. Out-of-plane deformations should be measured using a few extra sensors in order to quantify the measurement errors and to calculate the "actual" in-plane deformations caused by the applied in-plane forces/moments.